Università degli Studi di Padova

Dipartimento di Ingegneria Industriale DII

Corso di Laurea Magistrale in Ingegneria Aerospaziale

Mechanical Design of a Floating Pneumatic Module for Zero-gravity Motion Simulation

Relatore:

Prof. Francesco Branz

Laureando:

Simone Galleani

2004163

Anno Accademico 2022/2023

Abstract

Close Proximity Operations (CPOs) are critical maneuvers between two on-orbit spacecrafts which demand an accurate control in a micro-gravity environment, hence they must be reproduced and simulated with a systematic approach. Consequently, by creating specific facilities and spacecraft simulators, laboratory tests are a crucial aspect to validate the performances of space systems for CPOs.

This thesis presents the development, measurements and testing for mass-inertia properties evaluation of a floating pneumatic module, whose dimensions are representative of a 12U CubeSat system. The vehicle has been designed to perform planar low friction motion over a levelled table for docking experiments.

The thesis focuses on the mechanical design of the module, which has revolved around two main requirements: (1) the possibility to accommodate a docking system for complete modularity and adaptability to different devices (e.g.: docking port); (2) the control of the position of the center of mass of the system to ensure uniform floating and pure rotations with an actuated pneumatic system.

The first half illustrates a detailed overview of the assigned requirements and complete design of the module, from the early stages of development to the final one. The second half presents the several measurements and tests which have been performed to estimate the mass-inertia properties of the vehicle. The main goal has been to improve the estimation provided by the CAD model of the fully assembled system through the realization of dedicated setups to find and control the position of the center of mass and through the execution of simple rotational motions to calculate the inertia around the main axis.

Sommario

Le Close Proximity Operations (CPOs) sono manovre critiche tra due veicoli spaziali in orbita che richiedono un accurato controllo in un ambiente di micro-gravità, pertanto devono essere riprodotte e simulate con un approccio sistematico. Di conseguenza, con la realizzazione di attrezzature specifiche e simulatori di satelliti, i tests in laboratorio sono un aspetto cruciale per validare le prestazioni di sistemi spaziali dedicati alle CPOs.

Questi tesi presenta lo sviluppo, le misurazioni sperimentali e i tests per la stima della proprietà di massa e inerzia di un modulo pneumatico flottante, le cui dimensioni sono rappresentative di un sistema CubeSat a 12U. Il veicolo è stato realizzato per eseguire un moto planare a basso attrito su una superficie livellata al fine di simulare esperimenti di docking.

La tesi si concentra sul design meccanico del modulo, il quale si è basato su due requisiti principali: (1) la possibilità di accomodare un sistema di docking per garantire una completa modularità e adattabilità a diversi dispositivi (e.g.: docking port); (2) il controllo della posizione del centro di massa del sistema per garantire un flottaggio uniforme e rotazioni pure con un sistema pneumatico controllato.

La prima parte illustra una descrizione dettagliata dei requisiti assegnati e del design completo del modulo, dalle prime fasi di sviluppo a quella finale. La seconda parte presenta le numerose misurazioni sperimentali e tests che sono stati svolti per stimare le proprietà di massa e inerzia del veicolo. L'obiettivo principale è stato migliorare la stima fornita dal modello CAD del sistema totalmente assemblato attraverso la realizzazione di setups dedicati all'individuazione e il controllo della posizione del centro di massa e attraverso l'esecuzione di semplici moti rotazionali per calcolare l'inerzia attorno all'asse principale.

Contents

List of Figures

Chapter 1

Introduction

1.1 Spacecraft simulators for close proximity operations

A Close Proximity Operation (CPO) of on-orbit spacecraft (spacecraft orbiting around a celestial body) can be defined as a sequence of maneuvers of one spacecraft (chaser) in a relative orbit with respect to another spacecraft (target) [1]. On-orbit objects are in a free fall state due to the gravitational pull, hence they move in micro-gravity conditions. Therefore, CPOs (e.g.: berthing, rendezvous, capturing, on-orbit servicing and docking) are characterized by complex relative motions which require a systematic evaluation of the kinematics, forces and torques arising from the interaction between the chaser and the target.

The validation of the performances of CPOs enabling technologies is achieved by the realization of spacecraft simulators and facilities which reproduce the kinematics and/or the dynamics of the on-orbit relative motions in a laboratory environment. When reproducing micro-gravity conditions, spacecraft simulators can be divided into (1) kynematic and (2) dynamic simulators [1]:

1. Kynematic simulators perform translational or rotational motions with actuators that are not adopted by actual space systems (e.g.: electrical motors); therefore, they only simulate the kinematics of a CPO, because the generated forces and torques are not representative of the on-orbit motion;

2. Dynamic simulators generate forces and torques with actuators implemented on actual space systems (e.g.: reaction wheels, thrusters) and adopt several suspension methods to simulate the micro-gravity conditions, so that the dynamics of CPOs are reproduced.

1

Kynematic simulators include robotic manipulators, which can perform motions ranging from 1 Degree of Freedom (DoF) to 6 DoF. Among the suspension methods, dynamic simulators, for instance, involve the use of neutral buoyancy water tanks or planar air-bearings, the latter being the focus of this thesis and the following sections.

More complete, but, at the same time, more complex microgravity simulation methods include suborbital micro-gravity systems [1], such as drop towers and parabolic flights, which reproduce the full 6 DoF on-orbit motion, along with the dynamics, but have the great limitation of a reduced simulation time.

1.2   Planar air-bearings and thesis overview

Among the many micro-gravity simulation methods, an easily achievable and accessible solution for a laboratory environment is the use of planar Air-Bearings (ABs), which are mounted on tested devices to allow their floating [2] through the creation of a thin film ($5-15\,\mu$m, depending on input pressure and supported weight) of a pressurized gas, tipically compressed air or CO_2, between an internal porous structure and a smooth surface, such as an epoxy floor, a granite monolith or a glass plate over an optical bench [1]. Figure 1.1 shows a schematic view of a planar AB.
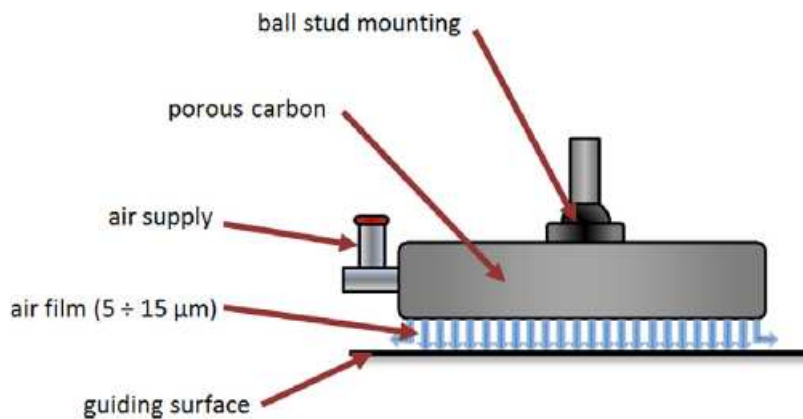
Figure 1.1: Schematic view of a planar air-bearing, reprinted from [2].

Furthermore, several actuators, such as thrusters and/or reaction wheels, are usually mounted on the floating devices to generate parallel forces and perpendicular torques with respect to the smooth flat surface. Consequently, a planar 3-DoF motion (2 translations and 1 rotation) can be achieved in a quasi frictionless condition (friction coefficient of approximately 10^{-5} [3]). Although a reduced

number of DoF is obtained compared to the 6 DoF of an on-orbit motion and to other spacecraft simulation methods, planar ABs are mostly used as suspension supports for dedicated vehicles (dynamic simulators) to reproduce CPOs and, specifically, docking maneuvers experiments [2].

This thesis presents the mechanical design, development and testing of a floating pneumatic module which has been designed to perform 3-DoF low friction planar motion with three ABs over a glass plane mounted on an optical bench (which will be referred to as levelled table). The module is a dynamic spaceraft simulator with a mass of approximately $12\,\text{kg}$ and a volume of $330 \times 224 \times 224\,\text{mm}^3$, so that it represents the dimensions of a 12U CubeSat. With a dedicated compressed air propulsion system, the main goal of the vehicle is to simulate docking maneuvers starting from a $500\,\text{mm}$ distance. The system has been realized to accommodate different docking systems (e.g.: docking port) and can operate either as a chaser, active mode, or a target, passive mode. Figure 1.2 illustrates the fully assembled module on the levelled table.
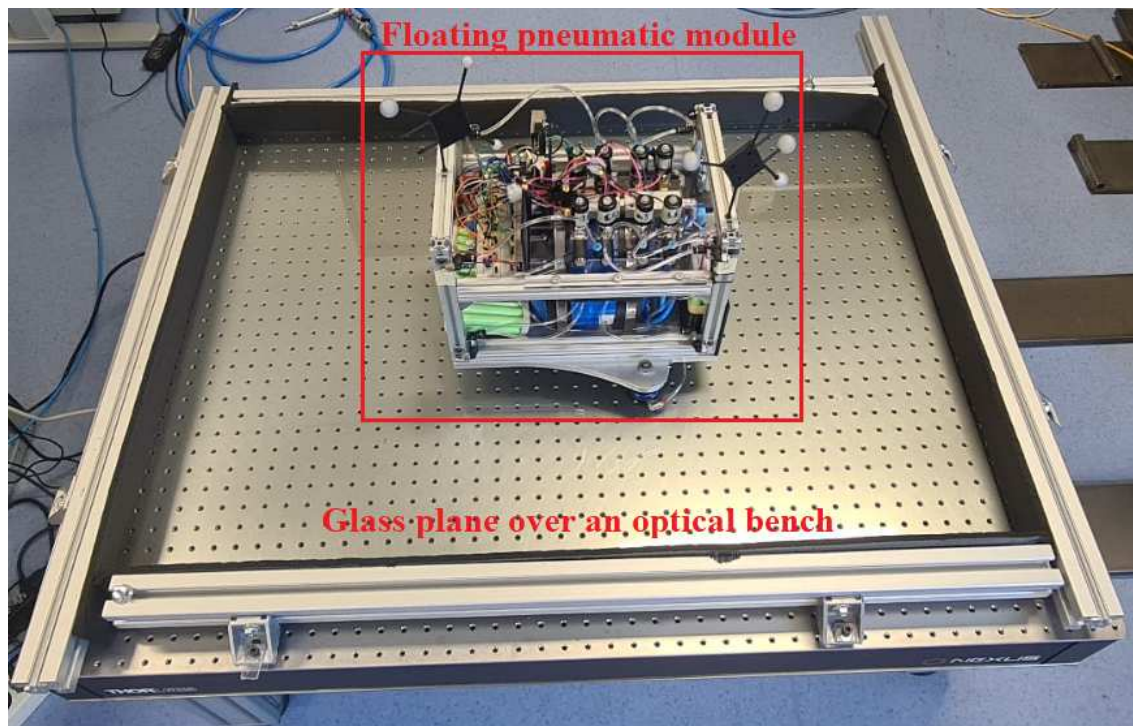
Figure 1.2: Fully assembled module on the levelled table.

Chapter 2

Mechanical design requirements and early stages of development

The mechanical design has revolved around the positioning and sizing of components, such as structural, pneumatic and electrical ones, so that they would fit inside the total volume of the module. Since the pneumatic system has been the most critical part of the module in terms of occupied space and mass, the pneumatic and mechanical designs have been developed together right from the start.

Firstly, this Chapter describes the requirements of the mechanical design (Section 2.1). Secondly, due to the pneumatic system being the most crucial part of the module in terms of occupied space, Section 2.2 presents the major requirements and project specifications of the pneumatic design which have influenced the mechanical one. Lastly, Section 2.3 illustrates an overview of the early stages of development which have led to the final design of Ch. 3.

2.1 Requirements of the mechanical design

The mechanical design has followed six requirements:

1. The module has a total volume of $330 \times 224 \times 224 \, \text{mm}^3$ and the total mass is approximately $12 \, \text{kg}$, thus the mass-inertia properties resemble a 12U CubeSat;

2. The module accommodates a docking system for complete modularity and adaptability to different devices (e.g.: docking port) with a dedicated volume of $100 \times 224 \times 224 \, \text{mm}^3$ (30.3% of the total volume) in the front part;

therefore, the major pneumatic and electrical components are mounted in the back $230 \times 224 \times 224\,\text{mm}^3$ (69.7% of the total volume) part (Figure 2.1a), when possible and with the exception of the ABs, which are mounted outside of the total volume to ensure a better floating;

3. The main frame of the structure is composed by $20 \times 20\,\text{mm}$ aluminum strut profiles made by Bosch Rexroth to provide a versatile mounting for components and payloads with M4 T-nuts and bolts (Figure 2.1b);
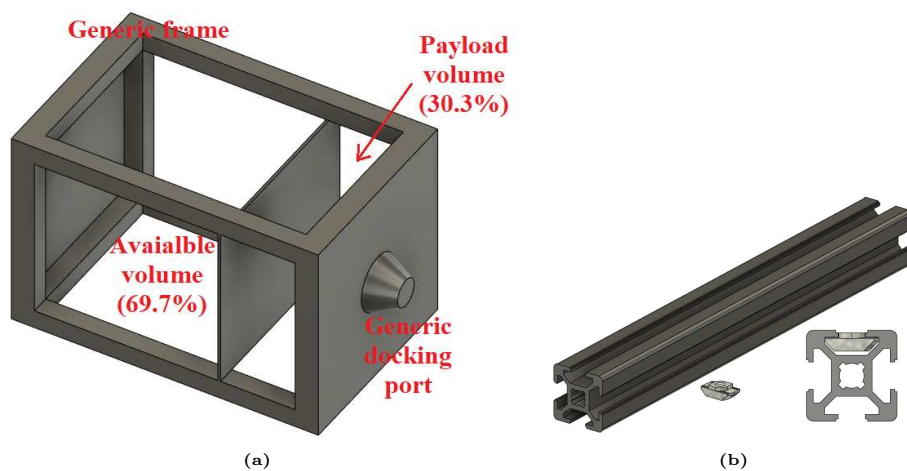
Figure 2.1: (a) Schematic view of the $230 \times 224 \times 224\,\text{mm}^3$ available volume and the $100 \times 224 \times 224\,\text{mm}^3$ payload volume and (b) CAD model of a generic $20 \times 20\,\text{mm}$ strut profile and a M4 T-nut.

4. The module floats with three ABs, so that they automatically form a three-point stance to support the vehicle on one plane [2] (smaller or greater numbers of ABs would require a precise levelling to avoid the deflection of a misaligned AB which would result in a disturbative force or torque on the system);

5. The three ABs are positioned in an equilateral triangular configuration and the Center of Mass (CoM) of the module is controlled to be coincident (within an error of 1 mm) with the centroid of the ABs to guarantee uniform floating of the vehicle;

6. The propulsion system allows a 3-DoF planar motion by activating eight thrusters in a rectangular configuration (two thrusters per corner of the rectangle in a 90 deg relative configuration); therefore, the centroid of the thrusters is coincident with the CoM of the system to allow pure rotational

motions; Figure 2.2 shows a schematic view of the 3 DOF motion which is achieved by aligning the thrusters centroid with the CoM.
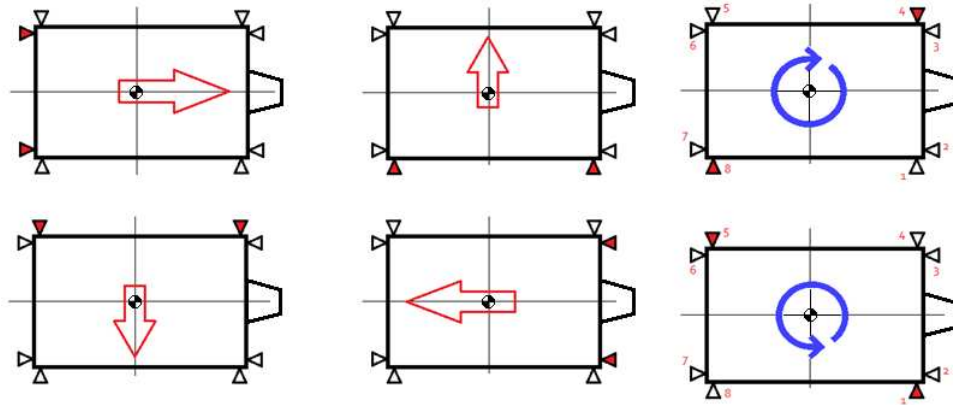
Figure 2.2: Schematic view of the achieavable 3 DoF planar motion.

The three alignments of requirements #5 and #6 have represented the main goal of the mechanical design: ideally, these three points need to be geometrically coincident during all experiments. While the position of the centroids of the ABs and the thrusters have been simply defined by the geometrical design of the corresponding supports and mountings, the control of the CoM location has proven to be more critical. The solution has been found in the design of fixed and movable steel masses to be placed along the main structure of the module and the realization of a dedicated setup to measure and control the position of the CoM (see Chs. 3 and 4 for details).

Additionally, the three alignments have been achieved only on the $330 \times 224\,\mathrm{mm}^2$ plane of translational movement, because their coordinate along the main rotational axis is irrelevant to ensure a planar 3-DoF motion.

2.2 Main requirements and project specifications of the pneumatic design

The pneumatic design and its major requirements and project specifications have greatly influenced the mechanical design. The pneumatic system has been realized by following four main requirements from the start:

1. The pneumatic circuit is supplied with compressed filtered air and recharged by an external air compressor at 10 bar;

2. The eight thrusters are activated by eight solenoid 24 V Electro-Valves (EVs);

3. The three ABs ensure a total floating time of 3 min with an increased mass of 24 kg;

4. The propulsion system ensures a linear acceleration of $50 \, \mathrm{mm \, s^{-2}}$ with an increased mass of 24 kg.

Additionally, all the CAD models and early designs, as well as the final design of Ch. 3, consider a 9th EV to act as a remotely controllable valve for the ABs. The fully assembled module (Figure 1.2) has substituted this additional EV with a manual valve to simplify the execution of all tests.

Requirements #1, #3 and #4 have led to a first estimation of the total volume of air at 10 bar to be stored inside a tank. By considering three flat-round 40 mm ABs (total ideal load of approximately 60 kg at around 4 bar to have a considerable margin over the 24 kg) and two nozzles with a throat diameter of 1 mm for each thruster (sixteen total nozzles) to improve the produced force and reduce the working pressure to approximately 3.9 bar, the total required air volume has been calculated to be 1.27 L* with a residual tank pressure of 4.4 bar after depletion (0.5 bar margin over the working pressure).

The most critical pneumatic components in terms of dimensions and mass for the mechanical design have been:

- The tank at a storage pressure of 10 bar;

- The nine EVs;

- The pressure regulator to control the ABs and EVs at the same input pressure.

Since compressed air at 10 bar requires a considerable volume for storage, defining a tank or multiple tanks has been necessary to develop the early designs. Several configurations have been considered to understand the percentage of the available $230 \times 224 \times 224 \, \mathrm{mm^3}$ volume to be dedicated to stored air. A solution to improve the occupied space and store greater volumes could have involved the use of multiple tanks. Figure 2.3 shows a configuration of 4 tanks of approximately 1 L each (total volume of 4 L).

---

*All volumes related to air and tanks storage are expressed in liters for a better understanding of the occupied space
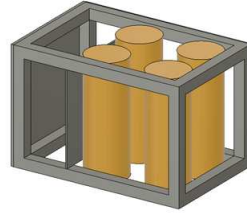
Figure 2.3: Configuration of 4 1 L tanks.

Figure 2.4 shows a second configuration of 10 smaller tanks, 2 with approximately 0.5 L and 8 with approximately 0.3 L (total volume of 3.4 L).
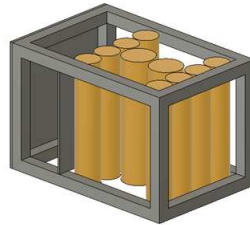
Figure 2.4: Configuration of 10 tanks, 2 0.5 L tanks and 8 0.3 L tanks

Even though greater volumes could have been stored, multiple tanks would have considerably complicated the mechanical design by introducing much more pneumatic connections, tubing and supports. Therefore, a configuration of a single tank has been chosen to be definitive for the module.

All early designs have considered a 3 L $160 \times \phi 160 \, \text{mm}^2$ tank (model 3L-A made by *Jian Yue*). Even though its stored volume of 3 L is considerably greater than the estimated required one of 1.27 L, the goal of the early designs has been to understand the impact of bigger components on the available space. Figure 2.5 shows the 3 L tank and corresponding CAD model.
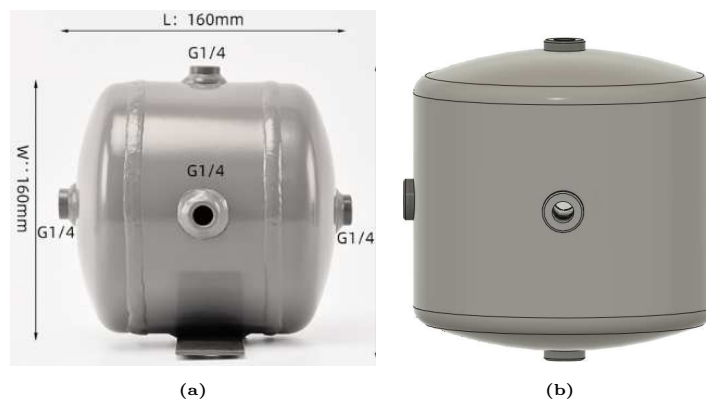
Figure 2.5: (a) 3 L $160 \times \phi 160 \, \text{mm}$ tank, model 3L-A made by *Jian Yue*, and (b) corresponding CAD model.

For the same reason, the early designs have included the EV shown in Figure 2.6 (model VZWD-L-M22C-M-G18-10-V-1P4-50 made by *Festo*), which differ from the actual EVs of the final design and the assembled module (see Ch. 3) in terms of greater mass ($300\,\mathrm{g}$) and dimensions ($52 \times 32 \times 30\,\mathrm{mm}^3$).

(a)   (b)
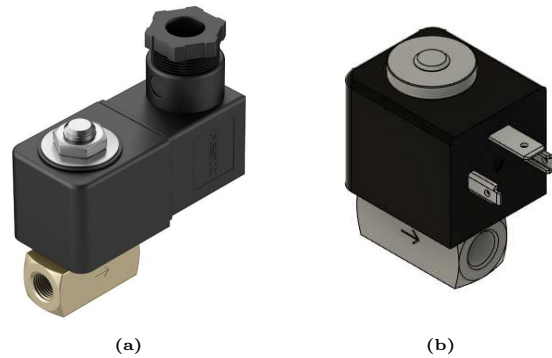
Figure 2.6: (a) Electro-valve of the early designs, model VZWD-L-M22C-M-G18-10-V-1P4-50 made by *Festo*, and (b) corresponding CAD model.

Finally, Figure 2.7 illustrates the CAD model of the $40 \times 40 \times 74\,\mathrm{mm}^3$ pressure regulator (model T020-MINI made by *AIGNEP*, pressure regulation ranges from $0\,\mathrm{bar}$ to $8\,\mathrm{bar}$ with integrated manometer, total mass of $192\,\mathrm{g}$) and corresponding mounting staff which have been chosen for the early and the final designs.
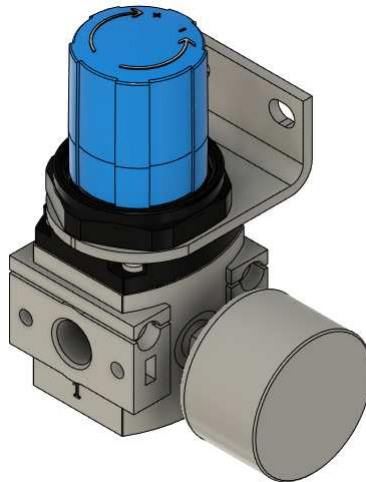
Figure 2.7: CAD model of the pressure regulator, model T020-MINI made by *AIGNEP*, integrated manometer and mounting staff

2.3   Early designs of the module

This section presents the early designs of the module which led to the final design of Ch. 3.

Firstly, there have been 2 possible configurations for the single 3 L tank: a vertical configuration (Figure 2.8a) and a horizontal configuration (Figure 2.8b).
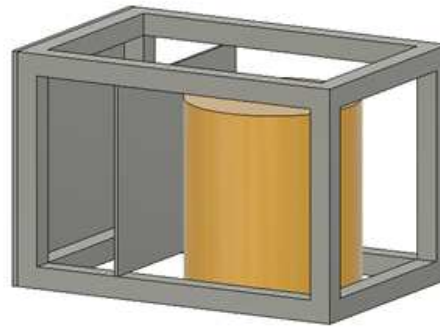
(a)
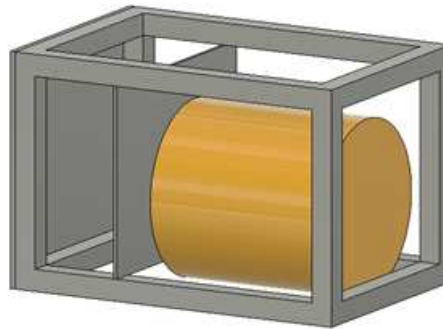
(b)

Figure 2.8: (a) Vertical and (b) horizontal configuration of the 3 L tank.

On one hand, the vertical configuration allows to shift the CoM of the tank towards the center of the module, but makes the corresponding mountings and supports more complicated. On the other, the horizontal configuration simpflies the possibility to directly anchor the tank to the main structure, but shifts its CoM towards the back part of the module. The initial designs have considered the vertical configuration.

The early designs have included the following necessary electrical components:

- Two Raspberry Pi 3 electronic boards, one to control the activation of the EVs and the other dedicated to a generic payload;

- One or two 24 V batteries (depending on the available space and the best case scenario being two batteries to ensure longer functioning times of the module to perform multiple or repetitive tests) to power the EVs and the Raspberries.

The initial idea has been to create (1) a main structural frame at the edges of a $325 \times 214 \times 214\,\text{mm}^3$ parallelepiped with (2) 5 polycarbonate walls (1 top wall, 2 side walls, 1 back wall and 1 bottom wall) with a thickness of 5 mm to support the tank, the EVs, the nozzles, the batteries and the Raspberries. Figure 2.9 shows the first iteration of this solution.
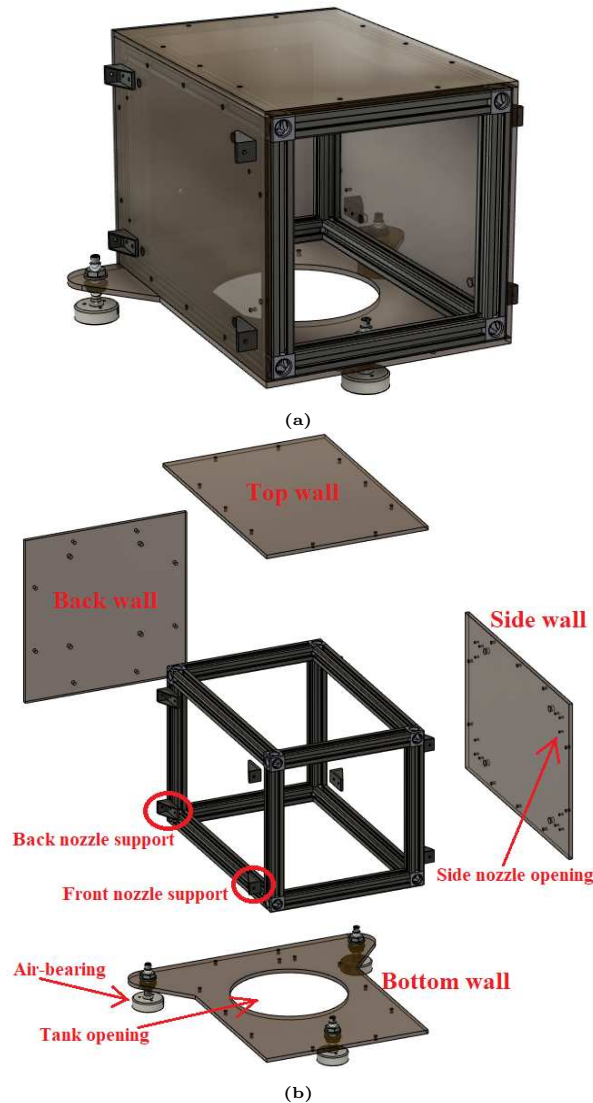
Figure 2.9: (a) CAD model of the initial solution and (b) exploded view.

This configuration has been developed with the goal of gaining an easy access to the main components by mounting them on the completely removable polycarbonate walls, so that maintenance procedures could have been performed at any time. The configuration has also included a $\phi 150\,\text{mm}$ opening on the bottom wall (Figure 2.9b) to use a part of the space between the levelled table and the module for the tank base to grant more room in the top part of the system. The

configuration of Figure 2.9 has led to two main preliminary designs. The first one is shown in Figure 2.10.

(a)

(b)
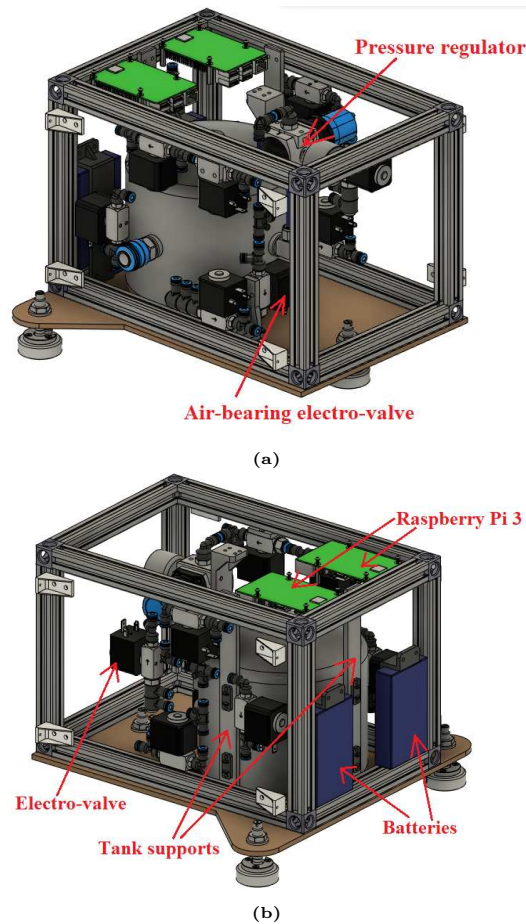
Figure 2.10: First preliminary design of the module: (a) View 1, (b) View 2.

This first preliminary design has been characterized by:

- The eight nozzle EVs to be mounted on the side polycarbonate walls with the corresponding pneumatic fittings;

- The ABs EV to be mounted on the bottom polycarbonate wall in the front part of the module;

- The 3 L tank in a vertical configuration with the corresponding support plates to allow the positioning of two belts for fixing;

- The pressure regulator to be mounted on the top polycarbonate wall;

- The two Raspberries electronic boards to be mounted on the top polycarbonate wall;

- The two 24 V batteries to be mounted on the back polycarbonate wall.

Figure 2.11 shows the second preliminary design.

(a)

(b)
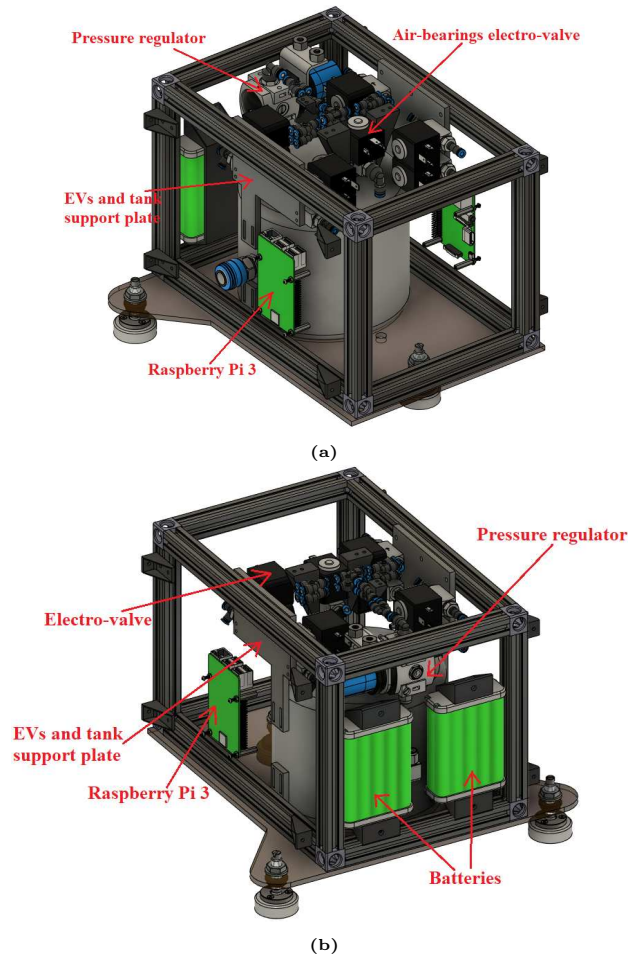
Figure 2.11: Second preliminary design of the module: (a) View 1, (b) View 2.

This second preliminary design has been characterized by:

- Four aluminum plates to be fixed on the main structural frame and to provide mounting of the eight nozzle EVs and the 3 L (vertical configuration) with two belts; Figure 2.12 presents a detail of the plates;

- The ABs EV to be mounted on the top polycarbonate wall in the front part of the module

- The pressure regulator and most of the pneumatic fittings to be mounted on the top polycarbonate wall;

- The two Raspberries electronic boards to be mounted on the side polycarbonate walls;
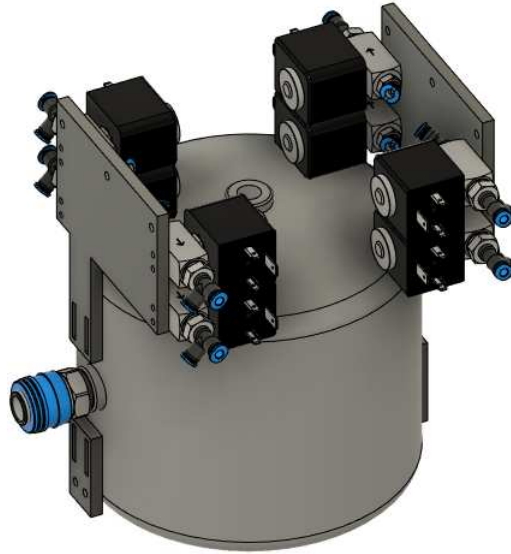
Figure 2.12: Detail of the four aluminum plates for the nozzle EVs and tank.

- The two 24 V batteries to be mounted on the back polycarbonate wall.

With these two preliminary designs, the following problems have arisen:

- An excessive amount of additional tubing and wiring (which are not shown in the CAD models) would have been required to remove the polycarbonate walls with the mounted major components;

- The tank supports for the vertical configuration have occupied additional space around the 3 L tank;

- The pressure regulator could not be easily accessed to regulate the ABs and EVs input pressure without removing the top wall;

- A single battery could not be removed without also removing the other one and the entire back polycarbonate wall;

- The centroids of the ABs and the nozzles are not coincident; Figure 2.13 shows this misalignment, with C_{AB} the ABs centroid, C_N the nozzles centroid and GC the Geometrical Center of the $330 \times 224 \times 224$ mm volume;

- The nozzles supports and openings have not taken into account the actual shape of the nozzles, because they were not yet chosen at the time.

Despite these issues, the preliminary designs have been useful to understand the impact of the major pneumatic and electrical components on the available

space of the module. However, they have also proven that the tank in a vertical configuration and the polycarbonate external walls as critical supports of the structure have led to overcomplicated designs.

Therefore, a new solution has been found with the two following characteristics:

1. The mounting of the tank in a horinzotal configuration;

2. The development of the vehicle to be fully functioning without the top, back and side polycarbonate walls of Figure 2.9b.

This solution has ultimately led to the final design and assembly of the module, which are discussed in Ch. 3.
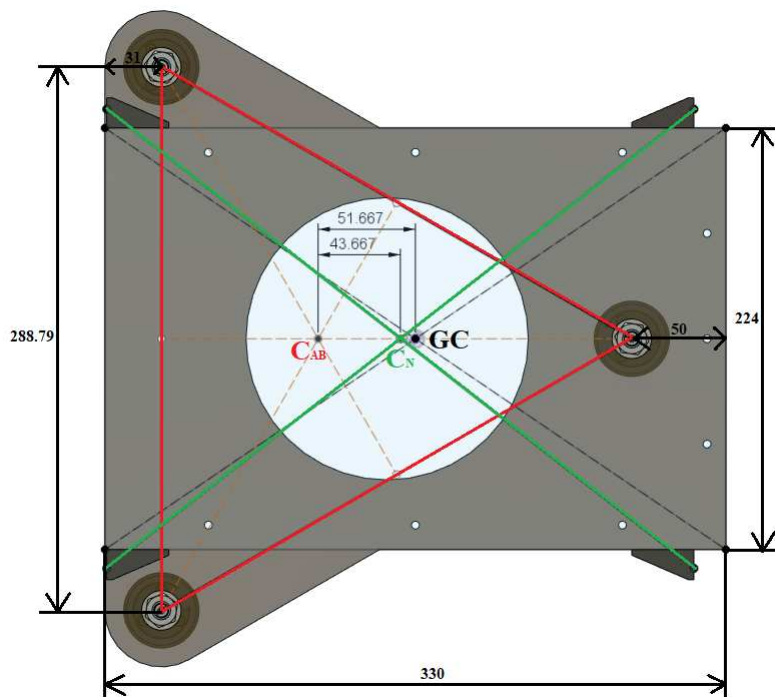
Figure 2.13: Misalignment of the ABs and nozzles centroids (quotes in mm).

Chapter 3

Final design and assembly of the floating pneumatic module

This chapter presents a detailed overview of the final design of the floating pneumatic module. The final design has been developed to solve all the major problems of the early designs of Section 2.3 and has the following characteristics:

- The top, side and back polycarbonate walls of Figure 2.9 (Ch. 2) have been redesigned with a 3 mm thickness without supporting any internal component; therefore:

    - Maintenance procedures can be easily performed by removing them;

    - The module fully functions without them;

- The bottom wall of Figure 2.9 (Ch. 2) has been redesigned to a 10 mm thick aluminum wall to:

    - Represent the main part of the main structural frame to sustain the weight of the system;

    - Position the tank in a horizontal configuration to simplify its mounting and supports;

    - Position the ABs to align their centroid with that of the nozzles;

- The structural frame of aluminum profiles has been redesigned to allow the mounting of an internal polycarbonate wall (referred to as mid wall) on top of the tank with the goal of supporting the nine EVs, the two Raspberry Pi 3 electronic boards, the pressure regulator and the corresponding necessary pneumatic connections.

Due to market availability, a $2.5\,\text{L}$ $159 \times \phi160\,\text{mm}^2$ tank (model S2.5N made by *PANAR*) has been chosen as a definitive component for the final design. Its dimensions are equivalent to the $3\,\text{L}$ $160 \times \phi160\,\text{mm}^2$ tank of the early designs (see Figure 2.5, Ch. 2) and its stored volume is still greater than the estimated required one of $1.27\,\text{L}$. Moreover, the tank has a mass of $1.472\,\text{kg}$. Figure 3.1 shows the CAD model of the definitive $2.5\,\text{L}$ tank.

Figure 3.1: CAD model of the definitive $2.5\,\text{L}$ tank, model S2.5N made by *PANAR*.

The final design has also included a set of fixed and movable steel masses which have been specifically designed to control the position of the CoM of the system around the centroid of the ABs (see Section 3.5).

Figure 3.2 shows the CAD model of the definitive design and the fully assembled vehicle. Figure 3.2a also illustrates the main reference frame at the GC of the module used to refer the position of several components and the CoM of the system.

(a)

(b)
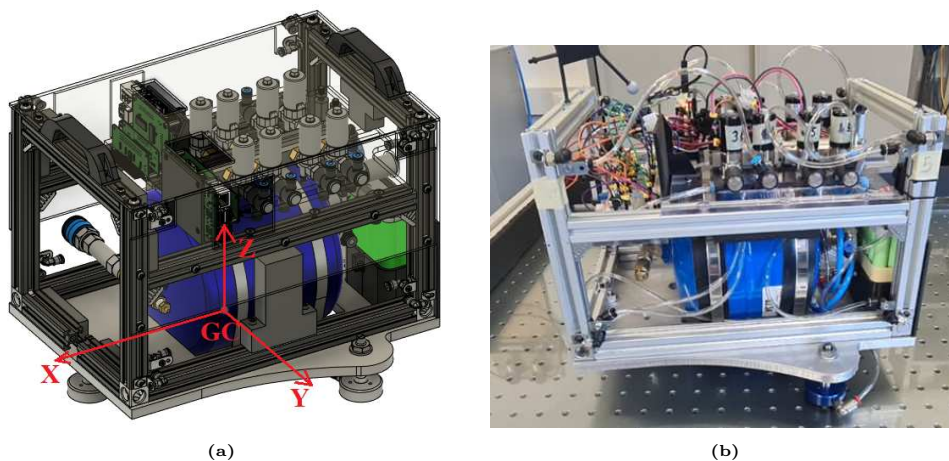
Figure 3.2: (a) CAD model of the vehicle and (b) assembled module (no external polycarbonate walls).

3.1   Main structural frame and mounting of ABs, nozzles and tank

The main structural frame is composed by:

1. The 10 mm thick aluminum bottom wall;

2. The structural frame of aluminum strut profiles;

Their design has been developed to satisfy the following 3 requirements:

1. Allow mounting of an internal polycarbonate wall (mid wall) to support the nine EVs, the two Raspberry Pi 3 electronic boards and the pressure regulator;

2. Align the ABs and nozzles centroids;

3. Position the tank in a horizontal configuration.

For requirement #1, the structural frame of aluminum strut profiles has been modified from the early designs by lowering the position of the two top horizontal profiles to act as a support for the mid wall. Additionally, the occupied volume has been increased from $325 \times 214 \times 214 \,\mathrm{mm}^3$ (early designs) to $327 \times 218 \times 211 \,\mathrm{mm}^3$ to account for the reduced 3 mm thickness (from 5 mm of the early designs) of the side, top and back polycarbonate walls and the increased 10 mm thickness of the bottom wall (the total volume of the module is $330 \times 224 \times 224 \,\mathrm{mm}^3$).*
Figure 3.3 shows a comparison between the structural frame of the early designs and the new one which has led to the definitive design.

---

*These volumes and all volumes in the following pages are always written as *Dimension along X × Dimension along Y × Dimension along Z*, where the X, Y and Z axes are the ones shown in Figure 3.2a.
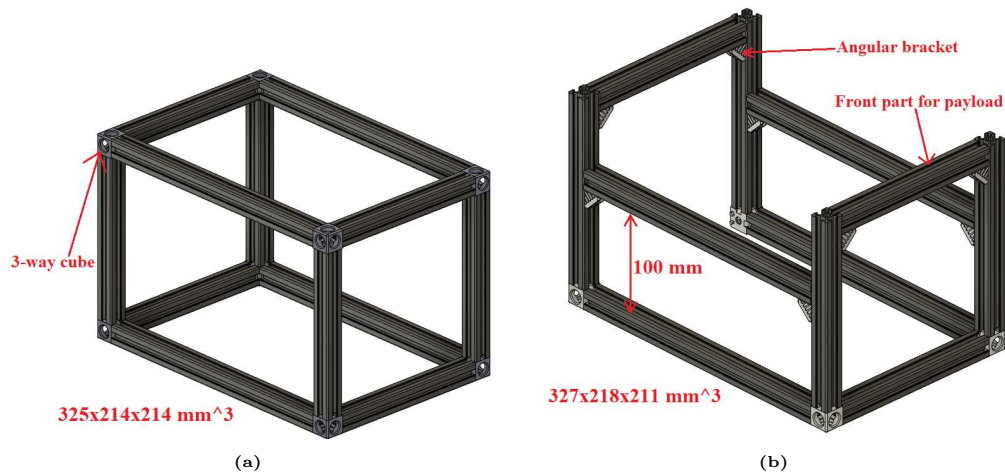
Figure 3.3: (a) Structural frame of the early designs and (b) new structural frame.

The two horizontal lowered profiles have been positioned at a 100 mm distance from the bottom profiles to ensure no conflict between the tank and the mid wall. Furthermore, the bottom strut profile in the back has been removed to grant more space behind the tank and the four 3-way cubic connectors on the top part have been substituted with 4 angular brackets to grant more space for the top nozzles.

For requirement #2, the 3D printer nozzles shown in Figure 3.4a have been initially considered. Specifically, these common 3D printers nozzles with a $\phi 1$ mm throat diameter and a M6 thread have been combined with a 10 mm M6 spacer, 3D printed supports and a proper pneumatic fitting (see Figure 3.4b) to be mounted on the strut profiles.
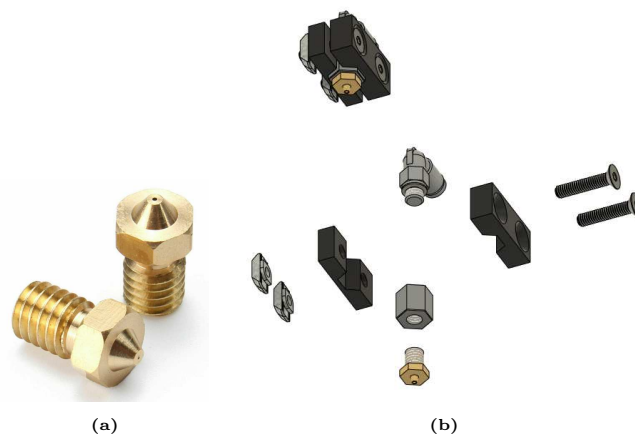
Figure 3.4: (a) $\phi 1$ mm nozzle and (b) CAD model of a nozzle assembly with exploded view.

To satisfy requirement #2, two solutions have been explored:

1. Design the bottom 10 mm thick aluminum wall to keep the ABs centroid at

a distance of approximately 52 mm from the GC (equivalent to Figure 2.13, Chapter 2) and add two vertical strut profiles to the structural aluminum frame of Figure 3.3b to support the front nozzles;

2. Design the bottom 10 mm thick aluminum wall to align the ABs centroid with the GC and mount the 16 nozzles at the 4 corners of the structural frame.

Solution #1 is presented in Figure 3.5. By adding two vertical strut profiles with a 100 mm length, all 16 nozzles have been mounted around the tank sides and below the position of the mid wall. While preventing a conflict between the front AB support and the front strut profile, this cramped configuration would have led to excessively tight curvatures for the tubing going from the EVs to the nozzles and taken away additional space for the components behind the tank.
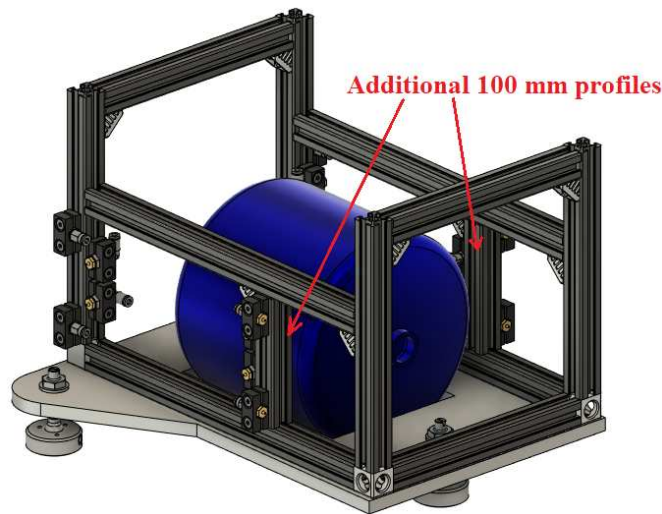
Figure 3.5: Solution #1 for the alignment of the ABs and nozzles centroids.

Solution #2 is presented in Figure 3.6 and has proven to be more practical and achieavable. The front AB has been positioned to have its $\phi40$ mm circumference tangential to the border of the $330 \times 224 \times 224$ mm^3 volume and, therefore, the front strut profile has been splitted into two smaller ones with a 77 mm length, which have been kept to allow a proper mounting for a generic payload, despite not providing any structural stiffness.
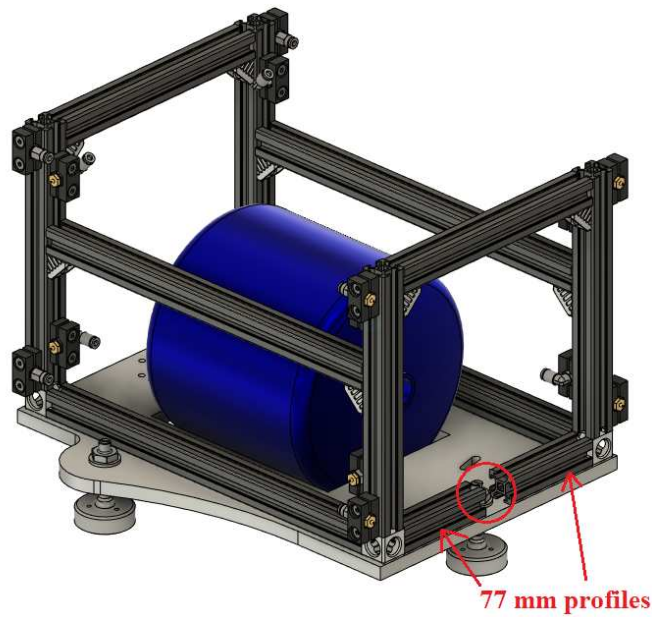
Figure 3.6: Solution #2 for the alignment of the ABs and nozzles centroids.

Figure 3.7 shows a schematic view of the obtained alignment.
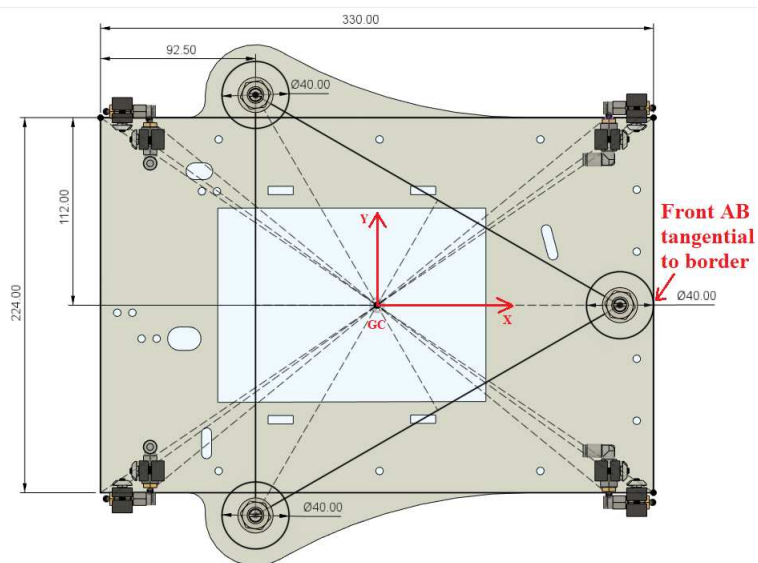
Figure 3.7: Schematic view of the obtained alignment.

The finalized bottom wall has an overall mass of 1.693 kg.

Figure 3.8 illustrates a detail of an AB and its ball mounting screw ($M10 \times 0.75 \times 54$ mm) on the bottom wall. The ABs are not actually fixed on the module, the vehicle is laid on the ABs over the levelled table instead.
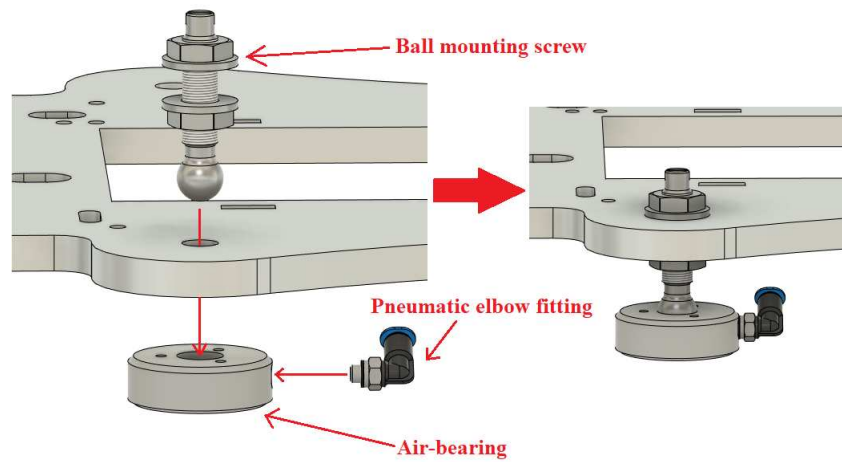
Figure 3.8: Air-bearing and ball mounting screw on the bottom wall.

While offering a simple design which has led to the configuration of Figure 3.4, the 3D printer nozzles are not meant to operate with compressed air (they create 3D printed layers made by termoplastic materials). Consequently, they would have required an additional sequence of tests to validate their performances and safety when generating a thrust at a given input pressure. To simplify the pneumatic system, the final design has included 16 elbow pneumatic fittings ($\phi 4\,\text{mm}$ tubing and M3 thread) with a throat diameter of $\phi 1.3\,\text{mm}$ to act as nozzles and corresponding steel supports to be mounted on the strut profiles in a configuration equivalent to Figure 3.6.

Figure 3.9 presents the new nozzles and supports, the three separate configurations used to align their centroids with the GC of the system and their overall positioning on the structure. By mounting the nozzles with a single nut on the supports, it has been possibile to easily rotate their configurations to adapt them to the tubing.

(a)

(b)

(c)
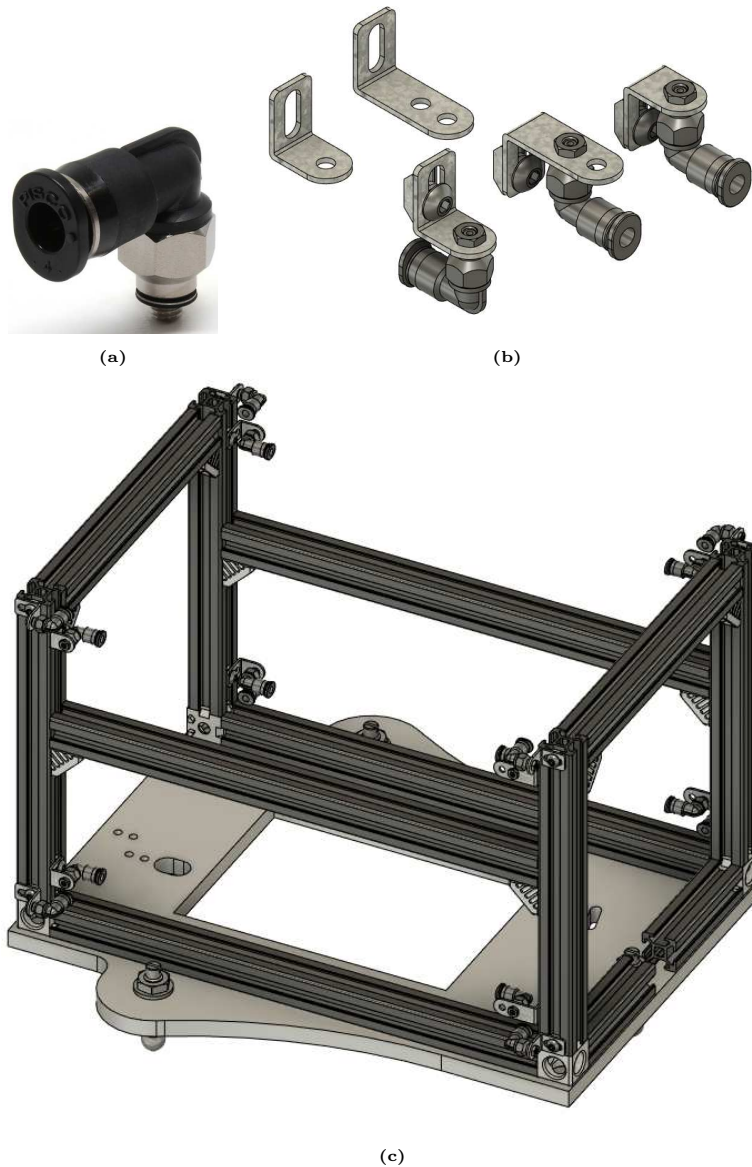
Figure 3.9: (a) $\phi 1.3\,\mathrm{mm}$ nozzle, (b) CAD model of the nozzle assemblies with a detail on the steel supports and (c) mounting on the structure.

The increased $\phi 1.3\,\mathrm{mm}$ throat diameter with an equivalent $3.9\,\mathrm{bar}$ input pressure has led to a new estimation of the required air volume of $1.51\,\mathrm{L}$ ($3\,\mathrm{min}$ of total floating time and linear acceleration of $50\,\mathrm{mm\,s^{-2}}$ with an increased mass of $24\,\mathrm{kg}$). While being slighlty greater than the evaluated one with the previous nozzles, the new required volume is still lower than the total $2.5\,\mathrm{L}$ stored volume of the tank.

Lastly, to satisfy requirement #3 of positioning the tank in a horizontal configuration, a rectangular $160 \times 115.5\,\mathrm{mm^2}$ opening and 4 smaller ones ($15 \times 5\,\mathrm{mm^2}$) have been created on the bottom wall to mount the tank with 2 flexible aluminum

belts with a circumference adjustable from $\phi150\,\mathrm{mm}$ to $\phi180\,\mathrm{mm}$. The bigger hole has also been realized at a $100\,\mathrm{mm}$ distance from the front edge of the bottom wall to free up as much space as possibile in the back part, while still placing the tank inside the avaialable $230 \times 224 \times 224\,\mathrm{mm^3}$ volume.

Figure 3.10 illustrates the aluminum belts, the rectangular openings on the bottom wall, the CAD model and assembly of the mounted tank. In Figures 3.10c and 3.10d, the $2.5\,\mathrm{L}$ tank is shown together with the necessary pneumatic components, which include a quick release coupling for fast refilling, a safety release valve to set the maximum internal pressure at $10\,\mathrm{bar}$ and a manual valve for fast emptying.

(a)

(b)

(c)

(d)
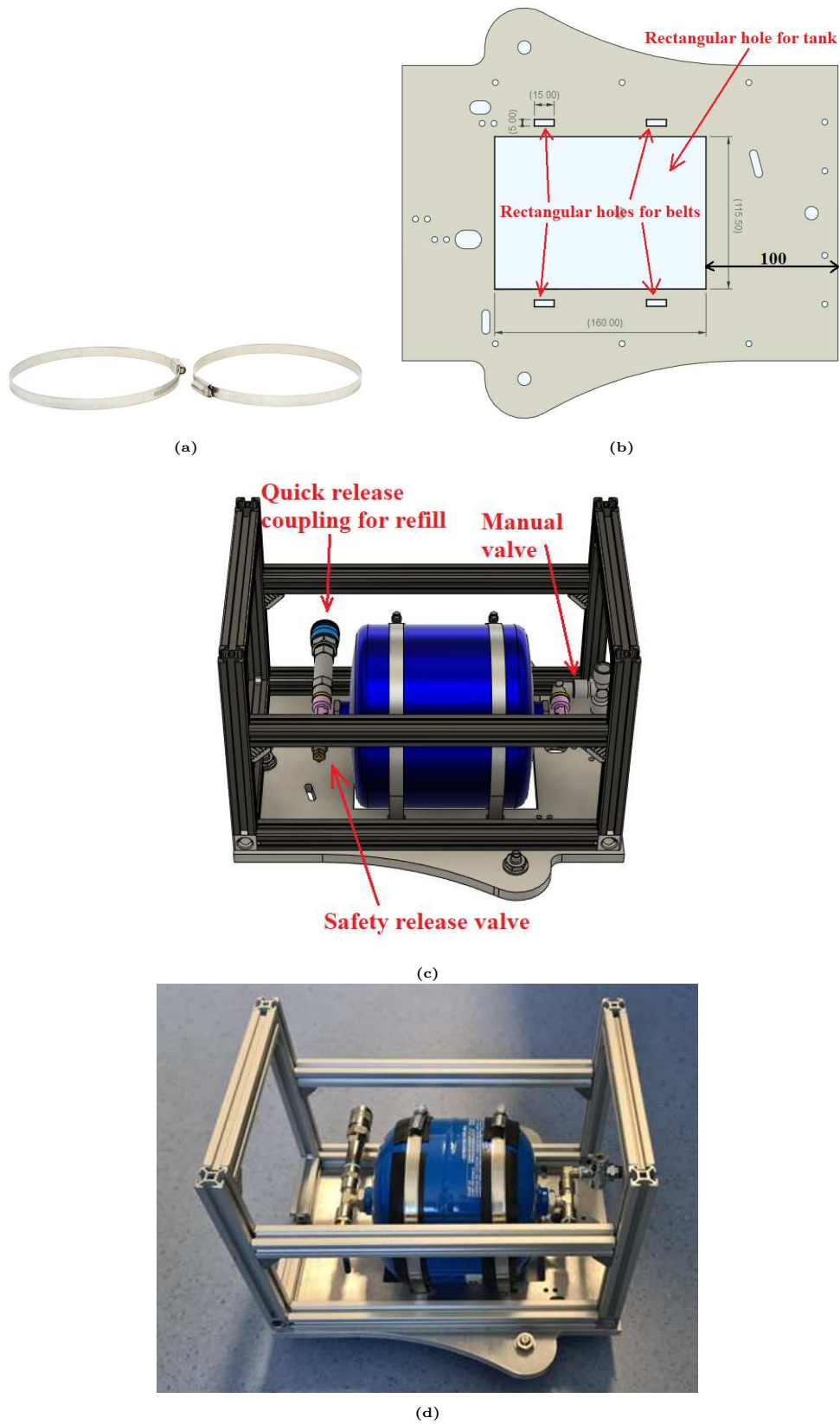
Figure 3.10: (a) Belt supports, (b) rectangular holes on the bottom wall, (c) CAD model and (d) assembly of the mounted tank.

3.2   Mid wall assembly

As stated in the previous Section, the main structural frame of the final design has been created to allow the mounting of an internal polycarbonate wall, defined as mid wall. Therefore, the mid wall assembly includes:

1. The mid polycarbonate wall with a 5 mm thickness;

2. The eight nozzle EVs;

3. The EV dedicated to the ABs;

4. The pressure regulator;

5. All pneumatic connections between the pressure regulator to the EVs and the EVs to the nozzles;

6. The two Raspberry Pi 3B electronic boards with three additional shields (Io Pi Plus, ADC Pi and Servo Pi Zero).

The mid wall is designed with overall dimensions of $227 \times 218 \, \text{mm}^2$, so that its front edge ends up exactly at the end of the avaialble $230 \times 224 \times 224 \, \text{mm}^2$ volume. Figure 3.11 shows the mid wall mounted on the vehicle.

(a)   (b)
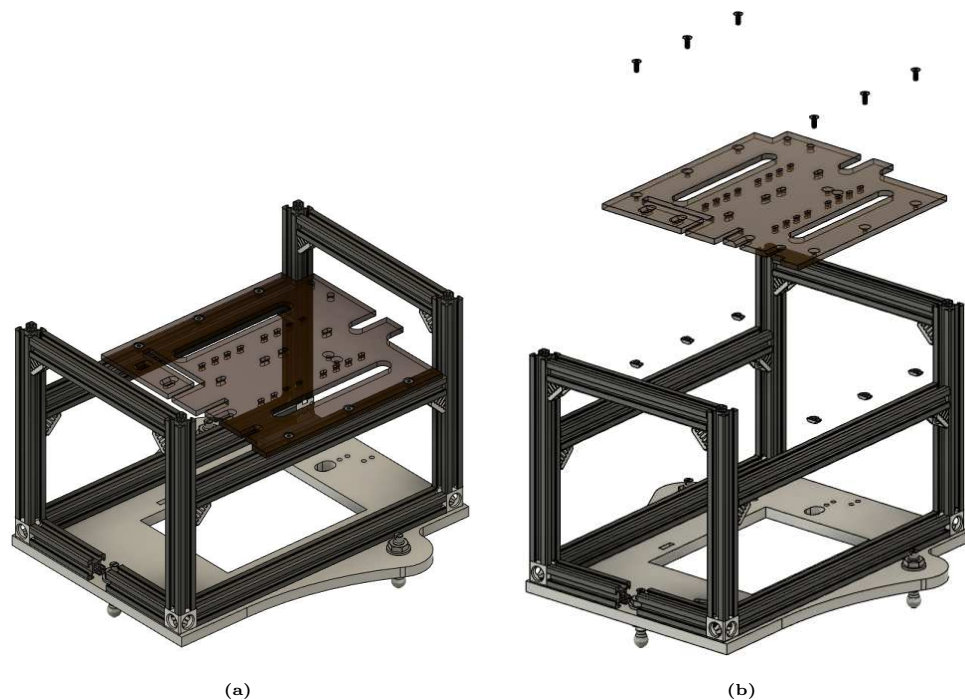
Figure 3.11: (a) Mounted mid wall and (b) exploded view.

Specifically, the mid wall has been mounted with six $M4 \times 0.7 \times 10$ mm flathead bolts on the aluminum profiles to keep its top surface flat to allow the mounting of the several components.

3.2.1   Mounting of the electro-valves

The bulky EVs of the early designs (Figure 2.6, Chapter 2) have been substituted with the 24 V EVs (model PVQ31-5G-16-01F made by *SMC*) shown in Figure 3.12.

(a)   (b)
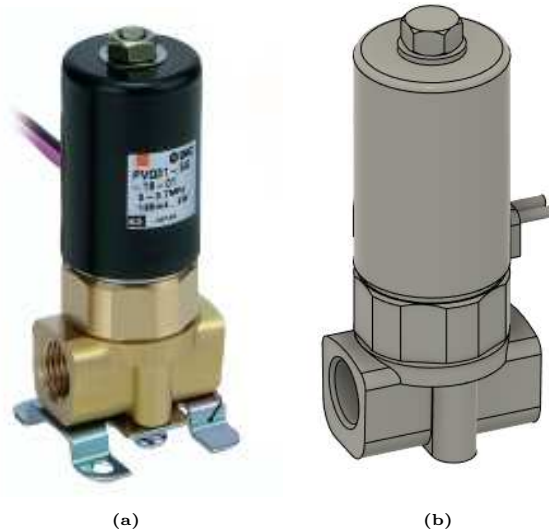
Figure 3.12: (a) New electro-valve (optional support), model PVQ31-5G-16-01F made by *SMC*, and (b) corresponding CAD model.

Despite withstanding a maximum pressure of 7 bar, which has led to the introduction of an additional safety release valve with a threshold pressure of 6 bar after the pressure regulator, the new EVs have reduced dimensions ($61 \times 25 \times 20.50$ mm^3) and much lower mass (100 g). Therefore, they allowed to realize the mid wall with flexible polycarbonate (and not aluminum, for instance), thus greatly simplifying its production process.

The eight nozzle EVs have been combined together with a nine-way pneumatic distributor into a single assembly which has been fixed onto the mid wall by using the $M3 \times 0.5 \times 5$ threaded holes of the EVs. A pneumatic two-way rotatable distributor has been mounted on each EV to link the top and bottom nozzles and two $119 \times \phi15$ slotted holes have been created on the mid wall to let one exit of the rotatable distributors through towards the bottom part of the system. Figure

3.13 presents a detail of the slotted holes for the EVs, the nozzle EVs assembly on the mid wall and a corresponding exploded view.

(a)

(b)

(c)
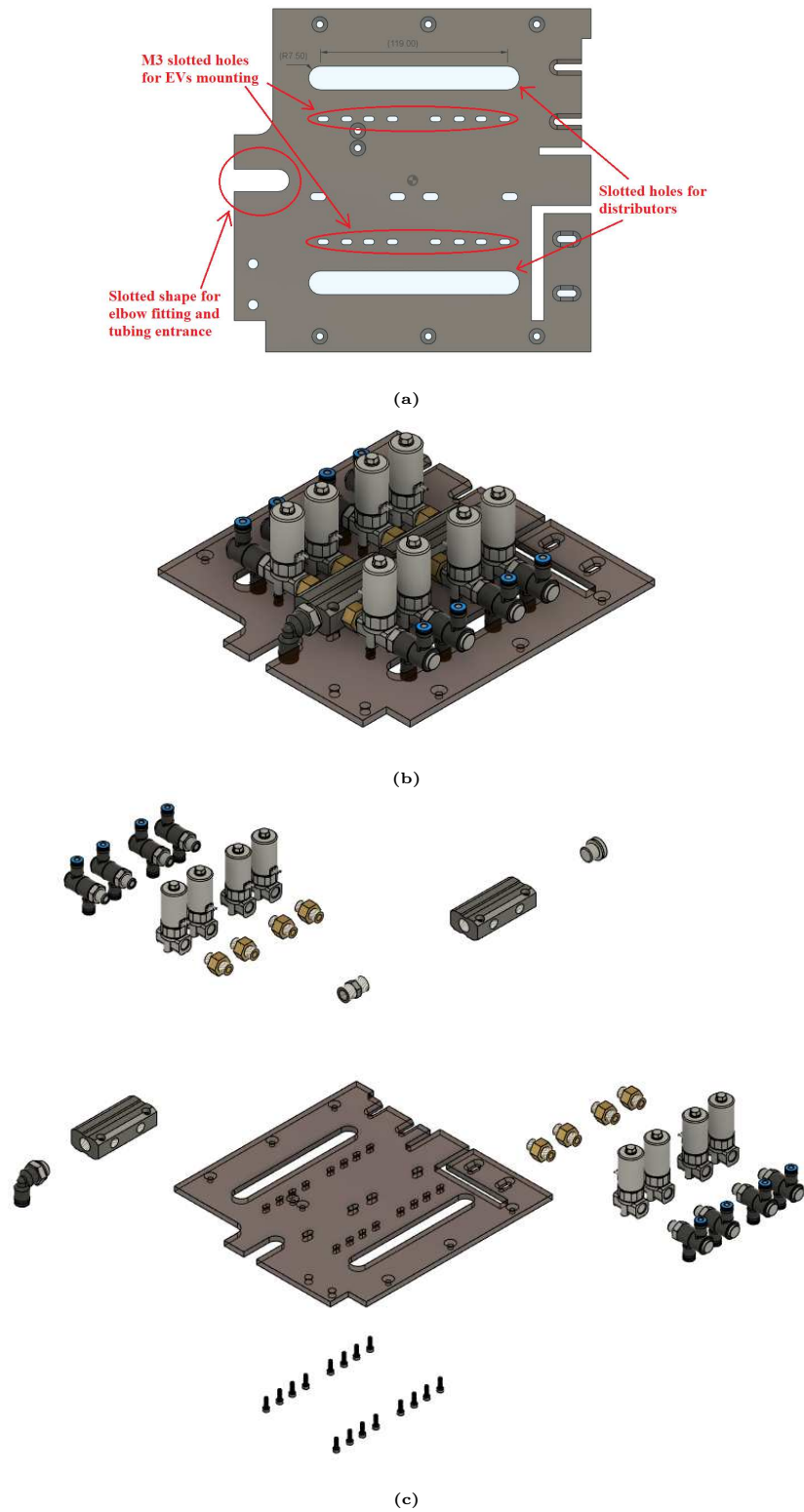
Figure 3.13: (a) Slotted holes for the EVs on the mid wall, (b) mounted nozzle EVs assembly and (c) exploded view.

The EV dedicated to the ABs has been mounted on a 3D printed support. This support has been designed with an L shape and fixed under the mid wall with two M4 flathead bolts and nuts in a "drawer" configuration to prevent facilitate mounting with the 2.5 L tank right under. Furthermore, the ABs EV has been combined with a 3 way rotatable distributor to link it to the ABs with 3 tubes of the same length to equalize the pressure losses and ensure uniform floating. Figure 3.14 illustrates the mounted ABs EV and a corresponding exploded view.

(a)

(b)
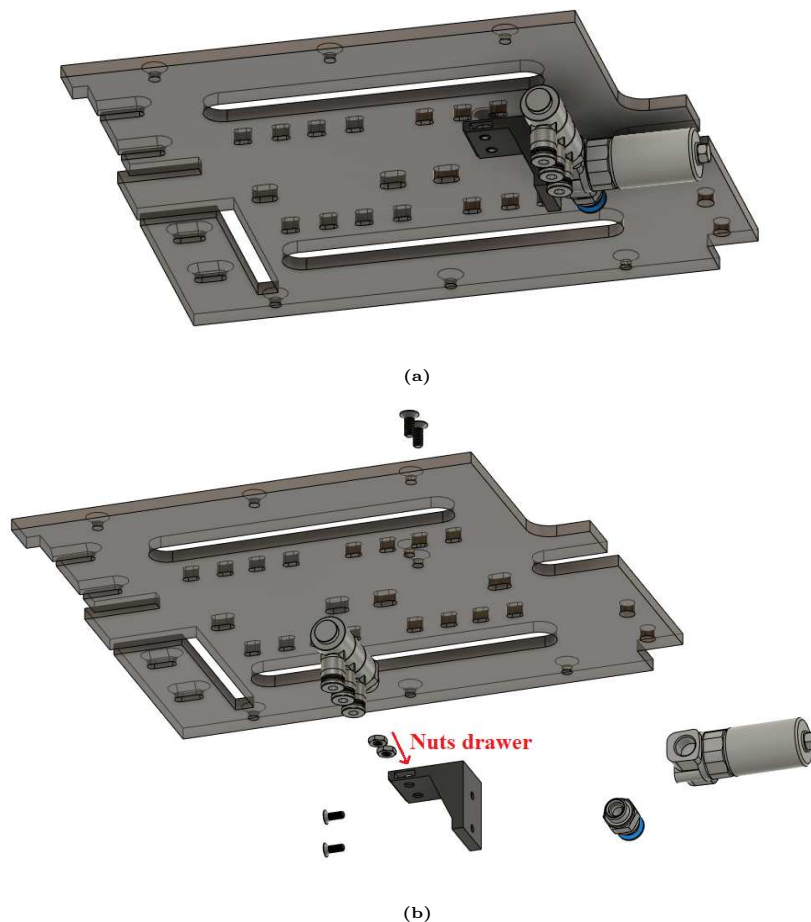
Figure 3.14: (a) Mounted ABs EV and (b) exploded view.

3.2.2 Mounting of the pressure regulator

The pressure regulator of Figure 2.7 (Chapter 2) has been fixed on the bottom part of the mid wall with its mounting bracket, so that the integrated manometer and the adjustable knob would slighty exceed the borders of the total $330 \times 224 \times 224 \,\mathrm{mm}^3$ volume. Therefore, the pressure regulator is operable from the outside at any time, even with the mounted polycarbonate external walls. Additionally, a 2 parallel way pneumatic distributor has been added to the pressure regulator exit

to link both the ABs and the EVs assembly, hence they operate at approximately the same pressure. This pneumatic fitting has required the introduction of two 20 mm standoffs on the mounting staff to avoid a conflict with the mid wall. Figure 3.15 shows the mounted pressure regulator, a corresponding exploded view and a detail with the main structural frame.
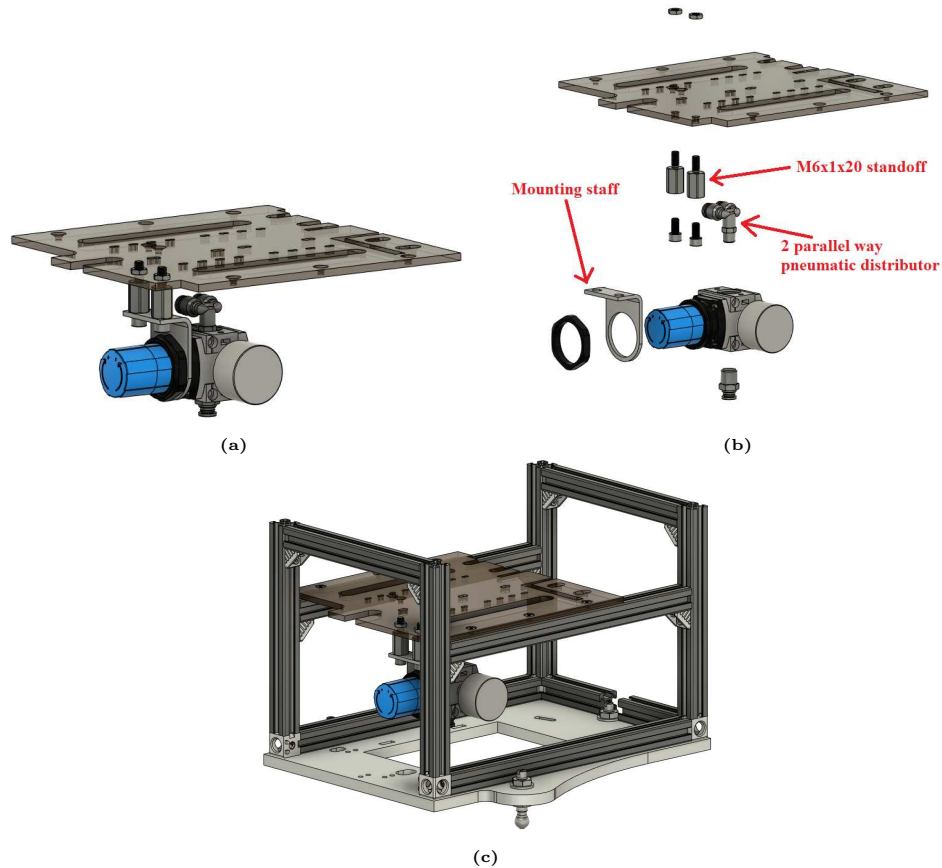
Figure 3.15: (a) Mounted pressure regulator, (b) exploded view and (c) detail with the main structural frame.

3.2.3 Mounting of the Raspberry Pi 3B electronic boards

The two Rapberry Pi 3B electronic boards have been fixed to the front edge of the mid wall with 3D printed identical supports. These supports have an L shape to hold the electronic board in a vertical configuration, thus the several ports (USB, HDMI, etc.) can be easily accessed from the top and the side, even with the mounted external polycarbonate walls. Furthermore, the two Raspberries have been mounted in an asymmetrical configuration, so that one faces the nozzle EVs assembly and, therefore, is dedicated to them, while the other faces the $100 \times 224 \times 224 \, mm^3$ volume and, therefore, is dedicated to the payload. Figure 3.16 presents the Raspberry assembly (with exploded view), a detail of

the holes and openings of the mid wall dedicated to the assemblies and the Rasp-
berries mounted on the mid wall. The assemblies include three additional shields
on the Raspberries (the 3D printed supports and openings on the mid wall have
been designed to account for the additional space occupied by the shields)

(a)   (b)

(c)
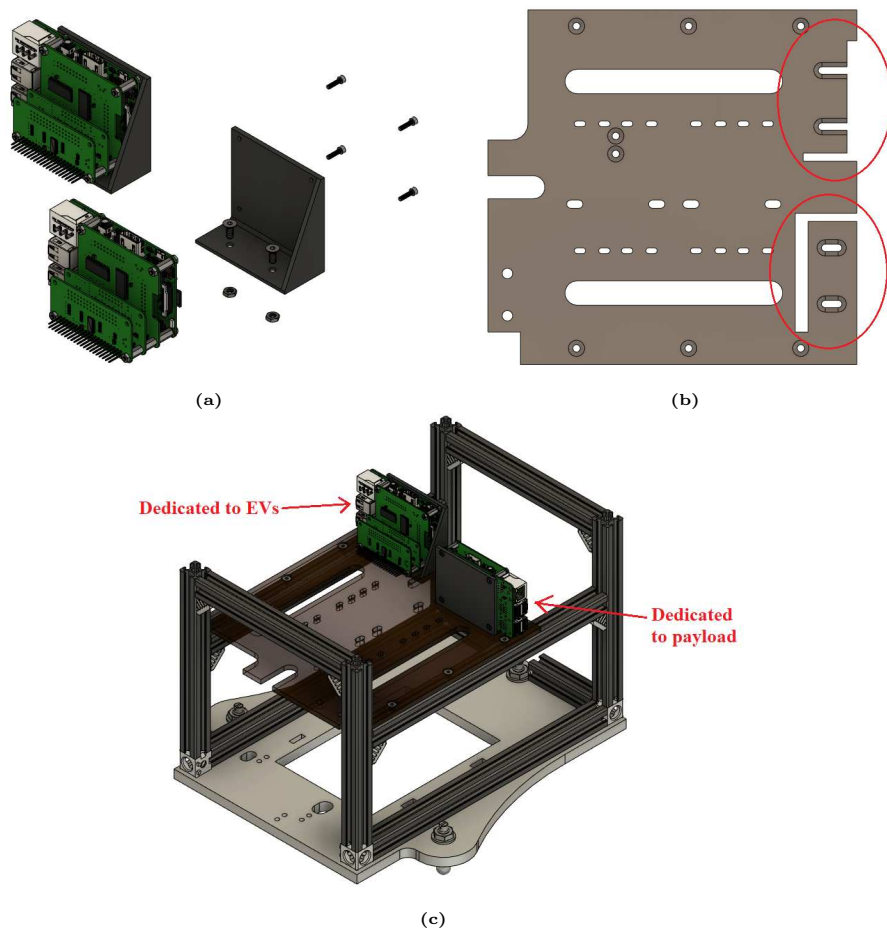
Figure 3.16: (a) Raspberry Pi 3 assembly (with exploded view), (b) dedicated holes and openings
on the mid wall and (c) assemblies mounted on the mid wall.

3.2.4   Overall assembly

Figure 3.17 shows the overall mid wall assembly and its mounting on the main
structural frame.
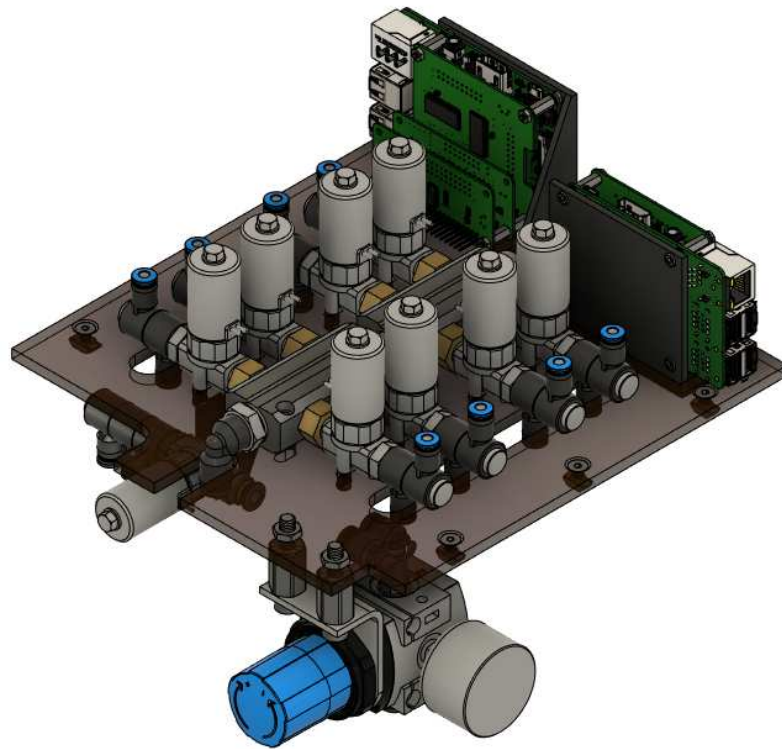
(a)
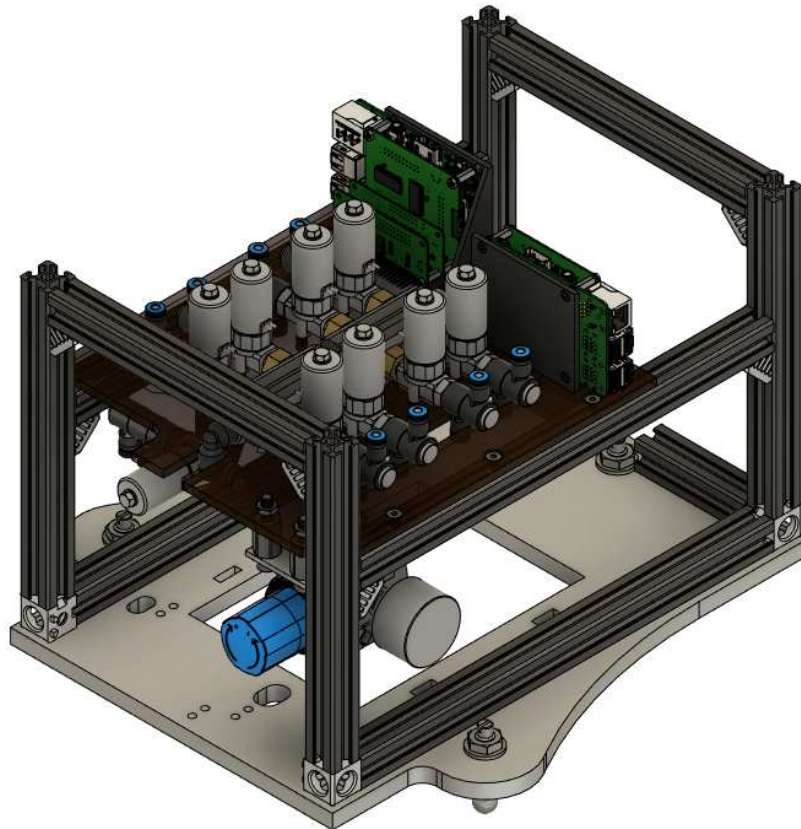
(b)

Figure 3.17: (a) Mid wall assembly and (b) mounting on the main structural frame.

3.3   Sizing and mounting of the battery

An estimation of the total power consuption has been necessary to choose 1 or 2 24 V batteries to be mounted on the vehicle to power the several electronic components.

3.3.1   Sizing of the battery

The power consumption estimation has been obtained by considering the Worst Case Scenario (WCS) of the nine EVs in a fully opened configuration and the Raspberries under a 400% CPU stess. Therefore, the main electrical circuit has included the following components:

- Nine solenoid 24 V electro-valves, power consumption $P_{EV} = 4$ W each (WCS);

- Two Raspberry Pi 3B electronic boards, power consumption $P_{RB} = 3.7$ W at 5 V ($I_{RB} = 0.730$ mA as output under the WCS) [4];

- Nine IC Mosfets for EVs control, maximum drain source resistance $R_{DS} = 3.3$ mΩ;

- A step-down converter to convert the 24 V into 5 V to power the Raspberries and Mosfets, efficiency $\eta = 0.96$.

Figure 3.18 shows the IC Mosfet and the step-down converter which have been included in the fully assembled module of Figure 3.2b.

(a)   (b)
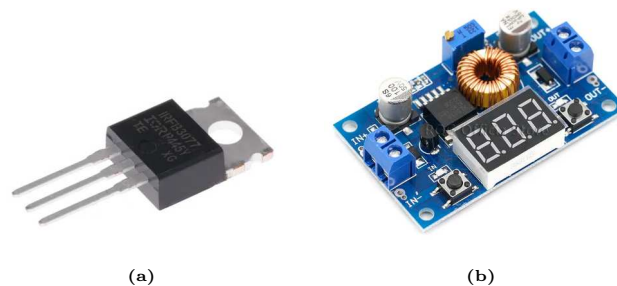
Figure 3.18: (a) IC Mosfet and (b) step-down converter.

Given the efficiency η, the step-down converter generates an additional power consumption which depends on the total power consumption of the connected

components (two Raspberries and nine Mosfets). Therefore, the consumed power P_{SD} of the step-down has been evaluated as:

$$P_{SD} = (2P_{RB}+9R_{DS}I_{RB})+(1-\eta)(2P_{RB}+9R_{DS}I_{RB}) = (2-\eta)(2P_{RB}+9R_{DS}I_{RB}) = 7.7\,\text{W}$$

The total estimated power P_{tot} in the WCS has been estimated as:

$$P_{tot} = 9P_{EV} + P_{SD} = 43.7\,\text{W}$$

At $V_a = 24\,\text{V}$, the overall output current I_a is:

$$I_a = \frac{P_{tot}}{V_a} = 1.8\,\text{A}$$

Therefore, the required estimated capacity C_a for 3 min of functioning (pneumatic system requirement) is:

$$C_a = I_a\frac{3}{60} = 0.1\,\text{A h}$$

Thanks to the relatively contained value of C_a and to save space behind the tank for additional pneumatic components and tubing, a configuration of a single 24 V battery has been chosen. In particular, a rechargeable 24 V NiMH (Nichel Metal Hydride) battery (made by RS Pro) with a capacity of 2 A h, dimensions of $101 \times 74 \times 34.5\,\text{mm}^3$ and mass of 500 g has been chosen. Figure 3.19 shows the battery and corresponding CAD model.

(a)   (b)
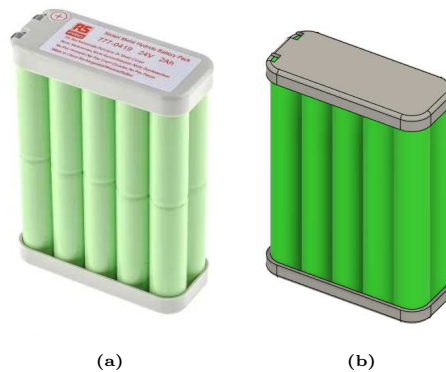
Figure 3.19: (a) Rechargeable 24 V 2 A h NiMH battery made by RS Pro and (b) CAD model.

3.3.2   Mounting of the battery

The battery has been encased in a 3D printed support and fixed on the main structural frame. The assembly has been designed so that the battery can be

removed at any time for substitution or recharge, even with the mounted external polycarbonate walls. Figure 3.20 illustrates the battery assembly, a corresponding exploded view and its mounting on the main structural frame.

(a)   (b)

(c)
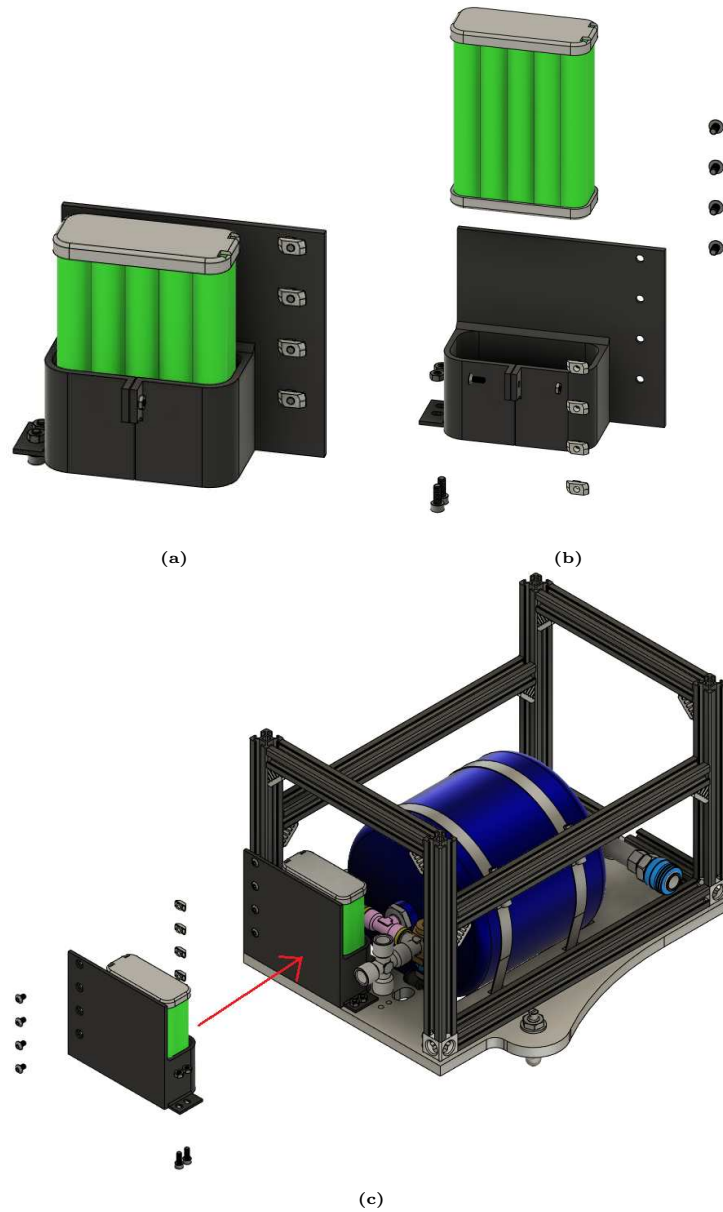
Figure 3.20: (a) Battery assembly, (b) exploded view and (c) mounting on the main structural frame.

3.4   External polycarbonate walls

With respect to the early designs, the external polycarbonate walls have been modified to a 3 mm thickness and to act as simple covers without any structural functionality. Therefore, the module is fully functioning with or without them (for

instance, the assembled system of Figure 3.2b used for all tests does not include the external walls). Figure 3.21 shows the mounted external polycarbonate walls and a corresponding exploded view.

(a)

(b)
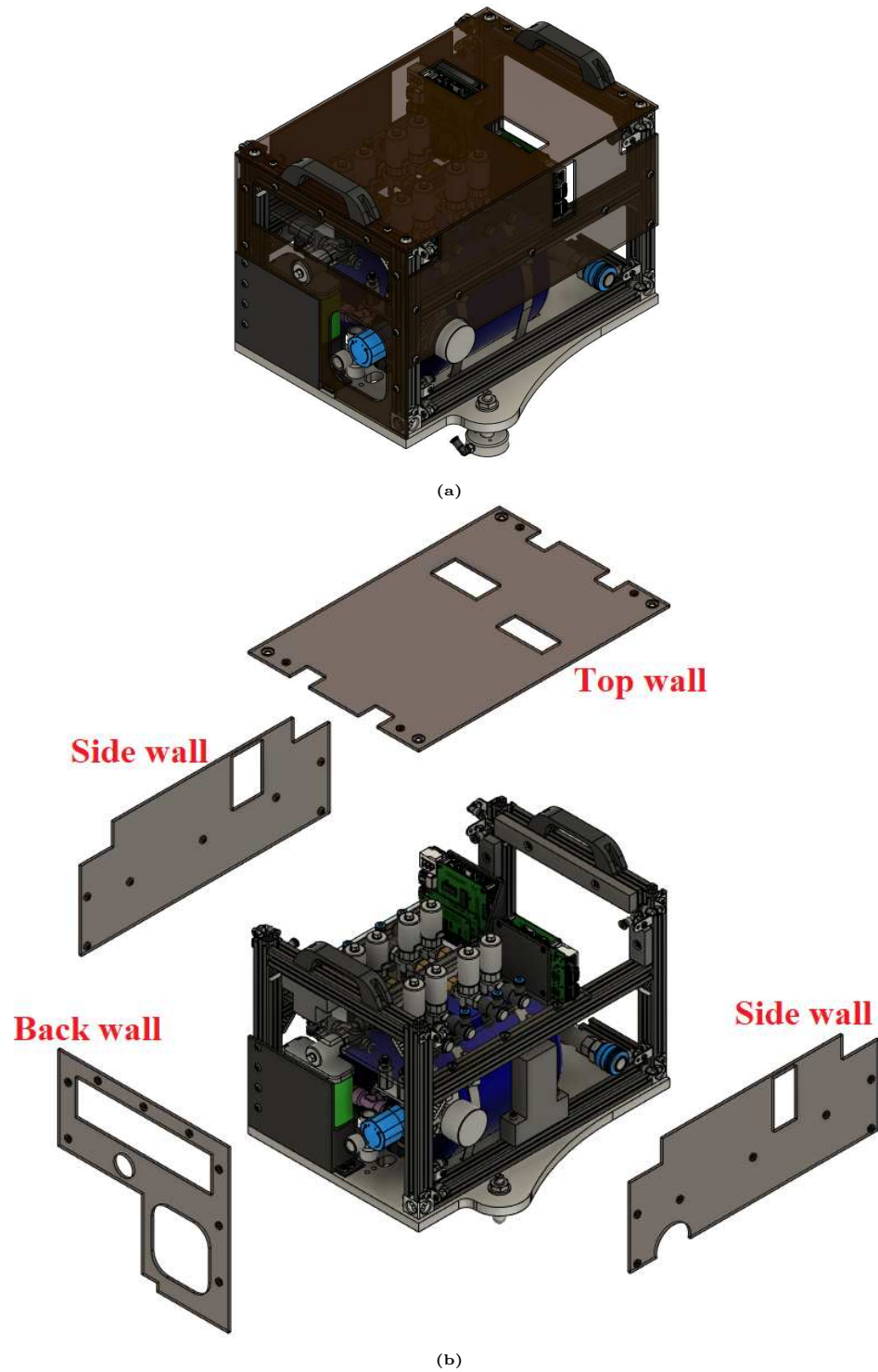
Figure 3.21: (a) Mounted external polycarbonate walls and (b) exploded view.

3.4.1   Top wall

Figure 3.22 presents a detail of the several openings of the top wall.
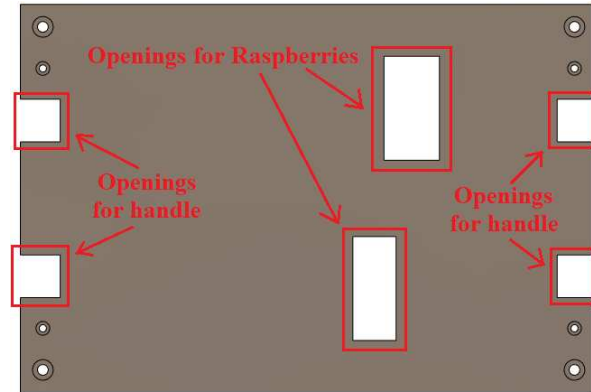
Figure 3.22: Detail of the openings of the top wall.

3.4.2   Back wall

Figure 3.22 presents a detail of the several openings of the back wall.
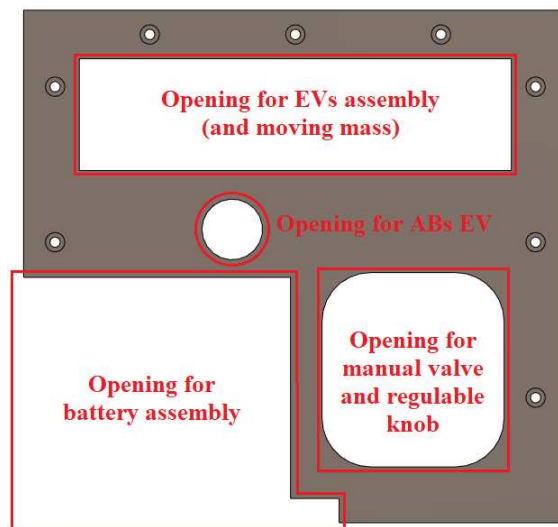
Figure 3.23: Detail of the openings of the back wall.

3.4.3   Side walls

Figure 3.24 presents a detail of the several openings of the side walls. Additionally, the side walls leave the bottom part of the vehicle open to access the internal components (and the movable masses, see Section 3.5)
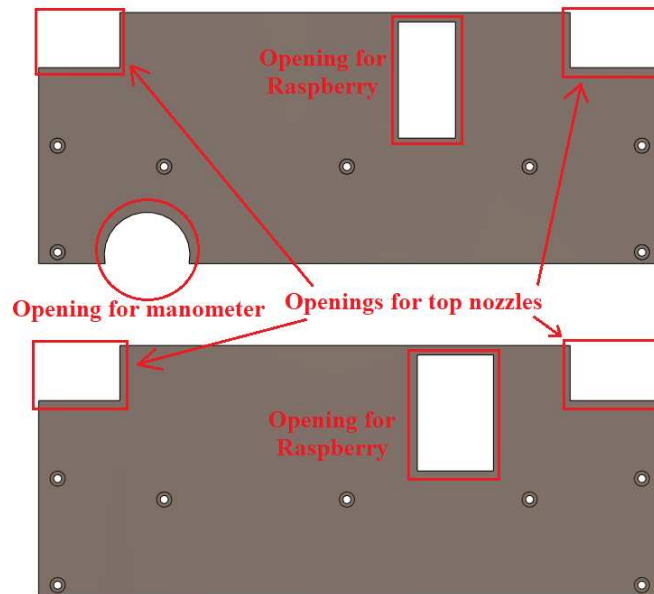
Figure 3.24: Detail of the openings of the side walls.

3.5 Fixed and movable masses system

The concluding part of the mechanical and final design of the module has been dedicated to finding a solution to satisfy the major requirement of aligning the CoM position of the system with the ABs centroid to ensure pure rotational motions. Specifically, since the ABs and nozzles centroid have been aligned with the GC of the module (see Section 3.1), the goal has been to control the CoM position to be coincident with said GC.

A possible method to control the position of the CoM of a system is the realization of custom masses which can be moved either manually [5] or automatically with motors [6]. For this reason, the design of a group of manually movable steel masses has been considered as an achievable solution for the vehicle. Their masses and dimensions have been determined from the CAD model estimation of the total mass and CoM position of the module.

In the following sections, the position of the several components and assemblies are expressed with the X and Y coordinates of the main reference frame at the GC of the module of Figures 3.2a and 3.7. Furthermore, the Z coordinates are not considered, because the CoM position along the main rotational axis (Z axis) is irrelevant to ensure a 3-DoF planar motion and pure rotations.

3.5.1   Estimation of the CoM position from the CAD model

An estimation of the total mass and CoM position has been necessary to understand how much mass would be required to significantly shift the CoM location. The estimation has been performed on the CAD model of Figure 3.21a and has followed the subsequent assumptions:

1. The masses of all components have been derived (depending on the component):

    - By directly measuring them on a scale (i.e. : tank and tank belts, electro-valves, pressure regulator, bottom wall, mid wall, pneumatic connections/fittings);

    - From the available datasheets (i.e. : battery, Raspberriy Pi 3B and shields);

    - From the density of the known material and volume (i.e. : strut profiles of the structural frame, 3D printed supports, external polycarbonate walls, bolts, nuts, screws)

2. Every component has been approximated as a homogeneous body with a custom density (when necessary) to set the proper mass;

3. The ABs have not been included, because they are not fixed on the module;

4. The electrical wiring has not been considered;

5. To account for a generic mounted payload in the front part of the vehicle, a homogeneous body with the following mass and CoM position has been considered:

$$m_{PA} = 1\,\text{kg}$$

$$\vec{r}_{PA} = \begin{pmatrix} 175 \\ 0 \end{pmatrix}\,\text{mm} \quad \text{To place it } 10\,\text{mm outside of the front border}$$

Therefore, the following list of the several assemblies with corresponding estimated masses and CoM positions is presented:

- Structural frame assembly (whose main components are the aluminum strut

profiles):

$$m_{SF} = 1.287 \, \text{kg}$$

$$\vec{r}_{SF} = \begin{pmatrix} 9.69 \\ 0 \end{pmatrix} \text{mm}$$

- Bottom wall assembly (whose main components are the bottom aluminum wall, the 2.5 L tank with the mounted pneumatic connections, the battery assembly and the ABs ball mounting screws)*:

$$m_{BWA} = 4.547 \, \text{kg}$$

$$\vec{r}_{BWA} = \begin{pmatrix} -23.59 \\ 1.53 \end{pmatrix} \text{mm}$$

- Mid wall assembly (Figure 3.17a):

$$m_{MWA} = 2.132 \, \text{kg}$$

$$\vec{r}_{MWA} = \begin{pmatrix} -58.96 \\ -7.12 \end{pmatrix} \text{mm}$$

- Nozzles assembly:

$$m_{NA} = 0.125 \, \text{kg}$$

$$\vec{r}_{NA} = \begin{pmatrix} 4.04 \\ 0 \end{pmatrix} \text{mm}$$

- External polycarbonate walls assembly:

$$m_{EWA} = 0.665 \, \text{kg}$$

$$\vec{r}_{EWA} = \begin{pmatrix} -24.16 \\ -2.22 \end{pmatrix} \text{mm}$$

---

*The mounted pneumatic connections amount to an overall mass of 0.566 kg, which represents the 38.5% of the 1.472 kg of the tank

- Tubing (estimated from earlier, but similar CAD models of the final design):

$$m_{TU} = 0.048\,\text{kg}$$

$$\vec{r}_{TU} = \begin{pmatrix} -43.88 \\ 4.59 \end{pmatrix} \text{mm}$$

Hence, the mass and CoM position of the floating module are:

$$m_{FM} = m_{PA} + m_{SF} + m_{BWA} + m_{MWA} + m_{NA} + m_{EWA} + m_{TU} = 9.804\,\text{kg}$$

$$\vec{r}_{FM} = \frac{1}{m_{LM}}(m_{PA}\vec{r}_{PA} + m_{SF}\vec{r}_{SF} + m_{BWA}\vec{r}_{BWA} + m_{MWA}\vec{r}_{MWA} + m_{NA}\vec{r}_{NA} +$$

$$+ m_{EWA}\vec{r}_{EWA} + m_{TU}\vec{r}_{TU}) = \begin{pmatrix} x_{FM} \\ y_{FM} \end{pmatrix} = \begin{pmatrix} -6.44 \\ -0.97 \end{pmatrix} \text{mm}$$

For the sake of the performed measurements (see Chapter 4), the mass and CoM position *without* the external walls and the payload are:

$$m'_{FM} = 8.139\,\text{kg} \tag{3.1}$$

$$\vec{r}'_{FM} = \begin{pmatrix} -27.29 \\ -0.99 \end{pmatrix} \text{mm} \tag{3.2}$$

$\vec{r}_{FM}$ shows how the X coordinate of the CoM is the most critical one.

From the values of m_{FM} and $\vec{r}_{FM}$, the required masses along the X (m_{m_x}) and Y (m_{m_y}) coordinates to align the CoM at the GC (origin of the main reference frame) have been calculated:

$$\frac{m_{FM}x_{FM} + m_{m_x}(x)x}{m_{FM} + m_{m_x}} = 0 \qquad \Longrightarrow \qquad m_{m_x}(x) = -m_{FM}\frac{x_{FM}}{x}$$

$$\frac{m_{FM}y_{FM} + m_{m_y}(y)y}{m_{FM} + m_{m_y}} = 0 \qquad \Longrightarrow \qquad m_{m_y}(y) = -m_{FM}\frac{y_{FM}}{y}$$

Figure 3.25 shows the required masses $m_{m_x}(x)$ and $m_{m_y}(y)$ in the X and Y intervals of $[20, 165]$mm and $[20, 112]$mm respectively (the interval extremes have been chosen to start relatively close to the origin and to end at the borders of the $330 \times 224\,\text{mm}^2$ available space).
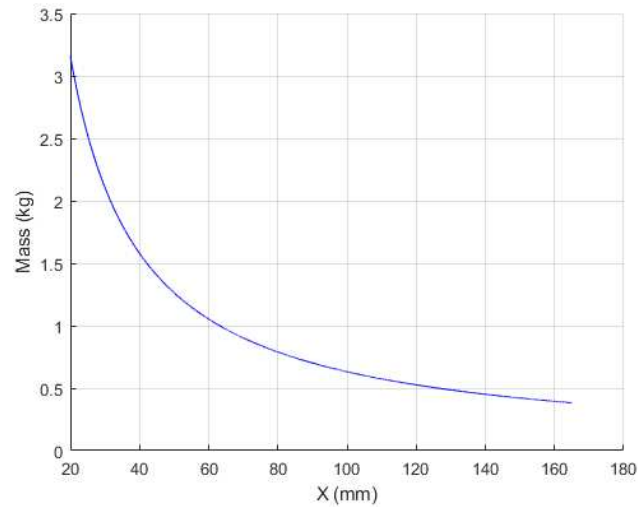
(a)
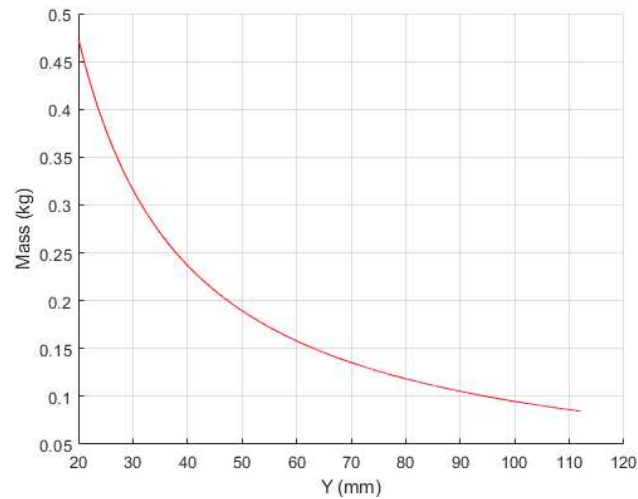
(b)

Figure 3.25: (a) Required moving masses along X and (b) required moving masses along Y.

Once again, Figure 3.25b proves how the control of the X coordinate is the most critical in terms of required mass to be moved.

Therefore, it has been decided to create two distinct systems of steel movable masses to control the X and Y coordinates separately and to take advantage of the aluminum profiles of the structure by using them as guides. Figure 3.26 shows a detail of where the movable masses have been mounted.
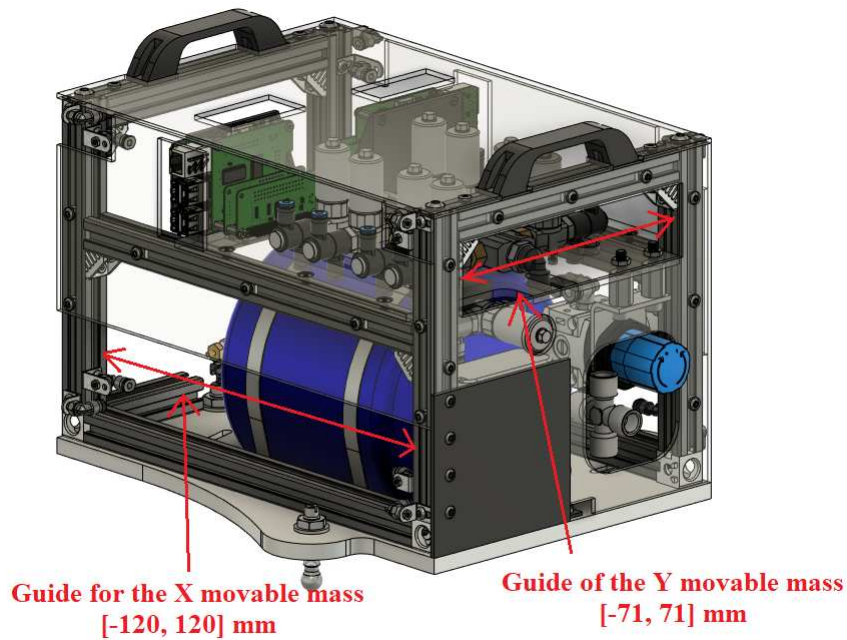
Figure 3.26: Guides for the X and Y movable masses.

For the X movable mass, an additional counterweight on the opposite side of the tank has also been considered to avoid an unnecessary displacement of the Y coordinate.

Furthermore, a set of fixed steel masses to be mounted on the front part of the vehicle has been designed to:

- Bring the CoM closer to the GC;

- Account for the additional X coordinate displacement of the CoM caused by the Y movable mass mounted in the back part of the vehicle;

- Get closer to the goal of a total system mass of 12 kg.

3.5.2   Fixed masses system

The fixed steel masses have been designed to be easily manufactured. The set has included 5 masses which all share a parallelepiped shape with dimensions of $L \times 20 \times 10 \, \text{mm}^3$, where L varies between the 5 of them. The 10 mm and 20 mm dimensions have been chosen to occupy as little space as possible in the front part of the vehicle where the payload will be located. Figure 3.27 presents the 5 fixed masses and an exploded view.
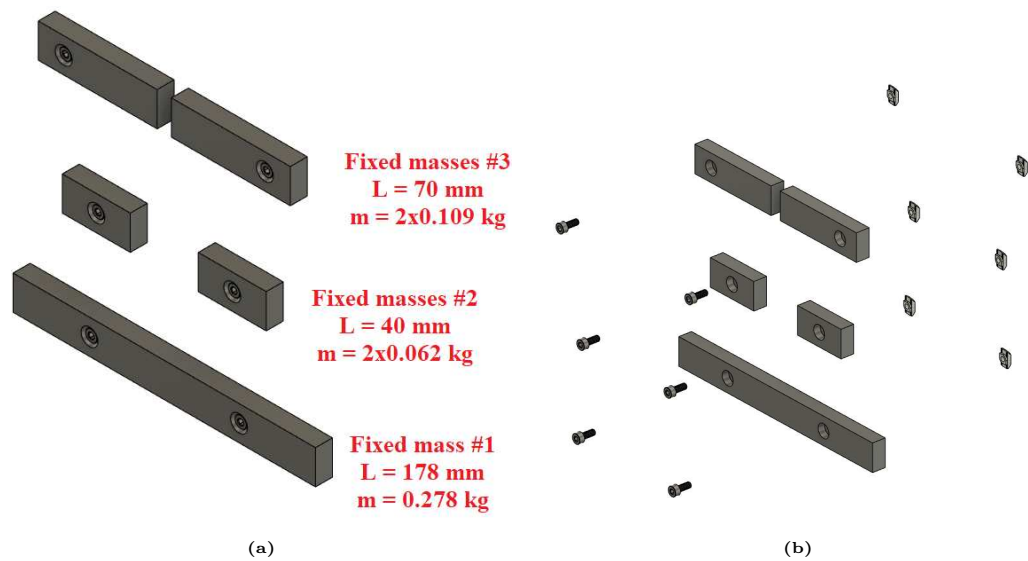
Figure 3.27: (a) Fixed steel masses (the masses values include the nuts and bolts) and (b) exploded view.

The total mass of the set amounts to $0.620\,\mathrm{kg}$.

Figure 3.28 illustrates the 5 fixed masses mounted on the structure of the module (they are symmetrical with respect to the Y axis because the Y coordinate $y_{FM} = -0.97\,\mathrm{mm}$ is already close enough to the GC).
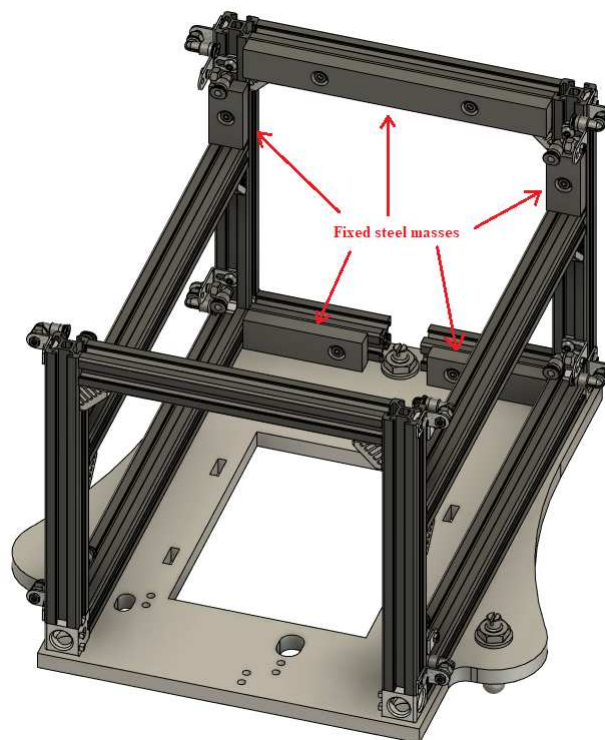
Figure 3.28: Mounted fixed masses.

With the 5 fixed masses in position, a $1\,\mathrm{kg}$ of a generic payload and without the external polycarbonate walls, the estimated mass and CoM of the module have become:

$$m_{FM} = 8.139\,\mathrm{kg} + 1\,\mathrm{kg} + 0.620\,\mathrm{kg} = 9.759\,\mathrm{kg} \tag{3.3}$$

$$\vec{r}_{FM} = \begin{pmatrix} 4.10 \\ -0.82 \end{pmatrix} \mathrm{mm} \tag{3.4}$$

The X coordinate has become greater than 0 to compensate the Y movable mass in the back.

3.5.3   Movable masses system

Initial ideas have revolved around the study of configurations with worm drives to slide the X and Y movable masses along the strut profiles of Figure 3.26. Specifically, two possibilities have been explored:

1. Movable masses with a parallelepiped shape to be moved by rotating the worm drive (Figure 3.29);
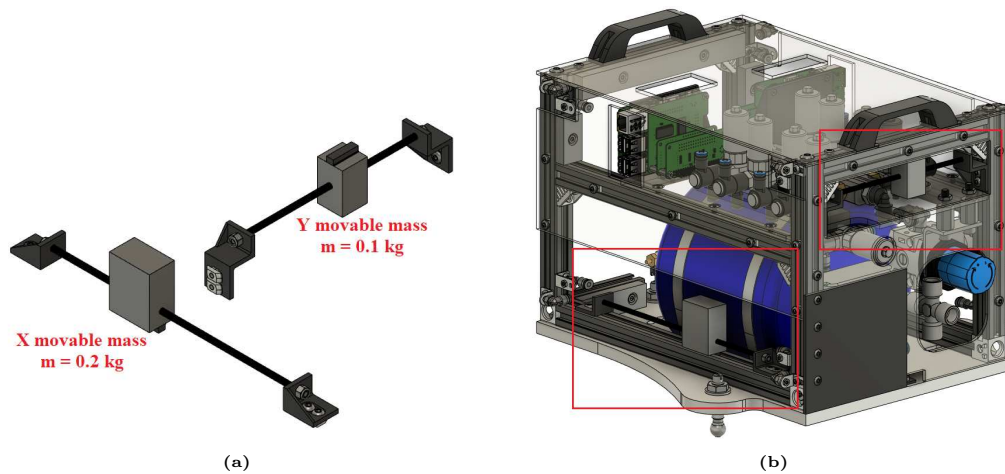
Figure 3.29: (a) First configuration for movable masses and (b) view on the module.

2. Movable masses with a cylindrical shape to be moved by rotating them on the worm drive (Figure 3.30).
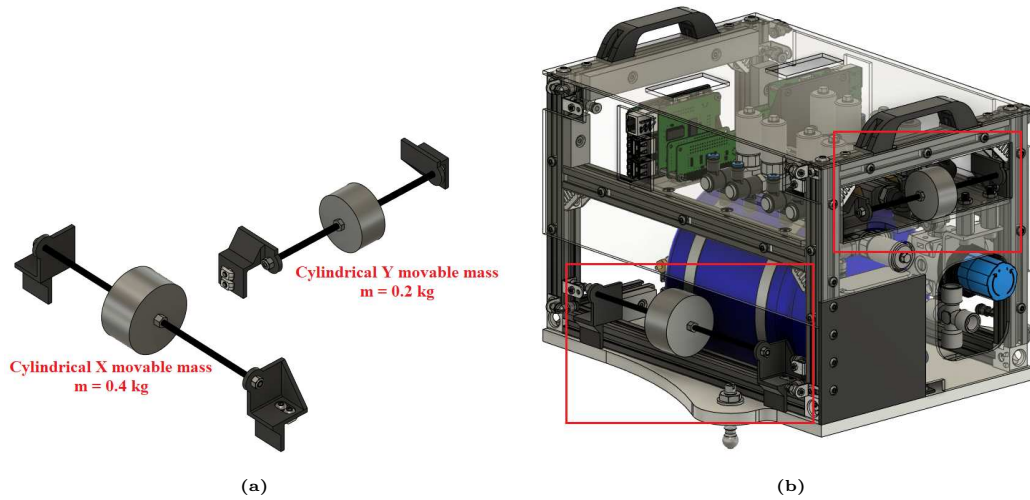
Figure 3.30: (a) Second configuration for movable masses and (b) view on the module.

Unfortunately, due to time limitations and other issues (e.g.: the first configuration having a reduced mass to control the CoM, the second one exceeding the borders and having movable masses with a complex manufacturing, the impossibility to integrate motors), a much simpler, but effective solution has been identified for the final design of the module.

This solution has involved the design of 3 steel blocks to be directly mounted and manually slided on the strut profiles of the structure. In particular, 2 of the 3 blocks have been made symmetrical with a mass of 0.687 kg each and dedicated to the control of the X coordinate, one to be moved and the other to act as a counterweight on the opposite side. The remaining smaller block with a mass of 0.240 kg has been dedicated to the control of the Y coordinate. Figure 3.31 illustrates the 3 steel blocks.
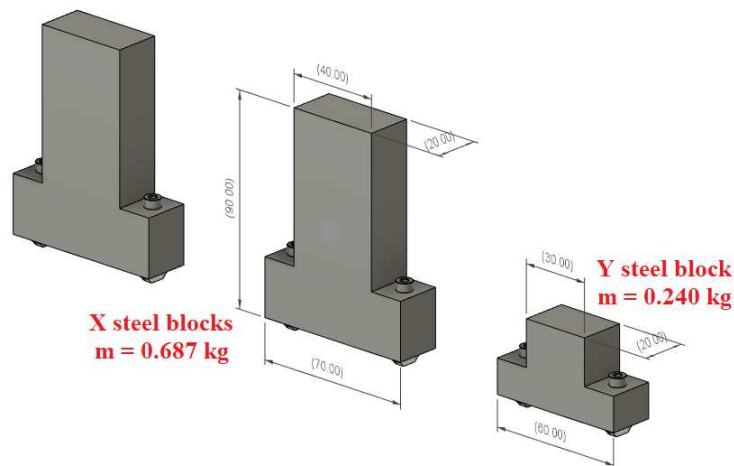
Figure 3.31: Movable masses.

Their T shapes have been designed to efficiently occupy the available space along the strut profiles to maximize their corresponding masses, while still ensuring an easy manufacturing.

Figure 3.32 presents the mounted steel blocks: the one acting as a counterweight is positioned at $x = 0$.

(a)

(b)
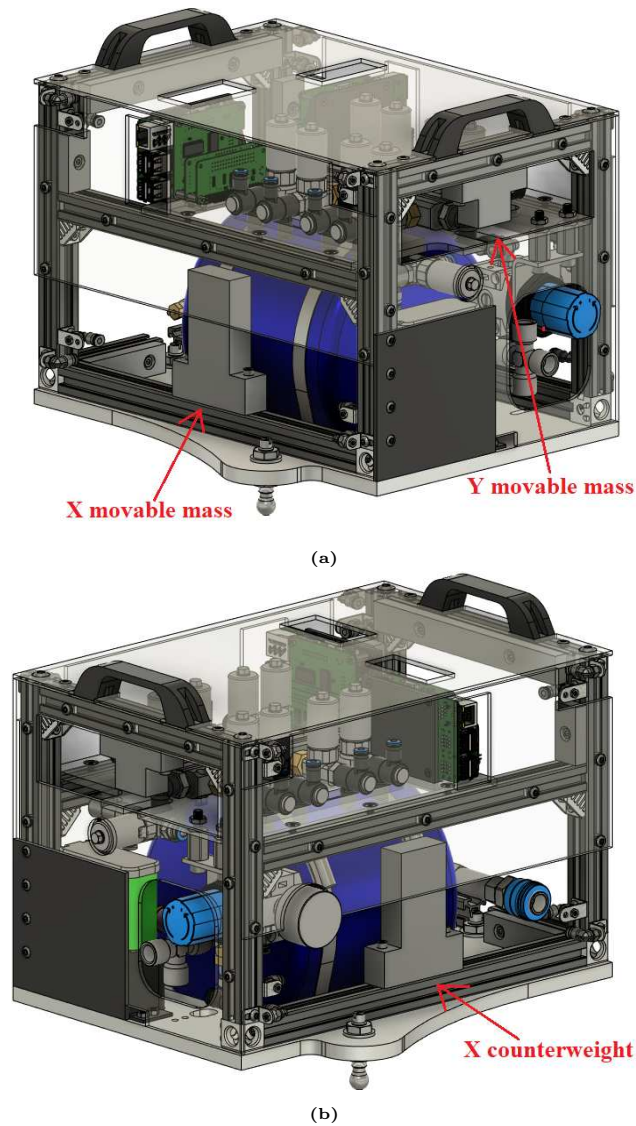
Figure 3.32: Movable steel blocks: (a) view 1 on movable masses and (b) view 2 on the counterweight.

From the CAD model of the system, the CoM of the X movable mass can be moved in a $[-91, 84]$mm range along the X axis. Figure 3.33 shows the two extreme positions of the movable mass.
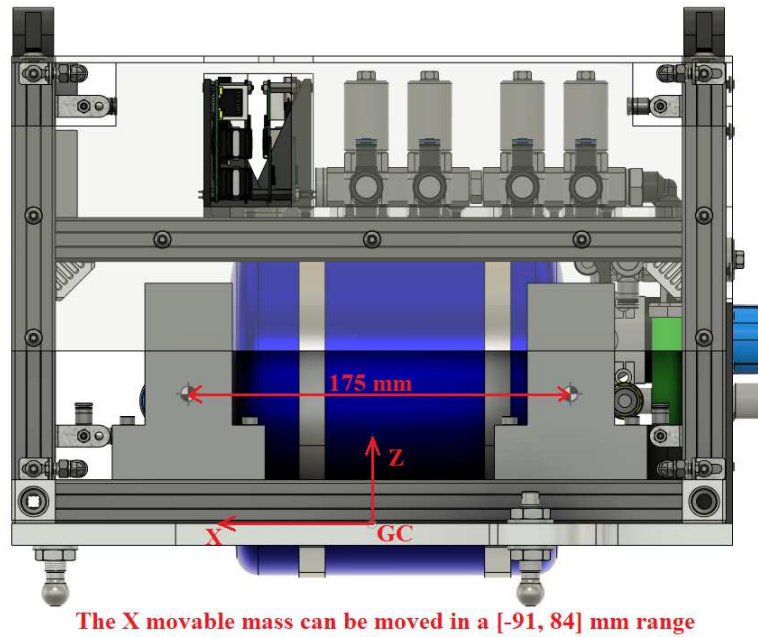
Figure 3.33: Extreme positions of the X movable mass.

Consequenty, the estimated X coordinate of the overall CoM can be shifted in a $[-3.27, 3.04]$mm range (6.31 mm total).

Similarly, the CoM of the Y movable mass can be moved in a $[-41, 41]$mm range along the Y axis. Figure 3.34 shows the two extreme positions of the movable mass.

Figure 3.34: Extreme positions of the Y movable mass.

Consequenty, the estimated Y coordinate of the overall CoM can be shifted in a $[-1.60, 0.03]$mm range ($1.63\,\mathrm{mm}$ total).

With all the mounted movable masses, the total mass of the vehicle m_{FM} has been estimated to be:

$$m_{FM} = 10.424\,\mathrm{kg} + 2 \cdot 0.687\,\mathrm{kg} + 0.240\,\mathrm{kg} = 12.038\,\mathrm{kg}$$

All the estimations of the above section have been validated by the performed measurements and tests on the floating assembled module of Figure 3.2b (see Ch. 4 for details).

Chapter 4

Procedures and setups of the performed tests

This chapter presents a description of the procedures and setups of the performed tests.

Two major tests have been performed:

1. Measurement, control and alignment of the CoM of the module around the centroid of the ABs and nozzles;

2. Estimation of the inertia around the main rotational axis.

The first test has involved the realization and use of a setup of three load cells to measure and control the CoM position: by mounting the movable masses and shifting their position along the guides, several measurements have been taken with the goal of aligning the CoM with the centroid of the ABs within an error of 1 mm. The second test has been performed by activating the thrusters of the pneumatic system to execute a serie of pure rotations (which have been achieved thanks to the alignment of the first test) around the Z axis (see Figure 3.2a, Ch. 3) on the levelled table, while tracking the module motion with a motion capture system of four cameras. The inertia of the vehicle has been estimated from the resulting angular acceleration around the main axis and the thrust of the propulsion system (the thurst values had been previously estimated by the pneumatic tests performed on the module [7]).

Figure 4.1 shows a logical scheme of the two performed test.
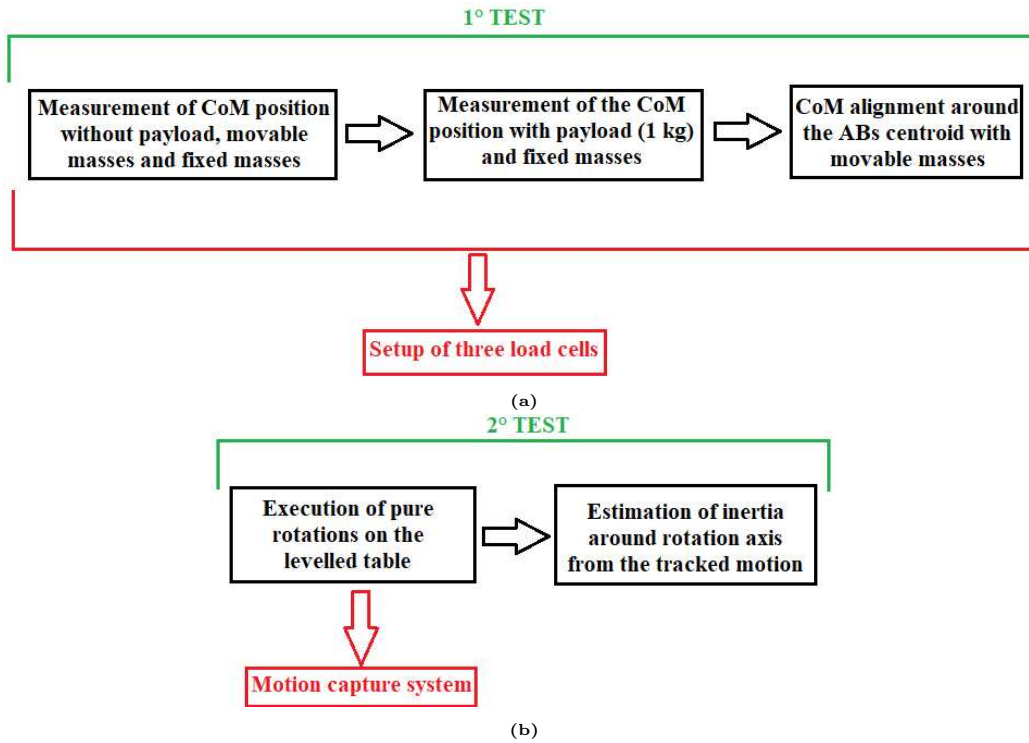
Figure 4.1: Logical schemes of (a) 1° test and (b) 2° test.

All tests have been performed on the assembled module of Figure 3.2b, which does not include the external polycarbonate walls and the air-bearings electro-valve.

4.1 Measurement, control and alignment of the CoM of the module

An achievable solution to measure the CoM position and mass of a body is the realization of a multi-point weighing system with load cells [8]. In the case of the developed floating module, a setup of three load cells has been created. By placing the load cells under the three ball mounting screws of the ABs in an equivalent equilateral triangular configuration, the goal has been to estimate the CoM position on the XY plane centered on the GC of the module (see Figure 3.2a, Ch. 3). Specifically, the first test for the control and alignment of the CoM of the module around the centroid of the ABs has involved the following steps:

1. Development of a setup of three load cells to measure the CoM position;

2. Setup of the electronic circuit to read the load cells outputs;

3. Calibration of the three separate load cells;

4. Realization of alternatives for the movable and fixed masses;

5. Measurement of the CoM position (and mass) without a payload and movable/fixed masses;

6. Measurement of the CoM position (and mass) with a generic payload of 1 kg and the alternatives for the fixed masses;

7. Alignment of the CoM around the GC within an error of 1 mm with the alternatives for the movable masses.

Steps #4 and #5 have been performed to validate the measurements of the three load cells setup and the CAD estimations of Section 3.5 (Ch. 3). The results of steps #3, #5, #6 and #7 are presented in Ch. 5.

4.1.1   Setup of three load cells

A schematic view of the developed three load cells setup can be seen in Figure 4.2.
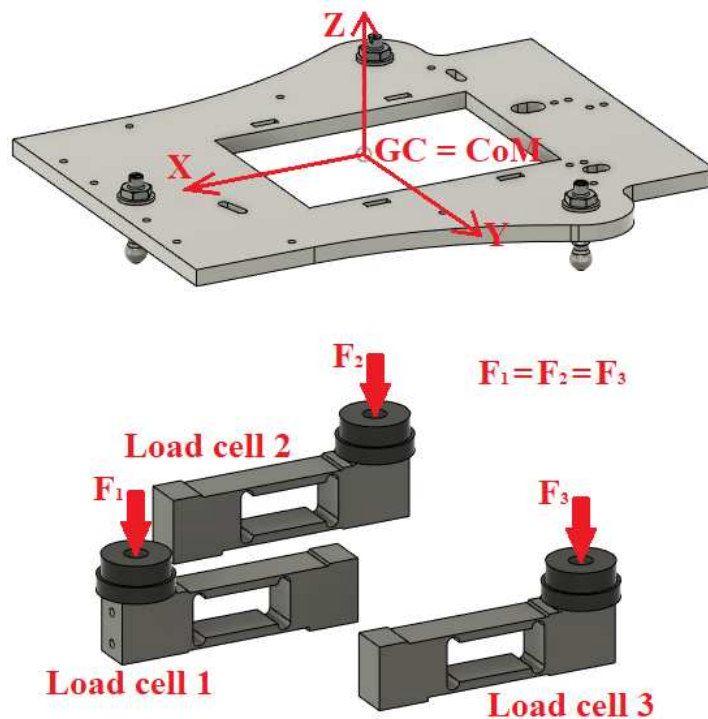
Figure 4.2: Schematic view of the three load cells setup.

Ideally, if $\vec{F}_1 = \vec{F}_2 = \vec{F}_3$, then the CoM and the GC are coincident on the XY plane. Furthermore, by knowing the geometrical positions of the ABs $\vec{r}_{AB_1}$, $\vec{r}_{AB_2}$

and $\vec{r}_{AB_3}$ from the CAD model in the XY plane and by converting F_1, F_2 and F_3 into mass values, it is possible to compute the mass m_{FM} and the CoM position $\vec{r}_{FM}$ of the module as follows:

$$
\left.\begin{array}{l}
m_1 = \frac{F_1}{g_0} \\
m_2 = \frac{F_2}{g_0} \\
m_3 = \frac{F_3}{g_0}
\end{array}\right\} \Rightarrow \left\{\begin{array}{l}
m_{FM} = m_1 + m_2 + m_3 \\
\vec{r}_{FM} = \frac{1}{m_{FM}}(m_1\vec{r}_{AB_1} + m_2\vec{r}_{AB_2} + m_3\vec{r}_{AB_3})
\end{array}\right.
\tag{4.1}
$$

Since the total estimated mass of the module is $12\,\text{kg}$, so that each load cell supports a mass of about $4\,\text{kg}$, three single point load cells with a rated load of $10\,\text{kg}$ have been chosen to have a reasonable safety margin even with a misaligned CoM. The chosen load cell, model 7MH5102-2AD00 made by *Siemens*, has a rated characteristic output of $2.0 \pm 0.2\,\text{mV V}^{-1}$ and a recommended supply voltage of $5-12\,\text{V DC}$. The chosen load cell and its technical drawing are shown in Figure 4.3.
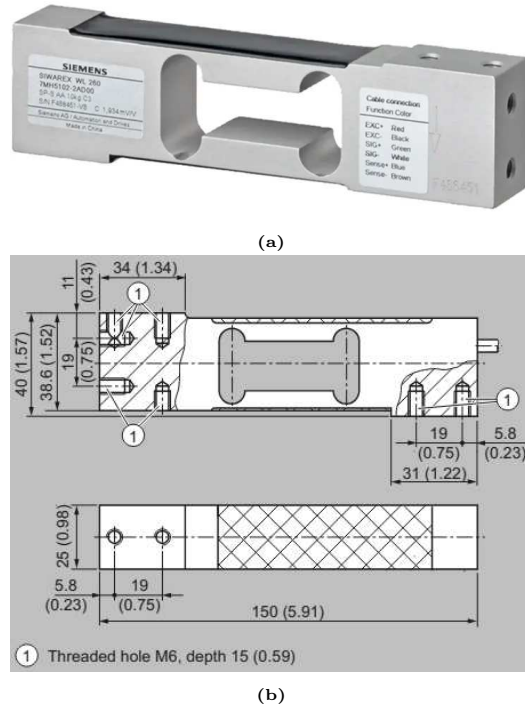
Figure 4.3: (a) 10 kg load cell, model 7MH5102-2AD00 made by *Siemens*, and (b) technical drawing, quotes in mm (inches).

Each load cell has been combined with a 3D printed $\phi 41\,\text{mm}$ base and a 3D printed $\phi 40\,\text{mm}$ AB substitute to lean the module on with the ball mounting screws. Moreover, a $172.50 \times 281.15\,\text{mm}$ polycarbonate base with a thickness of $5\,\text{mm}$ has been designed to support the three load cells in a configuration equivalent to

Figure 4.2, thus the AB substitutes have been positioned on the vertices of an analogue equilateral triangle. To avoid unwanted deformations which would have tampered with the measurements, the base has been stiffened by three additional $20 \times 20\,\text{mm}$ strut profiles (analogue to the module structural frame) which have been fixed under the platform and close to the mounted load cells. Lastly, each load has been fixed with two $25\,\text{mm}$ spacers to free up enough space above the base to allow their deformation.

Figure 4.4 presents the CAD model of a single load cell with the mounted 3D printed components and an exploded view.

3D printed AB substitute

3D printed base

(a)   (b)
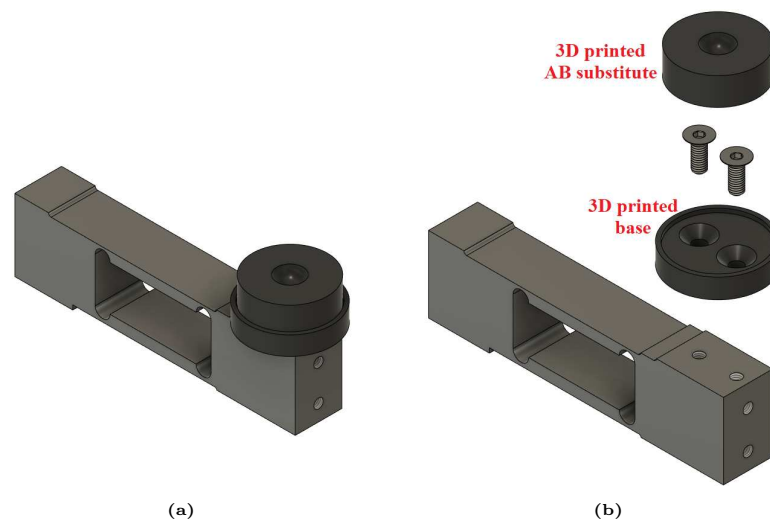
Figure 4.4: (a) CAD model of a load cell with 3D printed components and (b) exploded view.

Figure 4.5 illustrates the CAD model of the overall assembly and an exploded view.

(a)

25 mm spacers

Polycarbonate base

Strut profiles

(b)
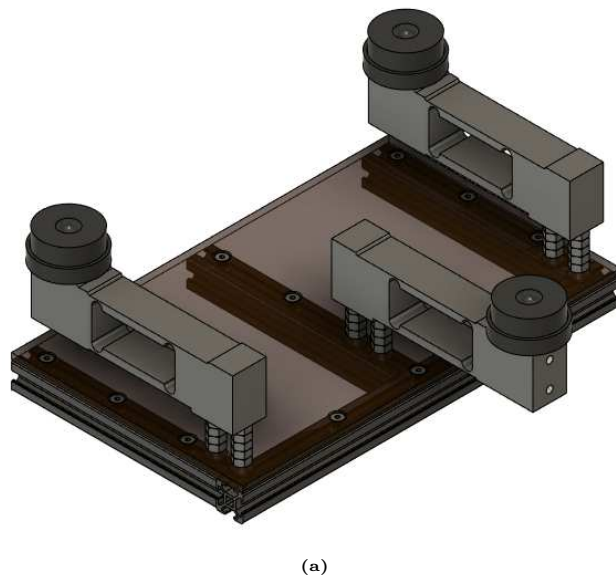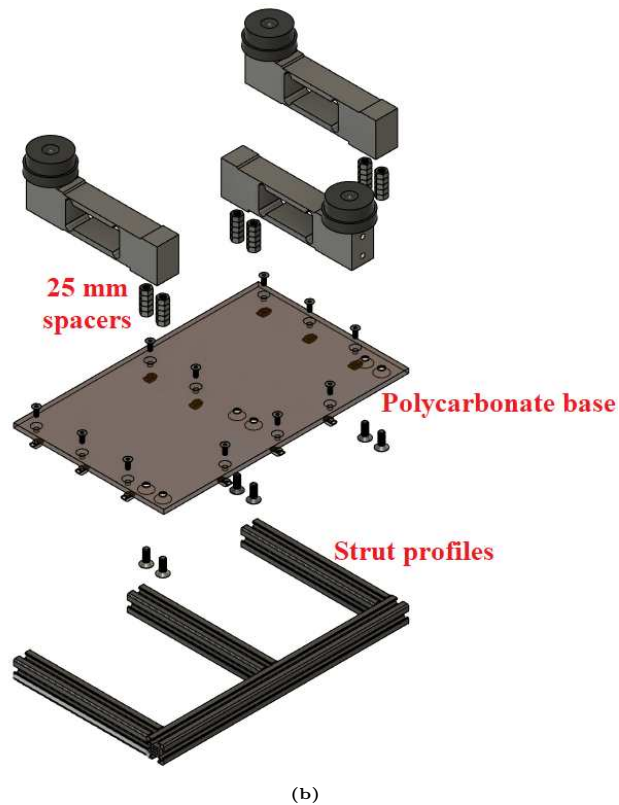
Figure 4.5: (a) CAD model of the load cells assembly and (b) exploded view.

To further stabilize the assembly, for the calibration and all obtained measurements, the load cells platform has been anchored on a table. Figure 4.6 shows the assembled module on the anchored load cells platform.

Figure 4.6: Assembled module on the anchored load cells platform.

4.1.2   Setup of the electronic circuit

The Siemens load cells are provided with a 6-wire configuration, whose diagram is shown in Figure 4.7.
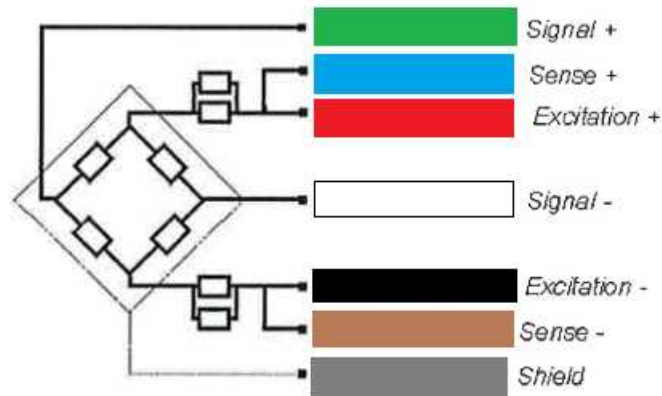
Figure 4.7: 6-wire load cell wiring diagram.

The 6 wires are the following:

- The excitation + and - wires (red and black) are dedicated to the power supply;

- The signal + and - wires (green and white) provide the analog output signal of a measurement;

- The sense + and - wires compensate possible voltage drops between the power supply and the load cel through an indicator on the excitation wires [9].

The three load cells have been connected to four additional components:

- Three HX711 24-bit Analog to Digital Converter (ADC) and amplifier electronic boards for each of the three load cells;

- An Arduino electronic board to read the digital outputs;

The HX711 ADC is an electronic board meant for a 4-wire load cell (Figure 4.8). The board is provided with 6 input pins and 4 output pins:

- Input pins:

    - 2 input pins E+ and E- for the excitation wires of the load cell;

- 2 input pins A+ and A- for the signal wires of the load cell with a gain factor of 128;

- 2 input pins B+ and B- for the signal wires of the load cell with a gain factor of 32;

- Output pins:

    - Output pin GND, ground for the power supply;

    - Output pin VCC, positive for power supply;

    - Output pins DT (short for DOUT) and SCK for digital data retrieval.
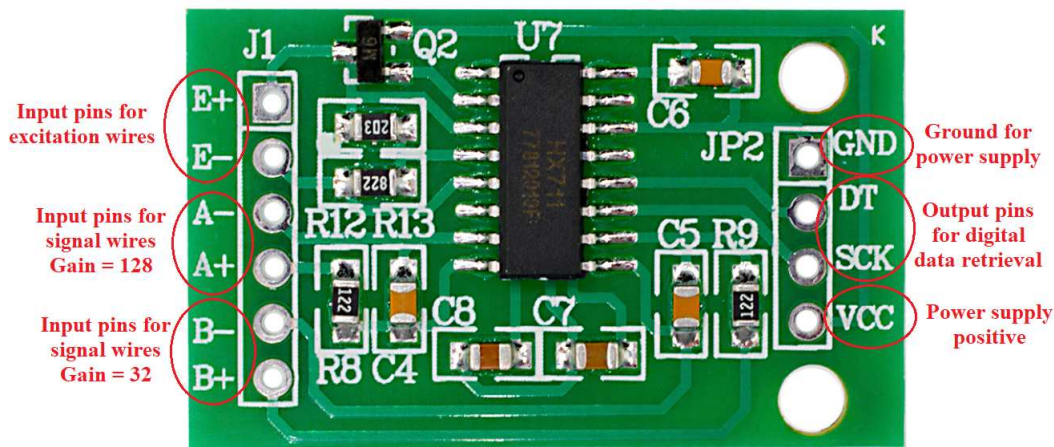
Figure 4.8: HX711 ADC board and description of input and output pins.

To connect the 6-wire load cells, the sense wires (blue and brown) have been coupled with the excitation wires (red and black) on the input pins E+ and E-. Since the rated output of the load cells is $2.0 \pm 0.2 \, \text{mV V}^{-1}$, the channel A with a gain factor of 128 has been chosen to connect the signal wires (green and white). The DT and SCK output pins have been connected to the digital I/O pins of the Arduino board to read the measured outputs (pins 2 and 3 for load cell #1, pins 4 and 5 for load cell #2 and pins 6 and 7 for load cell #3, Figure 4.9).

Lastly, the GND and VCC output pins of the ADC boards have been connected to an external power supply at 5 V and the Arduino has been connected to and powered by a PC through the USB port to display the several measurements. Therefore, the ADC boards and the linked load cells are separately powered from the Arduino to ensure the supply voltage of 5 V recommended by *Siemens*.

Figure 4.9 illustrates an Arduino board with a detail on the connected digital I/O outputs and Figure 4.10 presents a schematic overview of the electronic circuit.
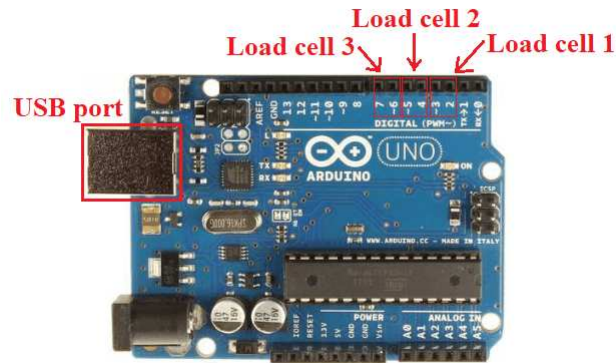
Figure 4.9: Arduino board and description of connected digital I/O pins.
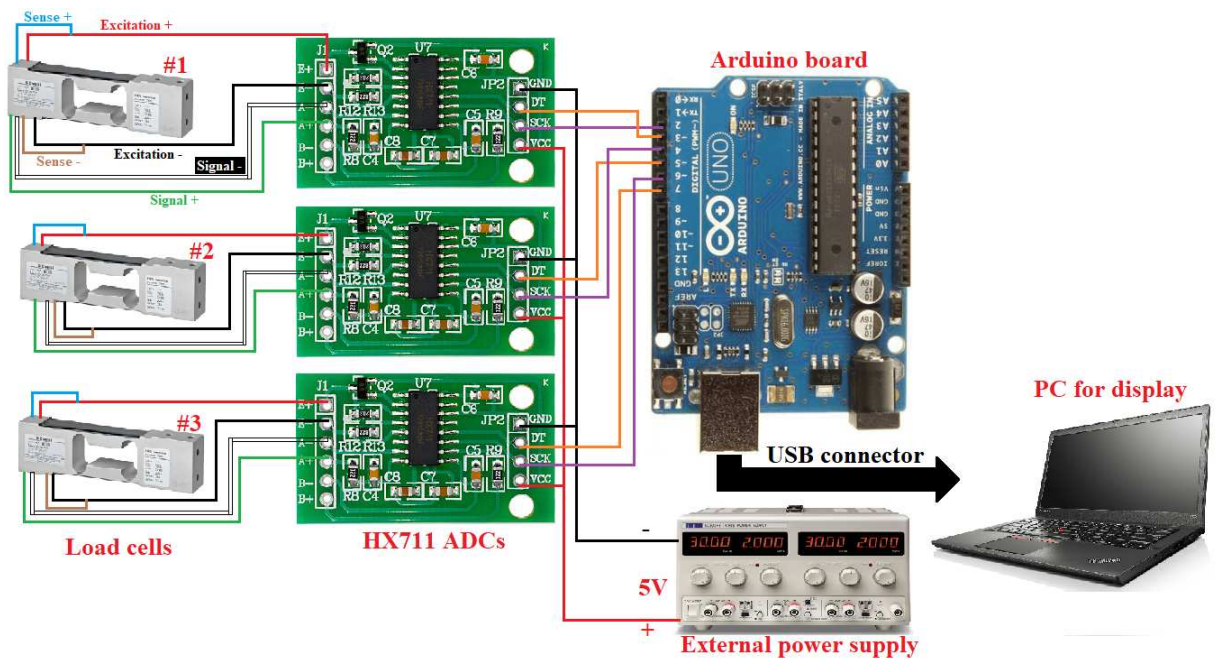
Figure 4.10: Schematic overview of the electronic circuit.

4.1.2.1 HX711 ADC board output readout and conversion

The HX711 board is 24-bit ADC converter with a gain factor G_f of 128. Therefore, it amplifies and converts the differential voltage signal of a load cell into an integer digital output O_d in the range $[O_d^{min}, O_d^{max}]$, where:

$$
\begin{cases}
n = 24 \\
O_d^{min} = -2^{n-1} = 8388608 \qquad \text{To account for negative readouts} \\
O_d^{max} = 2^{n-1} - 1 = 8388607
\end{cases}
$$

O_d^{max} corresponds to the maximum measured differential voltage of O_v^{max}, which depends on G_f and the supply voltage V_p (5 V for the three described load cells):

$$O_v^{max} = 0.5 \frac{V_p}{G_f} = 19.53 \, \text{mV}$$

Consequently, the generic amplified digital output O_d^g (which is read by the Arduino in the electronic circuit of Figure 4.10) can be converted into a differential voltage output O_v^g (in mV):

$$O_v^g = \frac{O_v^{max}}{O_d^{max}} O_d^g \tag{4.2}$$

This conversion has been useful to understand the obtained measurements for the 1° test.

4.1.3   Calibration of the three load cells

Before performing any measurement, the three load cells have been calibrated with a set of known weights by applying the linear least square method to obtain the calibration factors.

By using the library and custom functions provided by the HX711 ACD board, an Arduino script has been created to carry out the calibration procedure. After manually setting the proper digitial I/O pins to choose the output of one of the three load cells, this script has operated with the following steps:

1. Delay for a time of 5 s to prepare for the tare;

2. Apply the tare with a dedicated function from the HX711 library to remove any offset/bias of the unloaded load cell;

3. Delay for a time of 20 s to prepare for the acquisition and place a known weight;

4. Measure 100 output amplified digital values;

5. Compute and display the arithmetic average of the 100 obtained values on the serial monitor.

Seven known masses m_{C_i} have been considered for the calibration. Their masses values are shown in Table A.1.

m_{C_i}	Mass value [kg]
m_{C_1}	0.100
m_{C_2}	0.500
m_{C_3}	1.332
m_{C_4}	2.034
m_{C_5}	3.055
m_{C_6}	4.011
m_{C_7}	5.010

Table 4.1: Known masses for load cells calibration

These masses have spanned from $0.100\,\mathrm{kg}$ to approximately $5\,\mathrm{kg}$ to improve the least square method around the origin and to cover the expected load of the module of approximately $\frac{12}{3} = 4\,\mathrm{kg}$ with a margin of $1\,\mathrm{kg}$.

Therefore, the calibration procedure* has been performed with the following steps:

1. Manually set the digital I/O pins on the Arduino script to select one of the load cells;

2. Wait $5\,\mathrm{s}$ with the unloaded selected load cell for the tare to be completed;

3. Place a known weight m_{C_i} in the following $20\,\mathrm{s}$ on the selected load cell;

4. Read and take note of the obtained average output on the serial monitor;

5. Remove the known weight and reset the Arduino to reupload the script;

6. Repeat steps #3 to #7 for $i = 1, \ldots, 7$;

7. Repeat steps #2 to #8 for every load cell.

The obtained digital outputs have been converted to differential voltage outputs with Eq. 4.2.

A qualitative calibration curve of a load cell between the mV output and load is presented in Figure 4.11.

---

*The 3 load cells have been calibrated with the two mounted 3D printed components of Figure 4.4, because they have not been included in the estimation of the CoM position.
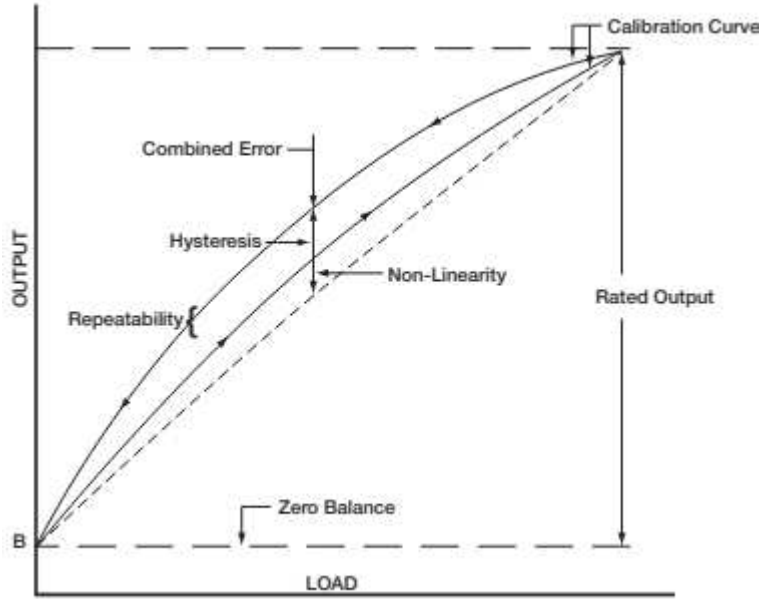
Figure 4.11: Generic calibration curve of a load cell, reprinted from [9].

While non-linearity and hysteresis are phenomena which affect the theoretical linear behaviour of a load cell, a linearization of the actual response can be performed with an acceptable approximation to achieve a calibration in the shortest time and at a low computational cost [10]. Therefore, a standard linear least square method [11] has been chosen to compute the calibration factors F_{C_j} (for $j = 1, \ldots, 3$) of the three load cells (expressed in $\mathrm{mV\,kg^{-1}}$) from the differential voltage outputs (7 per load cell).

A Matlab algorithm has been created to take the known masses and the voltage values as inputs and compute the linear calibration factors as outputs with the function *polyfit.m* (with polynomial degree set to 1 for least square linearization). Moreover, the function *polyval.m* has been used to compute the standard errors $\Delta_{C_j}^i$ of the linearization on the known masses for every load cell. Specifically, $\Delta_{C_j}^i$ is an estimation of the standard error of the least square linearization of the j-th load cell in predicting a future observation at the known mass value m_{C_i}.

Thus, with a known F_{C_j}, it is possible to convert a generic voltage output of the j-th load cell O_v^g into a correspoding mass value m^g (in kg), as follows:

$$m^g = \frac{O_v^g}{F_{C_j}} \quad \text{Linearized input/output relationship of a load cell} \qquad (4.3)$$

The results and calibration factors are presented in Subsection 5.1.1 of Ch. 5.

4.1.4 Alternatives for the movable and fixed masses

Unfortunately, the designed movable and fixed steel masses of Section 3.5 (Ch. 3) have not been manufactured in time for the performed tests and the overall thesis work. Therefore, a set of alternatives with equivalent masses and dimensions has been developed to be mounted on the structural frame and to carry out the declared tests.

The alternatives have involved the realization of four 3D printed cases to be filled with nuts, screws and several metallic parts to reach the designed mass values:

- Two identical $76 \times 26 \times 90 \, \mathrm{mm}^3$ cases to replace the two movable masses for the control of the X coordinate of the CoM in an equivalent configuration of Figure 3.32; once filled as efficiently as possible, the two cases have shared a mass of $0.672 \, \mathrm{kg}$ (which is acceptably lower than the designed mass of $0.687 \, \mathrm{kg}$); Figure 4.12 presents the CAD model of the 3D printed X case and the two filled cases;

- A $48 \times 70 \times 23 \, \mathrm{mm}^3$ case to replace the movable mass for the control of the Y coordinate in an equivalent configuration of Figure 3.32a; once filled, the case has amounted to a mass of $0.240 \, \mathrm{kg}$ (equal to the designed one); Figure 4.13 presents the CAD model of the 3D printed Y case and the filled case.

- A $56 \times 140 \times 55 \, \mathrm{mm}^3$ case to replace the fixed masses (total mass of $0.620 \, \mathrm{kg}$) and to simulate a payload with a mass of $1 \, \mathrm{kg}$; once filled and coupled with some aluminum mounting brackets, the assembly has amounted to a mass of $1 + 0.620 = 1.620 \, \mathrm{kg}$; Figure 4.14 presents the CAD model of the 3D printed payload case and the filled case with the aluminum brackets.

(a)   (b)
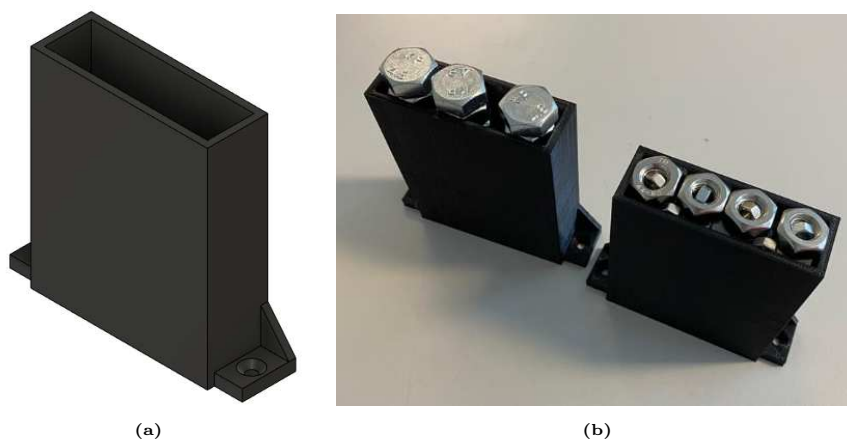
Figure 4.12: (a) CAD model of the 3D printed X case and (b) the two filled cases.

<div align="center">(a)   (b)</div>
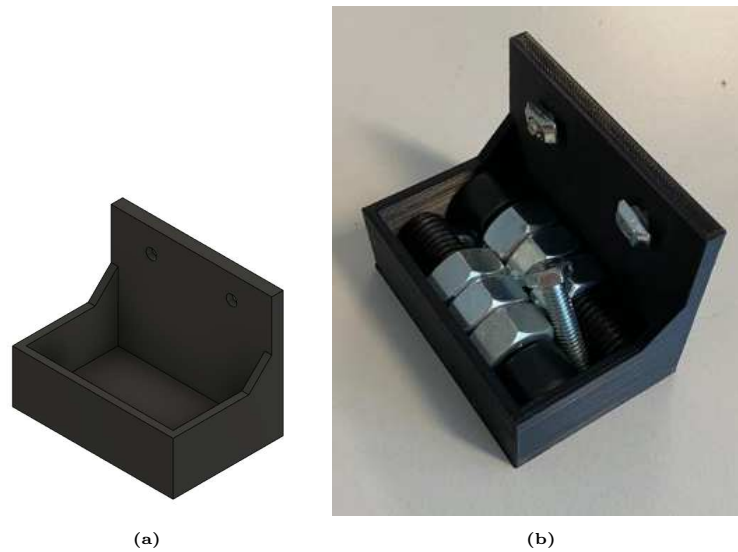
Figure 4.13: (a) CAD model of the 3D printed Y case and (b) filled case.

<div align="center">(a)   (b)</div>
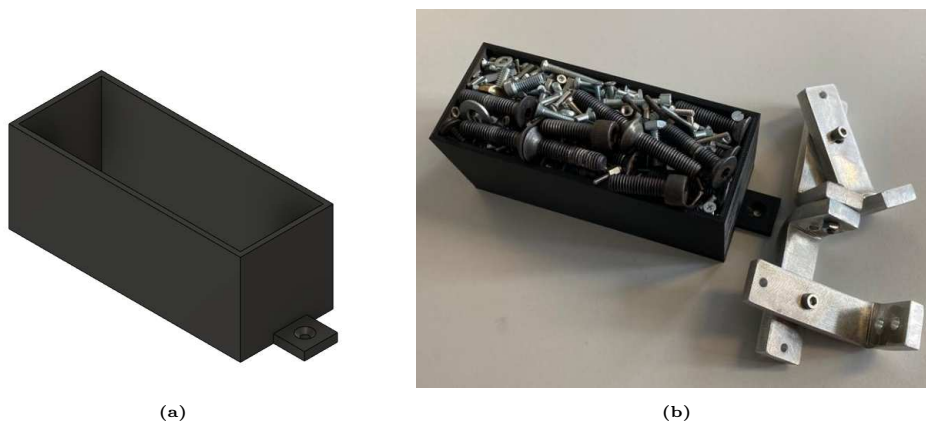
Figure 4.14: (a) CAD model of the 3D printed payload case and (b) filled case with additional aluminum brackets.

4.1.5 Measurement of the CoM position

The Arduino script for the load cells calibration has been expanded to perform the measurements with the load cells platform. The new script has simultaneously read the three output digital signals of the ADC boards and has extended the second delay duration of 20 s to 30 s to grant more time to manually place the module on the platform.

Two measurements have been performed with the goal of understanding the precision of the load cells platform and validating the CAD estimations:

1. Measurement of the CoM position and mass of the assembled module WITH-OUT the payload and movable alternative cases of the previous Subsection

(Figure 3.2b);

2. Measurement of the CoM position and mass of the assembled module with the mounted payload case and aluminum brackets; these additional components have been mounted on the front structural frame of the assembled module (Figure 4.15).
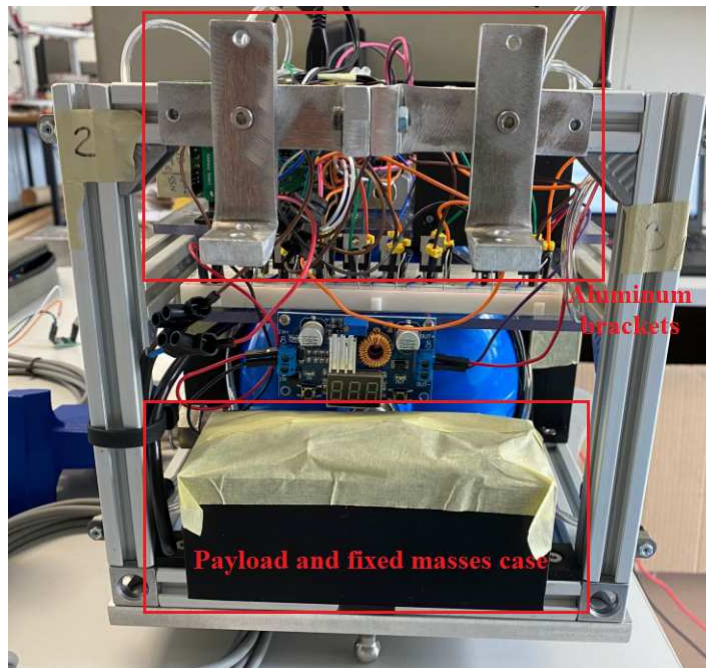
Figure 4.15: Mounted payload and fixed masses case and additional aluminum brackets.

The procedure for a single measurement has been the following:

1. Wait 5 s with the unloaded load cells platform for the tare to be completed;

2. Place the assembled module on the platform in the following 30 s;

3. Read and take note of the three output digital signals on the serial monitor;

4. Remove the module and reset the Arduino to reupload the script;

5. Repeat steps #2 to #6 ten times.

The three digital outputs have been converted to differential voltage outputs with Eq. 4.2.

Ten sets of outputs have been obtained to have an estimation of the uncertainty of the two measurements. For each set of three voltage outputs, the CoM position and the total mass have been computed with the obtained calibration factors and

the geometrical positions of the ABs from the CAD model (Equations 4.1 and 4.3). Therefore, an overall mean of the ten values and corresponding standard deviations have been obtained. The results are presented in Subsection 5.1.2 of Ch. 5.

4.1.6 Control and alignment of the CoM position

The first test on the vehicle has been concluded with the control and alignment of the CoM position around the GC within an error of 1 mm. The movable masses alternatives (Figures 4.12b and 4.13b) have been positioned according to the results of the second measurement of the previous Subsection, which has included the mass of a generic payload and the fixed masses.

The X movable masses have been positioned in configurations which are shown in Figure 4.16a (X movable mass which has acted as a counterweight) and Figure 4.17a (X movable mass whose position has been actually shifted). The second measurement of the CoM position of Subsection 4.1.5 has proved its X coordinate to approximately be 6 mm (see Ch. 5 for the results), therefore the X movable counterweight has been positioned at the maximum fixed distance L_{c_x} of 196 mm from the front strut profile (Figure 4.16b) to maximize the CoM shift along the X axis. Due to the second measurement estimating the Y coordinate at approximately -3 mm, the Y movable mass has been mounted and kept fixed on the extreme position of its guide (Figure 4.18) to maximize the CoM shift along the Y axis. The distance L_{m_x} of the X movable mass from the front strut profile (Figure 4.17a) has been manually shifted with increments of 1 mm to achieve the CoM alignment along the X axis.

The test procedure, which has involved the same Arduino script of the two previous measurements, has had the following steps:

1. Position the X movable mass at a distance L_{m_x};

2. Wait 5 s with the unloaded load cells platform for the tare to be completed;

3. Place the assembled module on the platform in the following 30 s;

4. Read and take note of the three output digital signals on the serial monitor;

5. Remove the module and compute the X coordinate of the CoM;

6. Repeat steps #2 to #7 until the X coordinate is acceptably close to the origin;

7. Take nine additional measurements of the load cells with the proper L_{m_x} distance by applying the same procedure of Subsection 4.1.5.

Once again, ten sets of three digital outputs have been obtained. The estimation of the mean values of the CoM position and mass and the corresponding standard deviations have been performed in a manner equivalent to Subsection 4.1.5. The results are presented in Subsection 5.1.3 of Ch. 5.
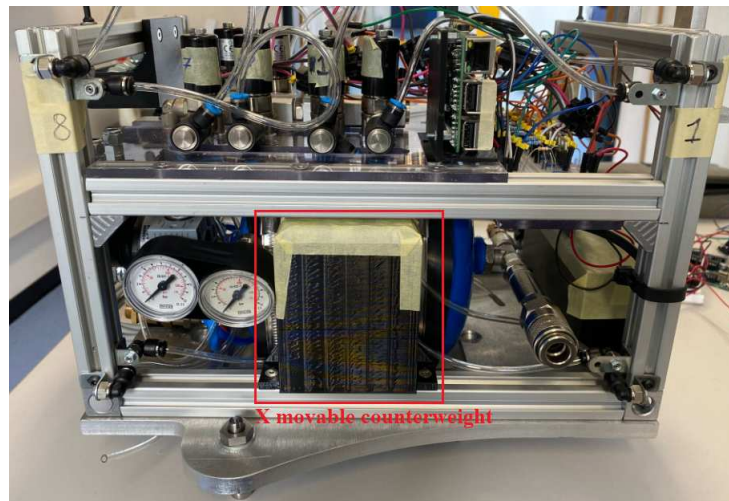
(a)
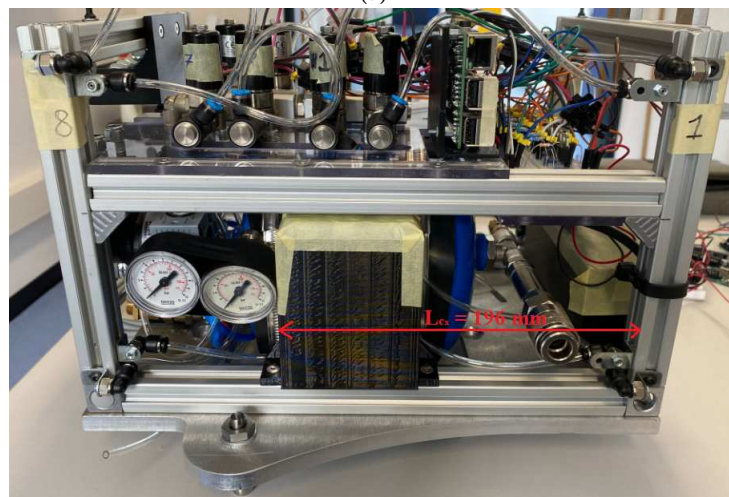
(b)

Figure 4.16: (a) X movable counterweight and (b) detail of the measured distance L_{c_x}.
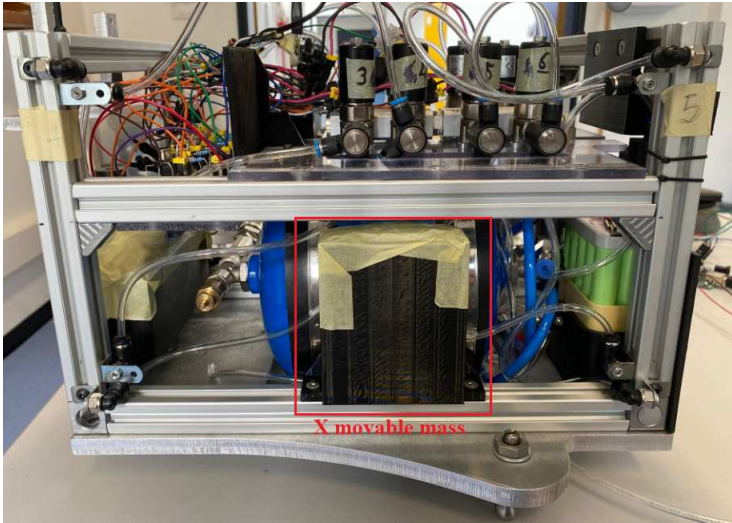
(a)
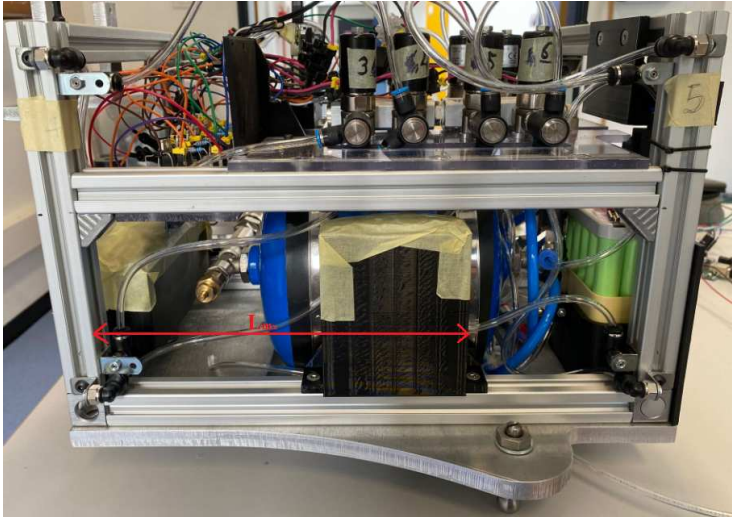
(b)

Figure 4.17: (a) X movable mass and (b) detail of the measured distance L_{m_x}.
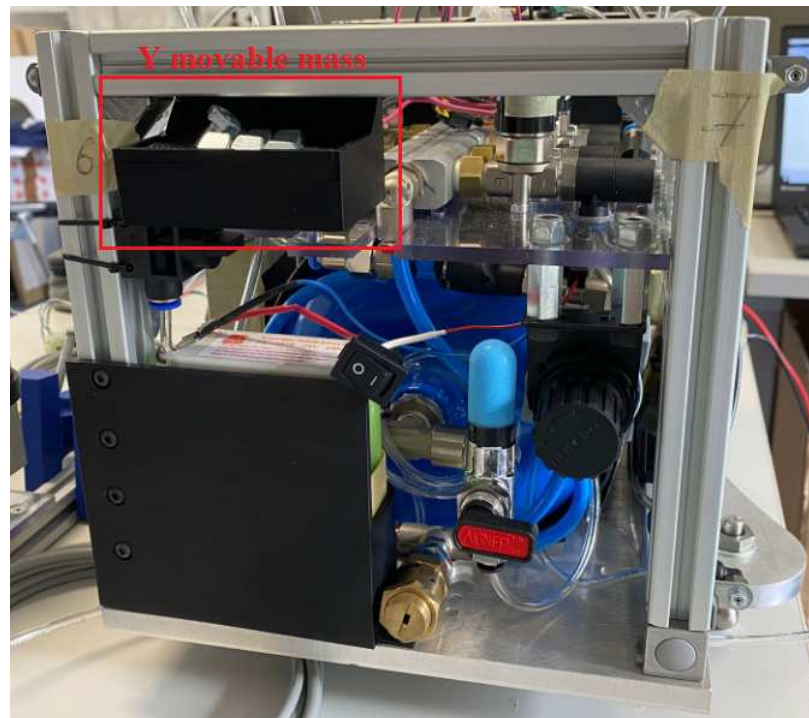
Figure 4.18: Y movable mass on its extreme position.

4.2   Estimation of the inertia around the main rotational axis

The second sequence of tests to estimate the inertia of the module around its main rotational axis has been performed after the achievement of the CoM alignment (first test, see previous Section). By executing multiple pure rotations on the levelled table with the actuated propulsion system, the module motion has been tracked with a motion capture system. From the resulting angular acceleration around the Z axis and the torque applied by the thrusters, the inertia has been estimated. Therefore, the second test has involved the following steps:

1. Setup of the motion capture system;

2. Execution of pure rotations with the propulsion system;

3. Estimation of the inertia inertia from the tracked motion.

The results of steps #2 and #3 are presented in Ch. 5.

4.2.1 Setup of the motion capture system

In order to track the module movement, a motion capture system of four IR cameras at the four corners of the levelled table has been employed. The motion capture cameras, model Prime^x 13 made by *OptiTrack*, are able to reconstruct the trajectory of an object with an accuracy of $\pm 0.2\,$mm. Figure 4.19 presents the motion capture camera and the overall test setup for the inertia estimation.

(a)

(b)

Figure 4.19: (a) Motion capture camera, model Prime^x 13 made by *OptiTrack*, and (b) test setup for the inertia estimation of the module.

Once properly calibrated and with a framerate of 240FPS, the motion capture system returns the 3D position (in mm) and rotation (in deg) of an object in a predetermined reference frame. This reference frame is set by the four cameras with a calibration square (model CS-200 by *OptiTrack*), which defines the origin

and the X and Y axes. Consequently, the calibration square has been positioned at one corner of the levelled table, so that the corresponding XY position of the module would have positive values for simplicity. Figure 4.20 shows the calibration square and the resulting predetermined reference frame on the levelled table.

(a)

(b)
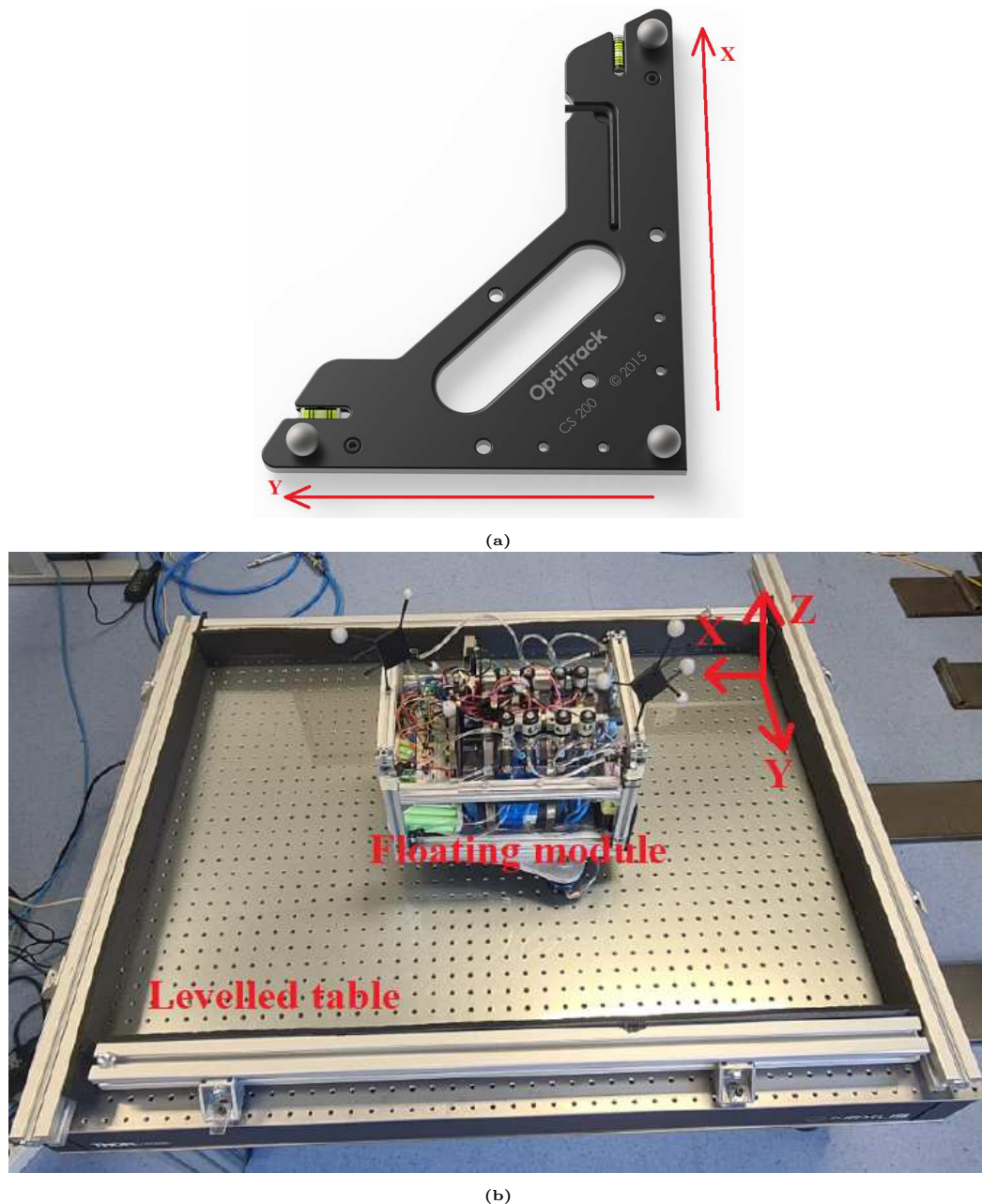
Figure 4.20: (a) Calibration square, model CS-200 made by *OptiTrack*, and (b) predetermined reference frame on the levelled table.

Furthermore, the motion capture system tracks the position of an object with a group of mounted spherical markers, which are coated with a reflective tape detected by the four IR cameras. The markers are identified as geometrical points

in the predetermined reference frame and their overall barycenter is automatically computed. Therefore, the markers geometrical configuration is represented as a rigid body whose movement is tracked by the multi-view system. For the floating module, two sets of three and four markers respectively have been mounted on the corners of the aluminum structural frame in an asymmetrical configuration, so that:

  - The markers barycenter would have been coincident with the module CoM (therefore, the tracked motion has been the actual motion of the vehicle to estimate the inertia);

  - The rotation around the Z axis (Figure 4.20b) would have been properly detected even with rotations greater than 180 deg (thanks to the asymmetrical configuration).

Figure 4.21 illustrates the base for the set of four markers and the markers mounted on the module structural frame.

(a)   (b)
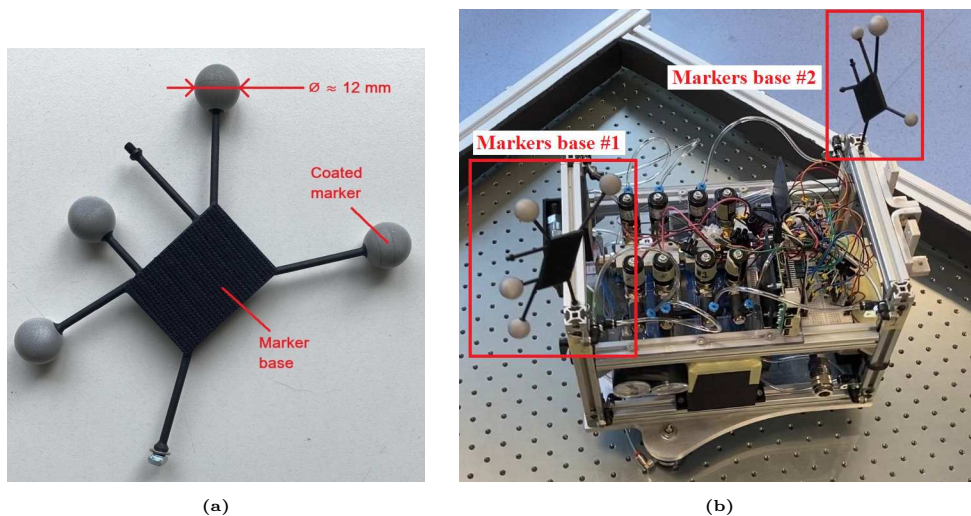
Figure 4.21: (a) Base for the four markers and (b) markers mounted on the vehicle.

Lastly, the calibration procedure and the data acquisition have been performed with the *Motive:Tracker* software provided by *OptiTrack*. Figure 4.22 presents the software interface, which shows the simultaneous view of the four IR cameras, the predetermined reference system and the rigid body defined by the markers.
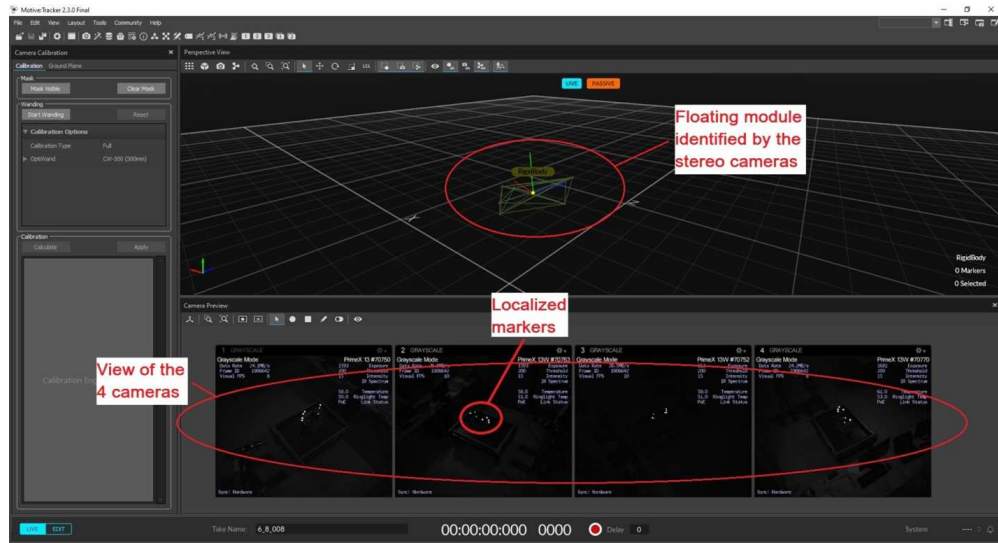
Figure 4.22: *Motive:Tracker* software interface.

4.2.2 Execution of pure rotations on the levelled table

By actuating the propulsion system, a sequence of pure rotations around the Z axis has been performed on the levelled table to evaluate the inertia of the system. Specifically, twelve pure rotations have been performed to estimate the associated error. The nozzles along the Y axis of Figure 3.2a (Ch. 3) have been separarely activated to generate the necessary torques and angular accelerations to initiate and terminate a counterclockwise rotation around the Z axis. Figure 4.23 illustrates a schematic view of the produced torques and rotation.
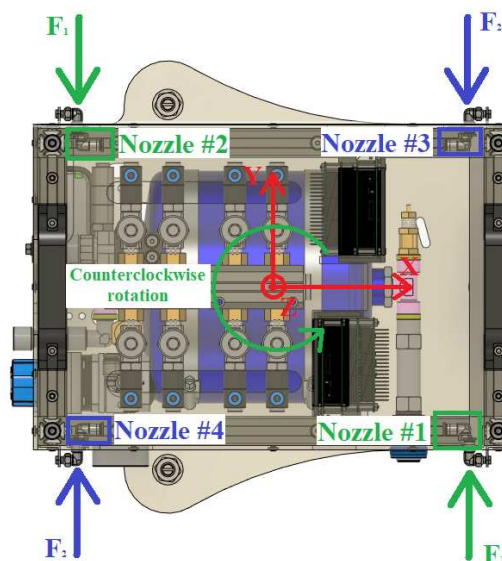
Figure 4.23: Schematic view of the produced torques and counterclockwise rotation around the Z axis, nozzles #1 and #2 for acceleration and nozzles #3 and #4 for deceleration.

The nozzles along the Y axis have been chosen due to their greater geometrical arm with respect to the opposite ones along the X axis. Furthermore, to generate a counterclockwise rotation, the control sequence for nozzles #1, #2, #3 and #4 has been divided into three phases:

1. Acceleration phase: wait for 1 s and activate nozzles #1 and #2 by fully opening the corresponding EVs for a total time of 1 s;

2. Steady state phase: deactivate nozzles #1 and #2 and leave the floating module in a resulting free rotation for 2 s;

3. Deceleration phase: activate nozzles #3 and #4 by fully opening the corresponding EVs for a total time of 1 s to stop the rotation.

From the external PC of Figure 4.19b, the control sequence has been generated by a Simulink model and directly uploaded via Wi-Fi to the mounted Raspberry Pi 3B. The electronic board has consequently controlled the four EVs during the three phases for every performed rotation. Figure 4.24 illustrates the plot of the commanded control sequence over time, with logical 0 representing an EV closed and logical 1 representing the same EV fully opened.
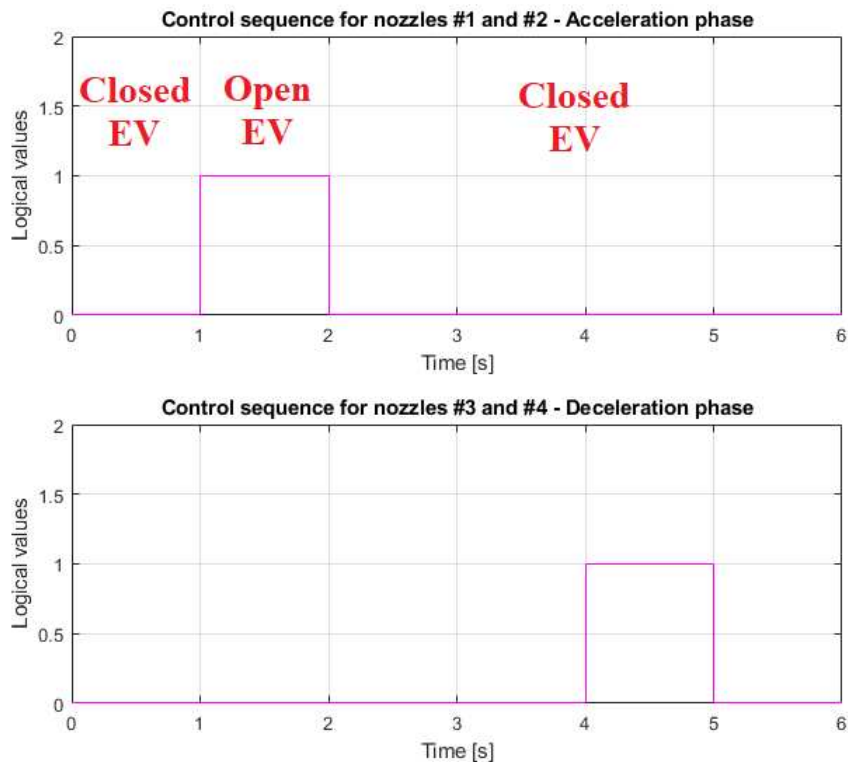
Figure 4.24: Plot of the commanded control sequence for the nozzles activation.

After placing the module on the levelled table, the procedure for the second serie of tests has been the following:

1. Open the valve for the floating system;

2. Manually stabilize the floating module to ensure a fixed initial position;

3. Start the acquisition of the motion capture system;

4. Upload the control sequence to the Raspberry PI 3B board;

5. Wait for a time greater than 4 s for the control sequence and rotation around the Z axis to be completed;

6. Stop the acquisition and save the tracked motion;

7. Close the valve for the ABs;

8. Repeat steps #1 to #7 twelve times.

Moreover, the motion capture system has returned twelve acquisitions in the form of .csv files. Each file has contained a table with the registered frames (with a framerate of 240FPS), the time values, the rotation values (in deg) and position values (in mm) of the X, Y and Z axes. The .csv tables have been converted to matrices by a Matlab script. Consequently, the rotation values around the Z axis have been extracted to compute the mean and standard deviation of the resulting twelve inertia values. Section 5.2 of Ch. 5 presents the performed computations and obtained results for the inertia estimation.

Chapter 5

Results and analysis of the performed tests

This chapter presents the results and corresponding analysis of the two main performed tests:

1. Measurement, control and alignment of the CoM of the module (Test #1);

2. Estimation of the inertia around the main rotational axis (Test #2).

5.1   Results and analysis of Test #1

This section presents and analyzes the results of steps #3, #5, #6, #7 of Section 4.1 (see Ch. 4 for Test #1 procedure).

5.1.1   Results and analysis of the load cells calibration

By following the calibration procedure of Section 4.1.3, seven average differential voltage outputs per load cell have been obtained. Table 5.1 illustrates these results.

Mass m_{c_i} [kg]	Differential voltage outputs [mV]		
	Load cell #1	Load cell #2	Load cell #3
0.100	0.10	0.10	0.10
0.500	0.49	0.50	0.50
1.332	1.31	1.32	1.33

2.034	2.01	2.02	2.03
3.055	3.02	3.04	3.05
4.011	3.96	3.99	4.00
5.010	4.95	4.99	4.99

Table 5.1: Obtained differential voltage values for calibration

By taking the known masses m_{C_i} and the voltage values as inputs, the Matlab algorithm has computed the three calibration factors F_{C_j} and the standard errors $\Delta^j_{C_i}$ with the least square linearization.

The calibration factors F_{C_j} of the three load cells are:

$$F_{C_1} = 0.988 \, \text{mV} \, \text{kg}^{-1}$$
$$F_{C_2} = 0.996 \, \text{mV} \, \text{kg}^{-1}$$
$$F_{C_3} = 0.997 \, \text{mV} \, \text{kg}^{-1}$$

The three values are remarkably equivalent, thus validating the performances of the load cells which have been operating under similar conditions on the platform. Additionally, the standard errors $\Delta^1_{C_i}$ and $\Delta^2_{C_i}$ of load cells #1 and #2 and $\Delta^3_{C_i}$ of load cell #3 have been observed to be of the orders of $10^{-3} \, \text{mV}$ and $10^{-4} \, \text{mV}$ respectively. Therefore, the least square linearization has proven to be optimal to approximate the input/output relationship of the three load cells.

Figures 5.1, 5.2 and 5.3 show the linearized load-to-output relationships and the corresponding prediction intervals of $\pm 2\Delta$ (confidence level of 95%) of the load cells #1, #2 and #3 respectively.
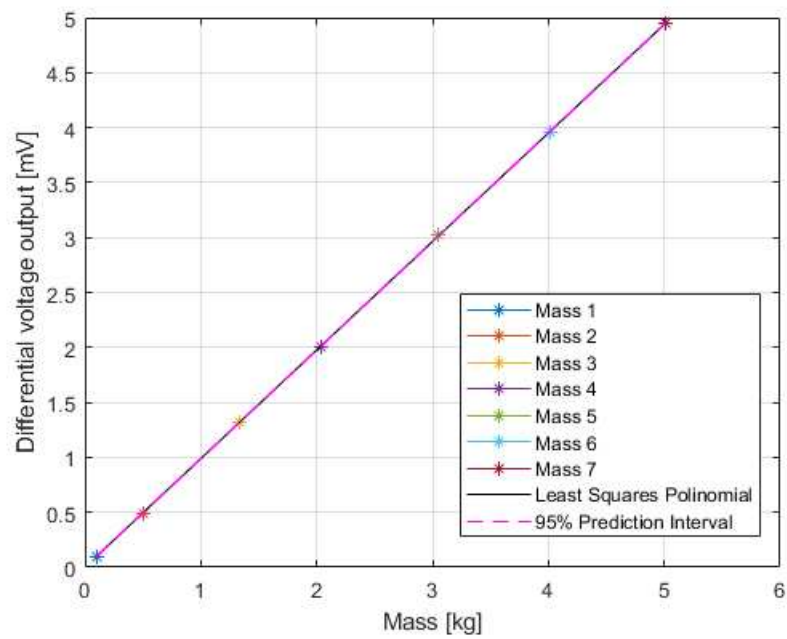
Figure 5.1: Calibration curve of a load cell #1 and 95% prediction interval.
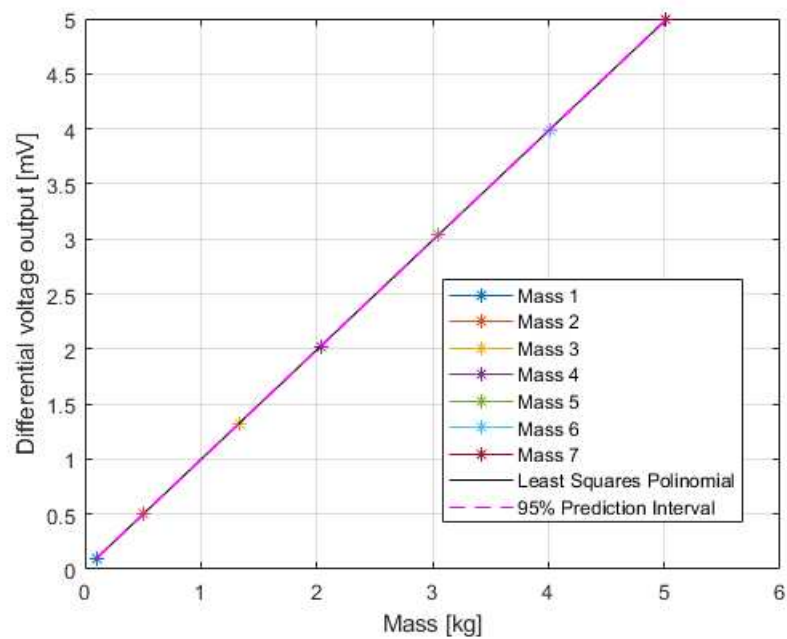
Figure 5.2: Calibration curve of a load cell #2 and 95% prediction interval.
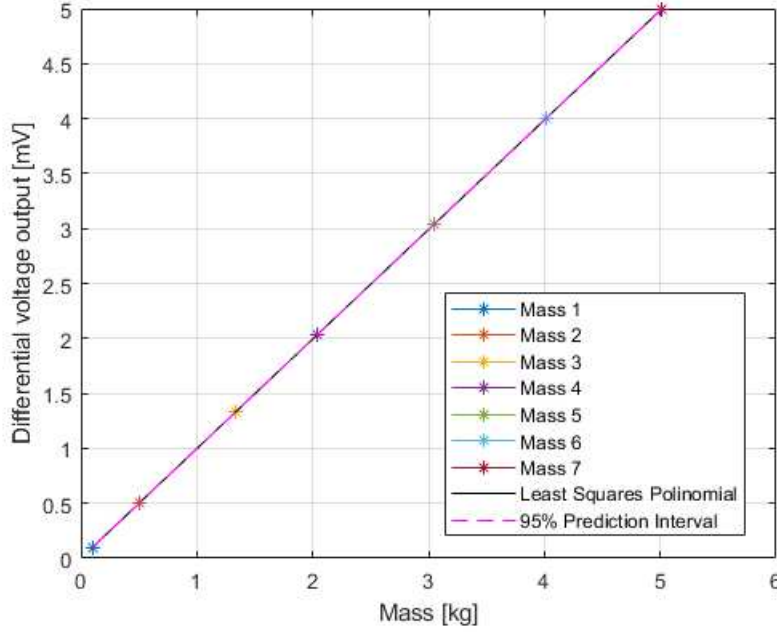
Figure 5.3: Calibration curve of a load cell #3 and 95% prediction interval.

By zooming on each measured point, it has been verified that all of them are contained in the prediction intervals of $\pm 2\Delta$.

5.1.2 Results and analysis of the two measurements of the CoM position

By following the procedure of Subsection 4.1.5, ten sets of three output differential voltages have been obtained for each of the two performed measurements. The geometrical positions in the XY plane of the ABs from the CAD model $\vec{r}_{AB_1}$, $\vec{r}_{AB_2}$ and $\vec{r}_{AB_3}$ are:

$$\vec{r}_{AB_1} = \begin{pmatrix} 145 \\ 0 \end{pmatrix} \text{mm} \qquad \vec{r}_{AB_2} = \begin{pmatrix} -72.5 \\ -125.574 \end{pmatrix} \text{mm} \qquad \vec{r}_{AB_3} = \begin{pmatrix} -72.5 \\ 125.574 \end{pmatrix} \text{mm}$$

5.1.2.1 Results of the first measurement: assembled module without payload and movable and fixed masses

Ten sets of three output differential voltage values $O_{v_j}^i$ ($j = 1, \ldots, 3$ for number of load cells, $i = 1, \ldots, 10$ for number of repeated measurements) have been obtained for the first measurement (see Table A.1, Appendix A). The $O_{v_j}^i$ values

have been converted into mass values m_j^i with the calibration factors F_{C_j}:

$$m_j^i = \frac{O_{v_j}^i}{F_{C_j}} \tag{5.1}$$

From m_j^i and $\vec{r}_{AB_j}$, the i-th CoM position $\vec{r^i}_{FM}$ (on the XY plane) and mass m_{FM}^i of the module have been computed:

$$m_{FM}^i = m_1^i + m_2^i + m_3^i \tag{5.2a}$$

$$\vec{r^i}_{FM} = \begin{pmatrix} x_{FM}^i \\ y_{FM}^i \end{pmatrix} = \frac{1}{m_{FM}^i}(m_1^i \vec{r}_{AB_1} + m_2^i \vec{r}_{AB_2} + m_3^i \vec{r}_{AB_3}) \tag{5.2b}$$

Table 5.2 presents the obtained results with three significant figures for the X coordinate, two for the Y coordinate and three for the mass.

Set #	x_{FM}^i [mm]	y_{FM}^i [mm]	m_{FM}^i [kg]
1	-25.2	-3.7	8.48
2	-25.0	-2.5	8.49
3	-26.3	-3.8	8.43
4	-26.7	-3.7	8.46
5	-26.2	-2.6	8.42
6	-25.8	-3.0	8.44
7	-25.9	-2.5	8.44
8	-25.5	-2.4	8.48
9	-25.3	-3.8	8.52
10	-24.5	-2.6	8.50

Table 5.2: Results of the CoM position and mass

The mean values $\overline{m}_{FM}$ and $\vec{\overline{r}}_{FM}$ are:

$$\overline{m}_{FM} = \frac{1}{10}\sum_{i=1}^{10} m_{FM}^i = 8.47\,\text{kg}$$

$$\vec{\overline{r}}_{FM} = \frac{1}{10}\sum_{i=1}^{10} \vec{r^i}_{FM} = \begin{pmatrix} \overline{x}_{FM}^i \\ \overline{y}_{FM}^i \end{pmatrix} = \begin{pmatrix} -25.6 \\ -3.1 \end{pmatrix}\text{mm}$$

The corresponding standard deviations σ_m, σ_x, σ_y are:

$$\sigma_m = \sqrt{\frac{1}{10}\sum_{i=1}^{10}(m_{FM}^i - \overline{m}_{FM})^2} = 0.03\,\text{kg}$$

$$\sigma_x = \sqrt{\frac{1}{10}\sum_{i=1}^{10}(x_{FM}^i - \overline{x}_{FM})^2} = 0.7\,\text{mm} \qquad (0.21\%\text{ of the }330\,\text{mm dimension})$$

$$\sigma_y = \sqrt{\frac{1}{10}\sum_{i=1}^{10}(y_{FM}^i - \overline{y}_{FM})^2} = 0.6\,\text{mm} \qquad (0.27\%\text{ of the }224\,\text{mm dimension})$$

Therefore, the overall results are:

$$m_{FM} = 8.47 \pm 0.03\,\text{kg}$$

$$\vec{r}_{FM} = \begin{pmatrix} -25.6 \pm 0.7 \\ -3.1 \pm 0.6 \end{pmatrix}\text{mm}$$

The results have reduced errors and are remarkably similar to the CAD estimation of Eq. 3.1 (see Ch. 3), with only the mass greater by approximately 0.4 kg, because the assembled module has included additional electrical components, such a breadboard for the EVs circuit, and corresponding supports and electrical wiring, despite not including the ABs EV.

5.1.2.2   Results of the second measurement: assembled module with payload and fixed masses

Similarly to the first measurement, ten sets of output differential voltage values $O_{v_j}^i$ have been obtained for the second measurement (see Table A.2, Appendix A). These values have been converted in an equivalent manner with Eqs. 5.1 and 5.2. Table 5.3 presents the obtained results with two significant figures for the X and Y coordinates and five significant figures for the mass.

Set #	x_{FM}^i [mm]	y_{FM}^i [mm]	m_{FM}^i [kg]
1	5.8	−2.8	10.253
2	5.8	−1.9	10.253
3	5.8	−2.8	10.251
4	5.7	−2.4	10.258

5	5.8	−3.1	10.253
6	5.2	−2.8	10.258
7	5.6	−2.8	10.251
8	5.5	−2.6	10.248
9	5.1	−2.4	10.276
10	5.2	−3.4	10.263

Table 5.3: Results of the CoM position and mass

The mean values $\overline{m}_{FM}$ and $\overline{\vec{r}}_{FM}$ are:

$$\overline{m}_{FM} = 10.256 \, \text{kg}$$

$$\overline{\vec{r}}_{FM} = \begin{pmatrix} 5.6 \\ -2.7 \end{pmatrix} \text{mm}$$

The corresponding standard deviations σ_m, σ_x, σ_y are:

$$\sigma_m = 0.008 \, \text{kg}$$
$$\sigma_x = 0.3 \, \text{mm} \qquad\qquad (0.09\% \text{ of the } 330 \, \text{mm dimension})$$
$$\sigma_y = 0.4 \, \text{mm} \qquad\qquad (0.18\% \text{ of the } 224 \, \text{mm dimension})$$

Therefore, the overall results are:

$$m_{FM} = 10.256 \pm 0.008 \, \text{kg}$$

$$\vec{r}_{FM} = \begin{pmatrix} 5.6 \pm 0.3 \\ -2.7 \pm 0.4 \end{pmatrix} \text{mm}$$

The estimations have slightly improved with respect to the first measurement. The reason has been identified with all three load cells having similar and greater weights to support, therefore equalizing and reducing the structural deformation of the polycarbonate platform along the X and Y axes. Once again, the results are similar to the CAD estimation of Eq. 3.3 (see Ch. 3), with the mass greater by approximately $0.4 \, \text{kg}$ for the same reasons.

5.1.3   Results and analysis of the CoM control and alignment

By following the procedure of Subsection 4.1.6, the CoM position has been aligned around the GC within an error of $1\,\mathrm{mm}$.

The distance L_{m_x} of the X movable mass has been shifted three times until an acceptable alignment along the X axis has been achieved, while the Y movable mass has been kept fixed on its extreme position to maximize the CoM shift along the Y axis:

1. $L_{m_x} = 196\,\mathrm{mm}$, symmetrical position with respect to the X movable counterweight:

   $$\text{Obtained voltage outputs from load cells:}\quad \begin{pmatrix} 3.89 \\ 4.01 \\ 3.85 \end{pmatrix}\mathrm{mV} \implies x_{FM} = -0.7\,\mathrm{mm}$$

   x_{FM} is already in the $1\,\mathrm{mm}$ range, but a new L_{m_x} distance has been tested to account for uncertainties.

2. $L_{m_x} = 194\,\mathrm{mm}$:

   $$\text{Obtained voltage outputs from load cells:}\quad \begin{pmatrix} 3.92 \\ 3.96 \\ 3.88 \end{pmatrix}\mathrm{mV} \implies x_{FM} = 0.4\,\mathrm{mm}$$

   x_{FM} is greater than the first case and within the $1\,\mathrm{mm}$ range, therefore a new intermediate L_{m_x} distance of $195\,\mathrm{mm}$ has been tested.

3. $L_{m_x} = 195\,\mathrm{mm}$:

   $$\text{Obtained voltage outputs from load cells:}\quad \begin{pmatrix} 3.88 \\ 4.00 \\ 3.86 \end{pmatrix}\mathrm{mV} \implies x_{FM} = -0.2\,\mathrm{mm}$$

   x_{FM} is included in the range of the first two cases, therefore $L_{m_x} = 195\,\mathrm{mm}$ has been considered as the final distance.

To validate the identified alignment, nine more measurements have been acquired with the final distance $L_{m_x} = 195\,\mathrm{mm}$. Once again, the ten corresponding sets (see Table A.3, Appendix A) have been converted to CoM positions and system masses with Eqs. 5.1 and 5.2. Table 5.4 presents the obtained results, with one

significant figure for the X coordinate, two significant figures for the Y coordinate and four significant figures for the mass.

Set #	x_{FM}^i [mm]	y_{FM}^i [mm]	m_{FM}^i [kg]
1	-0.2	-1.6	11.828
2	-0.2	-1.9	11.811
3	-0.4	-2.3	11.839
4	0.8	-0.9	11.825
5	0.2	-1.1	11.829
6	0.0	-1.3	11.824
7	0.0	-1.6	11.821
8	-0.2	-2.9	11.839
9	-0.2	-1.5	11.828
10	0.4	-0.8	11.827

Table 5.4: Results of the CoM position and mass

The mean values $\overline{m}_{FM}$ and $\vec{\overline{r}}_{FM}$ are:

$$\overline{m}_{FM} = 11.827\,\text{kg}$$

$$\vec{\overline{r}}_{FM} = \begin{pmatrix} 0.0 \\ -1.6 \end{pmatrix} \text{mm}$$

The corresponding standard deviations σ_m, σ_x, σ_y are:

$$\sigma_m = 0.008\,\text{kg}$$
$$\sigma_x = 0.4\,\text{mm} \qquad\qquad (0.12\%\ \text{of the}\ 330\,\text{mm dimension})$$
$$\sigma_y = 0.6\,\text{mm} \qquad\qquad (0.27\%\ \text{of the}\ 224\,\text{mm dimension})$$

Therefore, the final results are:

$$m_{FM} = 11.827 \pm 0.008\,\text{kg}$$

$$\vec{r}_{FM} = \begin{pmatrix} 0.0 \pm 0.4 \\ -1.6 \pm 0.6 \end{pmatrix} \text{mm}$$

The alignment along X within an error of 1 mm (requirement #5 of the mechanical design, see Section 2.1, Ch. 2) has proven to be remarkably successfull around

the origin (actual error of $\pm 0.4\,\text{mm}$). On the contrary, the Y coordinate has been estimated to be approximately $1\,\text{mm}$ further from the GC. While representing an acceptable misalignment (0.27% of the $224\,\text{mm}$ dimension), the Y coordinate can be centered at the origin by shifting the symmetrical configuration of the designed fixed masses of Figure 3.28 (Ch. 3) into an asymmetrical one. Moreover, the mass is acceptably close to the goal of $12\,\text{kg}$.

5.2   Results and analysis of Test #2

This Section presents the results for the serie of tests for the inertia estimation of the module. By following the procedure of Subsection 4.2.2 of Ch. 4, twelve acquisitions of the tracked pure rotations in the form of .csv files have been obtained. A Matlab script has been created to extract the rotation values along the Z axis to be converted into the desired inertia values. For simplicity and clarity, all following Figures and plots refer to the data of rotation #3. Figure 5.4 shows the performed rotation around the Z axis over time for rotation #3, with an illustration of the three phases of the control sequence (acceleration phase, steady state phase and deceleration phase).
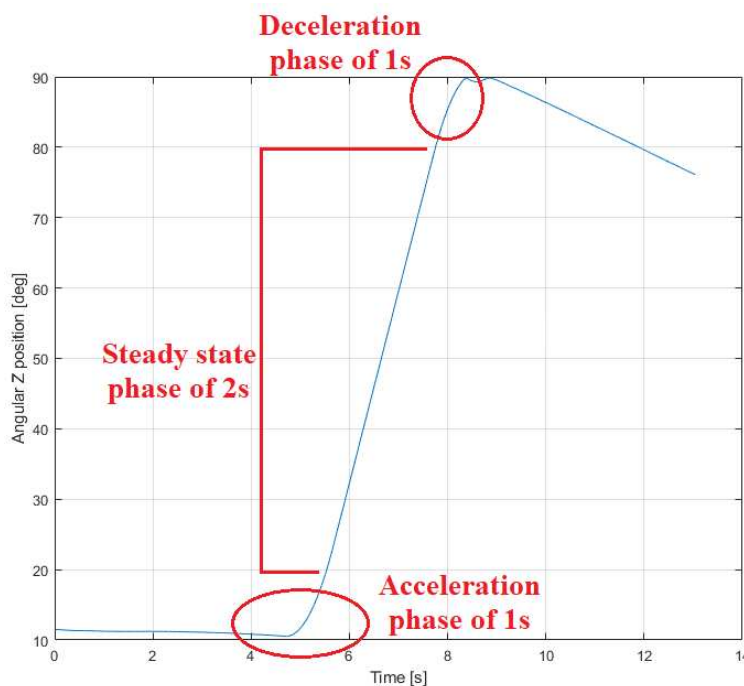
Figure 5.4: Angular rotation along the Z axis for rotation #3, with a detail of the three phases of the control sequence.

It has been verified that all the additional eleven rotations share an equivalent

qualitative shape and the three phases of the commanded control sequence (see Subsection 4.2.2) are clearly identified.

A Finite-Difference Method (FDM) has been applied to derive the generic rotation vector $\vec{\theta}^p$ with respect to the time vector $\vec{t}^p$ of the p-th test (for $p = 1, \ldots, 12$, number of elements equal to l) and obtain an angular velocity vector $\vec{\omega}^p$ (number of elements equal to m). Moreover, the obtained $\vec{\omega}^p$ has been converted to an angular acceleration vector $\vec{\alpha}^p$ (number of elements equal to n) in an similar manner. The following equations show the performed computations:

$$\theta_k^p(t_k)$$

$$\implies \omega_j^p(t_j') = \frac{\theta_{k+1}^p - \theta_k^p}{t_{k+1}^p - t_k^p}$$

$$\theta_{k+1}^p(t_{k+1}) \qquad\qquad\qquad\qquad \implies \alpha_i^p(t_i'') = \frac{\omega_{j+1}^p - \omega_j^p}{t_{j+1}' - t_j'}$$

$$\implies \omega_{j+1}^p(t_{j+1}') = \frac{\theta_{k+2}^p - \theta_{k+1}^p}{t_{k+2}^p - t_{k+1}^p}$$

$$\theta_{k+2}^p(t_{k+2})$$

Where:

$$t_j' = \frac{t_{k+1}^p + t_k^p}{2} \qquad\qquad \text{for} \quad j = 1, \ldots, m; \quad m = l - 1$$

$$t_i'' = \frac{t_{j+1}' + t_j'}{2} \qquad\qquad \text{for} \quad i = 1, \ldots, n; \quad n = m - 1$$

Figure 5.5 presents the obtained angular velocity over time for rotation #3. Once again, it has been verified that all performed rotations share the same qualitative behaviour in terms of velocity. The plot clearly shows the three phases of the control sequence:

1. Acceleration phase of 1 s, where the angular velocity is approximately linear with a positive slope;

2. Steady state phase of 2 s, where the angular velocity is approximately constant;

3. Deceleration phase of 1 s, where the angular velocity rapidly drops due to the opposite applied torque.

Moreover, the angular velocity is affected by noise due to the FDM applied with the above equations.
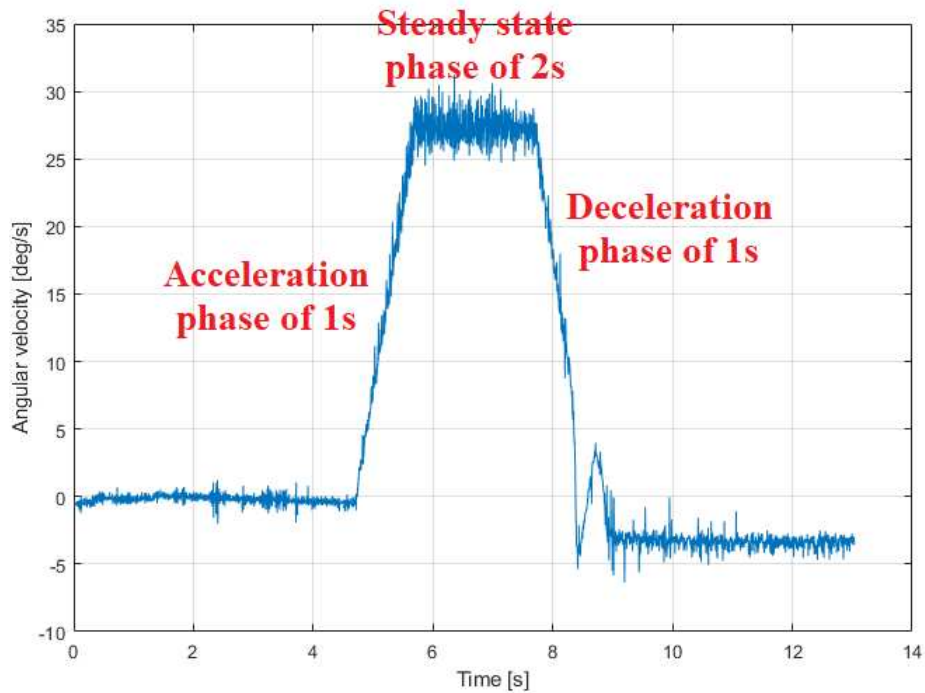
Figure 5.5: Obtained angular velocity over time for rotation #3, with a detail of the three phases of the control sequence.

Similarly, Figure 5.6 presents the obtained angular acceleration over time for rotation #3.
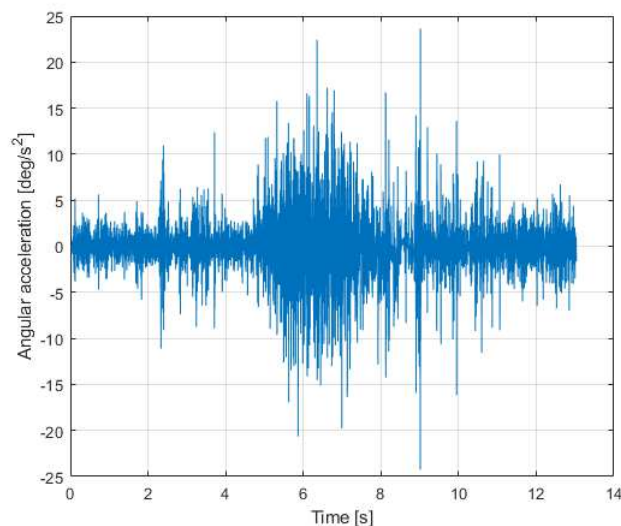
Figure 5.6: Obtained angular acceleration over time for rotation #3.

Once again, it has been verified that all performed rotations share the same qualitative behaviour in terms of acceleration. In this case, the angular acceleration computed with a FDM has been overshadowed by the noise and, therefore, has

not been useful.

For the above reason, a new solution to estimate the inertia around the Z axis has been found. For each set of angular velocities $\vec{\omega}^p$, this new solution has revolved around the following steps:

1. Extract the angular velocities values corresponding to the acceleration phase of Figure 5.5 (linear behaviour with a positive slope over 1 s);

2. Apply a least square linearization with the *polyfit.m* Matlab function;

3. Obtain the slope of the corresponding linearized velocity, which represents an estimation of the angular acceleration applied by nozzles #1 and #2 of Figure 4.23 (Ch. 4).

Therefore, twelve values of estimated angular accelerations have been computed. Figure 5.7 shows the linearized angular velocity with respect to the acquired data for rotation #3.
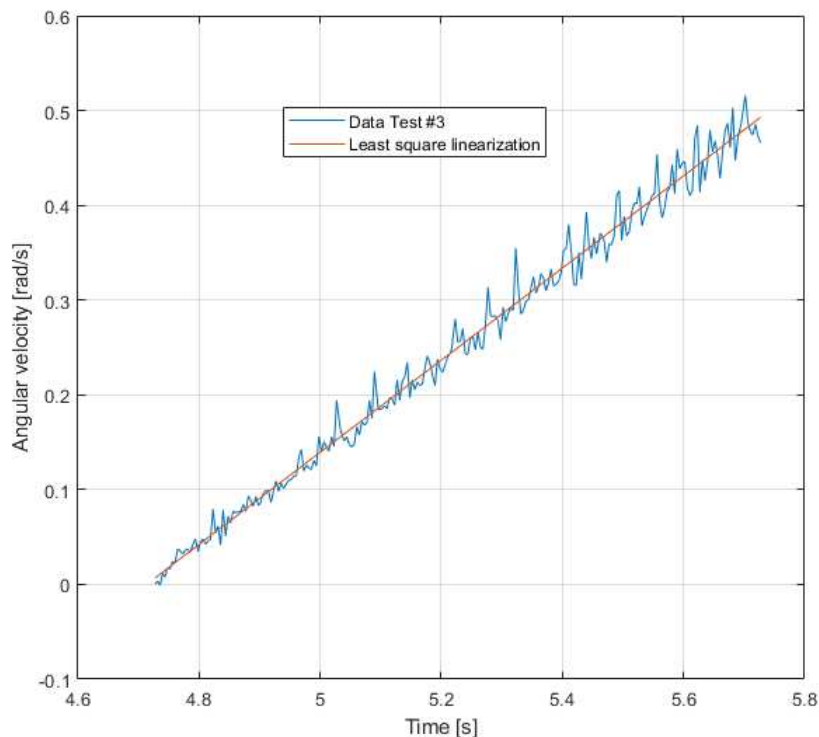
Figure 5.7: Least square linearization of the angular velocity for rotation #3.

From an obtained angular acceleration α^p, the p-th inertia I_{FM}^p around the Z axis has been computed with the torque T^p generated by nozzles #1 and #2 of

Figure 4.23 (Ch. 4). T^p has been estimated with the geometrical arm a_n and the provided thrust F_n of the two nozzles. a_n has been obtained from the CAD model of Figure 3.2a (Ch. 3) with a corresponding value of $264\,\mathrm{mm}$, while F_n has been estimated to be $1.53\,\mathrm{N}$ from the pneumatic tests which have been performed on the pneumatic system [7] before the ones described in this thesis. Therefore:

$$\left.\begin{array}{l} T^p = F_n a_n = 0.404\,\mathrm{N\,m} \\ I^p_{FM}\alpha^p = T^p \end{array}\right\} \Rightarrow I^p_{FM} = \frac{T^p}{\alpha^p} \qquad (5.3)$$

Table 5.5 presents the twelve angular accelerations α^p and inertias I^p_{FM} with two significant figures.

Rotation #	α^p [rad s^{-2}]	I^p_{FM} [kg m^2]
1	0.51	0.79
2	0.52	0.77
3	0.49	0.83
4	0.49	0.82
5	0.49	0.82
6	0.52	0.78
7	0.49	0.83
8	0.50	0.81
9	0.50	0.81
10	0.51	0.80
11	0.50	0.81
12	0.50	0.81

Table 5.5: Results of the angular acceleratons and inertias.

The mean value for the inertia I_{FM} is:

$$\bar{I}_{FM} = \frac{1}{12}\sum_{i=1}^{10} I^p_{FM} = 0.81\,\mathrm{kg\,m^2}$$

The corresponding standard deviation σ_I is:

$$\sigma_I = \sqrt{\frac{1}{10}\sum_{i=1}^{12}(I^p_{FM} - \bar{I}_{FM})^2} = 0.02\,\mathrm{kg\,m^2}$$

Therefore, the overall result is:

$$I_{FM} = 0.81 \pm 0.02 \, \text{kg} \, \text{m}^2$$

The result has a contained error and, therefore, validates the least square linearization method applied to the computed angular velocities. Furthermore, the inertia estimation of the CAD model of Figure 3.2a (Ch. 3) is $0.20 \, \text{kg} \, \text{m}^2$. Even though the two values are of the same order, the discrepancy is $0.61 \, \text{kg} \, \text{m}^2$ (75.3% of the final result). Three reasons have been identified to justify the discrepancy:

1. The CAD model has returned an imprecise computation of the system inertia, which could be related to the approximation of all components to rigid homogeneous bodies;

2. The thrust value of $1.53 \, \text{N}$ has been wrongly estimated with the pneumatic tests;

3. The test procedure of tracking the motion and estimating the inertia from it is not valid.

While plausible, reasons #2 and #3 are solidly confuted by the repeatability of the performed tests, both dynamical and pneumatic ones [7]. Therefore, reason #1 has been identified as the major one to cause the above discrepancy.

Chapter 6

Conclusions

This thesis has presented the mechanical design, development and testing of a floating pneumatic module which has been designed to perform 3-DoF low friction planar motion with three planar air-bearings over a glass plane mounted on an optical bench (levelled table). The module has a total mass of approximately $12\,\mathrm{kg}$ and dimensions of $330 \times 224 \times 224\,\mathrm{mm}^3$. While accomodating different docking systems and operating both as chaser or a target, the main goal has been to simulate docking maneuvers starting from a $500\,\mathrm{mm}$ distance with an actuated propulsion system.

The first part of the thesis has been dedicated to illustrating the main requirements for the mechanical design and the overall final design of the vehicle. The most critical part of the work has been the alignment of the Center of Mass of the system around the centroids of the air-bearings and the thrusters to ensure uniform floating and pure rotations on the levelled table. The solution has been found in the realization of a set of fixed and manually movable steel masses to control the position of the Center of Mass along the XY plane of motion.

The second part of the thesis has been dedicated to presenting a detailed description of the performed test procedures and analyzing the corresponding results. Two tests have been performed:

1. Measurement, control and alignment of the Center of Mass position around the centroid of the air-bearings (and, therefore, the origin of the XY plane) with a dedicated setup of three $10\,\mathrm{kg}$ load cells;

2. Estimation of the inertia around the main rotational axis through the execution of a serie of pure rotations on the levelled table and their tracking with a motion capture system of four IR cameras.

The results of the first test in terms of total mass m_{FM} and Center of Mass position $\vec{r}_{FM}$ on the XY plane are:

$$m_{FM} = 11.827 \pm 0.008 \, \text{kg}$$

$$\vec{r}_{FM} = \begin{pmatrix} 0.0 \pm 0.4 \\ -1.6 \pm 0.6 \end{pmatrix} \text{mm}$$

The results of the second test in terms of inertia around the rotation axis are:

$$I_{FM} = 0.81 \pm 0.02 \, \text{kg} \, \text{m}^2$$

All results have reduced errors and, therefore, validate the several test procedures and methodologies which have been followed.

In conclusion, this thesis has not only achieved its primary objectives in designing and testing a floating pneumatic module but also laid a solid foundation for future laboratory tests. By improving the movable masses system into an automated one, the Center of Mass position will be controlled with greater precision. Additionally, incorporating advanced sensors and real-time feedback mechanisms could enable the module to adapt autonomously during docking simulations. Furthemore, the vehicle will be able to accomodate and test several docking mechanisms, making it an even more valuable asset for various docking maneuvers scenarios.

Bibliography

[1] Markus Wilde, Casey Clark, and Marcello Romano. "Historical survey of kinematic and dynamic spacecraft simulators for laboratory experimentation of on-orbit proximity maneuvers". In: *Progress in Aerospace Sciences* 110 (2019), p. 100552. ISSN: 0376-0421. DOI: https://doi.org/10.1016/j.paerosci.2019.100552. URL: https://www.sciencedirect.com/science/article/pii/S0376042119300466.

[2] Tomasz Rybus and Karol Seweryn. "Planar air-bearing microgravity simulators: Review of applications, existing solutions and design parameters". In: *Acta Astronautica* 120 (2016), pp. 239–259. ISSN: 0094-5765. DOI: https://doi.org/10.1016/j.actaastro.2015.12.018. URL: https://www.sciencedirect.com/science/article/pii/S0094576515004634.

[3] *Air bearing application and design guide.* Revision E. New Way Air Bearings. Aston, USA, 2006.

[4] Jeff Geerling. *Power Consumption Benchmarks.* URL: https://www.pidramble.com/wiki/benchmarks/power-consumption (visited on 07/18/2023).

[5] Marcello Romano and Brij N. Agrawal. "Acquisition, tracking and pointing control of the Bifocal Relay Mirror spacecraft". In: *Acta Astronautica* 53.4 (2003). The New Face of Space Selected Proceedings of the 53rd International Astronautical Federation Congress, pp. 509–519. ISSN: 0094-5765. DOI: https://doi.org/10.1016/S0094-5765(03)80011-5. URL: https://www.sciencedirect.com/science/article/pii/S0094576503800115.

[6] Simone Chesi et al. "Automatic Mass Balancing of a Spacecraft Three-Axis Simulator: Analysis and Experimentation". In: *Journal of Guidance, Control, and Dynamics* 37.1 (2014), pp. 197–206. DOI: 10.2514/1.60380. eprint: https://doi.org/10.2514/1.60380. URL: https://doi.org/10.2514/1.60380.

[7]   Thomas Berthod. "Development and Testing of a Pneumatic Circuit to Control a 12-units Cubesat Simulator". Department of Industrial Engineering. Master's thesis in Aerospace Engineering. Via Venezia 1, Padova (Italy): University of Padova, Sept. 2023.

[8]   Meibao Wang et al. "A Structure for Accurately Determining the Mass and Center of Gravity of Rigid Bodies". In: *Applied Sciences* 9.12 (2019). ISSN: 2076-3417. DOI: `10.3390/app9122532`. URL: `https://www.mdpi.com/2076-3417/9/12/2532`.

[9]   Rice Lake Weighing Systems. *Load Cell and Weigh Module Handbook. A Comprehensive Guide to Load Cell Theory, Construction and Installation.* `https://www.ricelake.com/media/b5mlti1q/m_us_22054_lc-wm_handbook_revb.pdf`. 230 W. Coleman St., Rice Lake, WI 54868, USA: Rice Lake Weighing Systems, 2020.

[10] Tarikul Islam and S. C. Mukhopadhyay. "Linearization of the sensors characteristics: a review". In: *International Journal on Smart Sensing and Intelligent Systems* 12.1 (3919), pp. 1–21. DOI: `doi:10.21307/ijssis-2019-007`. URL: `https://doi.org/10.21307/ijssis-2019-007`.

[11] Kumar Molugaram and G. Shanker Rao. "Chapter 5 - Curve Fitting". In: *Statistical Techniques for Transportation Engineering.* Ed. by Kumar Molugaram and G. Shanker Rao. Butterworth-Heinemann, 2017, pp. 281–292. ISBN: 978-0-12-811555-8. DOI: `https://doi.org/10.1016/B978-0-12-811555-8.00005-2`. URL: `https://www.sciencedirect.com/science/article/pii/B9780128115558000052`.

Appendix A

Differential voltage outputs for CoM measurements

Table A.1 presents the differential voltage outputs for the first measurement of the CoM position and mass (no payload, fixed and movable masses).

Measurement #	Differential voltage outputs [mV]		
	Load cell #1	Load cell #2	Load cell #3
1	1.82	3.43	3.18
2	1.83	3.37	3.22
3	1.77	3.43	3.18
4	1.76	3.44	3.20
5	1.77	3.38	3.21
6	1.79	3.40	3.20
7	1.79	3.39	3.22
8	1.81	3.39	3.23
9	1.83	3.45	3.20
10	1.85	3.39	3.22

Table A.1: Obtained voltage differential values for first measurement

Table A.2 presents the differential voltage outputs for the second measurement of the CoM position and mass (with payload and fixed masses, no movable masses).

97

| Measurement | Differential voltage outputs [mV] | | |
	Load cell #1	Load cell #2	Load cell #3
1	3.65	3.38	3.16
2	3.64	3.34	3.19
3	3.65	3.38	3.16
4	3.64	3.37	3.18
5	3.65	3.39	3.14
6	3.62	3.39	3.17
7	3.63	3.38	3.16
8	3.63	3.38	3.17
9	3.62	3.39	3.20
10	3.62	3.42	3.15

Table A.2: Obtained voltage differential values for second measurement

Table A.3 presents the differential voltage outputs for the measurement of the aligned CoM position.

| Measurement | Differential voltage outputs [mV] | | |
	Load cell #1	Load cell #2	Load cell #3
1	3.88	4.00	3.86
2	3.88	4.01	3.84
3	3.87	4.05	3.84
4	3.93	3.95	3.86
5	3.90	3.97	3.87
6	3.89	3.99	3.87
7	3.89	4.00	3.85
8	3.89	4.07	3.80
9	3.88	4.00	3.86
10	3.92	3.95	3.88

Table A.3: Obtained voltage differential values for CoM alignment

Ringraziamenti

Ecco il capitolo tanto atteso e, forse, il più difficile da scrivere, soprattutto quando si è abituati a gestire equazioni, numeri e tabelle esclusivamente. É, intanto, necessario fare una premessa: il Simone che sono oggi è qui solamente grazie a tutte le persone che citerò di seguito, sia da un punto di vista professionale che personale; senza tutti voi, questo lavoro, questa laurea e questo percorso di studi non sarebbero stati possibili, quindi grazie dal profondo del cuore. Ma, bando alle ciance, veniamo ai ringraziamenti veri e propri.

Innanzitutto, ringrazio il mio relatore, l'Ing. Francesco Branz, il ricercatore Dott. Alex Caon, e i dottorandi Federico Basana e Luca Lion per avermi assistito in laboratorio in questi lunghi mesi nel portare a termine la tesi. La vostra guida è stata preziosa e i vostri consigli saranno portati con me negli anni a venire per la mia carriera professionale.

Ci tengo enormemente a ringraziare la persona più unica al mondo per ogni figlio (o figlia), ovvero la mamma, mia Mamma, Marina, in questo caso. Nonostante le nostre numerose ripicche, vista la testardaggine e l'orgoglio che entrambi ereditiamo dai Franceschi, una fetta di qualsiasi cosa che mi appartenga o caratterizzi la devo a te e, solamente, a te. Ti ringrazio, mamma, per avermi spronato, incoraggiato, rimproverato e amato come pochi (se non altre mamme con altri figli) potrebbero fare. Ti ringrazio, anche, per tutti gli insegnamenti che mi hai lasciato, anzi, che mi lasci ogni giorno. Cara Mamma, non potrei essere più orgoglioso di avere una mamma così, quindi ancora GRAZIE.

Voglio ringraziare profondamente anche il mio papà, Marco. Io e te abbiamo sempre vissuto in quella che a me piace definire una perfetta pacifica convivenza, quasi stoica, e a me è sempre piaciuto così, perchè per certi versi il nostro carattere è simile e compatibile. Non è certo mancato l'amore e il supporto che un padre non può non avere per un figlio, quindi ti ringrazio dal profondo del cuore per tutto quello che hai fatto e continui a fare per me. Quindi, ai miei fantastici genitori, ancora mille volte grazie.

Un ringraziamento ancora immenso è dedicato alla mia ragazza, Giulia. Ormai sei diventata per me una compagna di vita e non ti sostituirei per nulla al mondo. Ti ringrazio, Giulia, per amare e sopportare tutto di me, per rendermi completo. Ti ringrazio per l'enorme supporto che mi hai dato in questi mesi difficili, perchè senza di te non ne sarei mai uscito sano. Grazie per essere la stupenda ragazza quale sei, ti amo dal profondo del mio cuore. Forse, se fai la brava e lasci in pace le mie povere vene, un bel viaggetto a New York lo possiamo anche organizzare (ovviamente è una frase ironica, ma tanto mi conoscete, la serietà non è il mio forte).

Voglio ringraziare, inoltre, la mia stupenda famiglia, da mia nonna Angelina, ai miei zii, zia Daniela, zio Stefano, zio Francesco, zia Michela, zio Anacleto (i vallesi inseriscano mentalmente una "L" dove ben sanno) e zio Massimo, il vostro supporto lo porterò con me per sempre. Come non ringraziare anche i miei incredibili cugini, Matteo, Martina, Isabella, Camilla, Beatrice e Margherita, siete i fratelli e le sorelle che non ho mai avuto e avrete sempre un posto privilegiato nel mio cuore. Della mia famiglia sempre, ci tengo a ringraziare quattro persone che purtroppo ci hanno lasciato, anche da poco: zia Marisa, nonna Leonella, nonno Giacomo e nonno Albano. Questa laurea è dedicata anche a voi che ancora vivete vividamente nei miei ricordi e, soprattutto, a te, Sig. Giacomo, le orme che sto seguendo sono in parte le tue.

Infine, ringrazio profondamente i miei carissimi amici. In primis, al mio più grande amico d'infanzia Filippo, grazie per tutti questi anni di spensieratezza che mi hai regalato, le nostre serate al PC, sugli anime e sui giochi da tavolo sono e saranno parte di me per sempre. Grazie, poi, ai miei insostituibili amici di Valleremita, Nicola, Arment, Francesco e Jacopo, anche voi, come i miei cugini, siete i fratelli che non ho mai avuto; le ore e ore notturne passate sulle panchine le custodirò gelosamente con tutto me stesso.

Un grazie anche a tutti voi che state leggendo questi ringraziamenti: se siete qui oggi e leggete queste mie parole significa che avete avuto un ruolo in questo grande momento e di questo vi ringrazio di cuore.